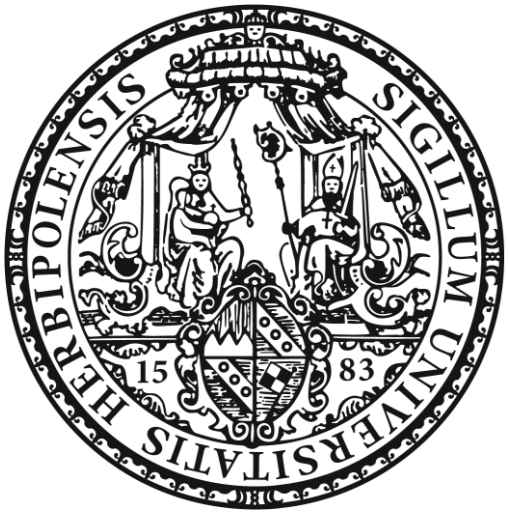

Reconstruction methods for the frequency-modulated balanced steady-state free precession MRI-sequence

Rekonstruktionsmethoden für die frequenz-modulierte balanced steady-state free precession MRT-Sequenz

Doctoral thesis for a doctoral degree

at the Graduate School of Life Sciences,

Julius-Maximilians-Universität Würzburg,

Section Biomedicine

submitted by

Anne Slawig

……

(Name)

from

Leipzig

……

(Place of Birth)

Würzburg…2018…

(Year of Thesis Submission)

Submitted on: ……..……..

Office stamp

Members of the *Promotionskomitee*:

Chairperson: ……..

Primary Supervisor: …… Prof. Dr. Herbert Köstler

Supervisor (Second): …… Prof. Dr. Michael Laßmann

Supervisor (Third): …… Prof. Dr. Thorsten Bley

Date of Public Defence: ……

Date of Receipt of Certificates: ……

Reconstruction methods for the frequency-modulated balanced steady-state free precession MRI-sequence

I. Abbreviations and symbols

GRE	gradient echo	M_0	equilibrium magnetization
SSFP	steady-state free precession	α	flipangle
bSSFP	balanced SSFP	θ	phase of RF-pulse
fm-bSSFP	frequency-modulated bSSFP	θ_0	phase offset
MRI	magnetic resonance imaging	$\Delta\theta$	linear phase term
TR	repetition time	ψ	quadratic phase term
TE	echo time	ϕ	dehasing
MI	maximum intensity		
MIP	maximum intensity projection	δ	chemical shift
CISS	constructive interference in the steady-state	σ	standard deviation
CS	complex sum	ω	angular frequency
SOS	sum-of-squares	γ	gyromagnetic moment
SNR	signal to noise ratio	B_0	static magnetic field
CNR	contrast to noise ratio	f	frequency
CSF	cerebrospinal fluid	Δf	offresonance
FT	Fourier transform	S	signal
FFT	fast FT	$\hat{}S$	mean signal
CINE	multiframe imaging	S_{comb}	combined signal
ECG	electrocardiography	t, τ	time, duration
TMS	tetramethylsilane	t_{single}	time for single acquisition
ppm	parts per million	t_{tot}	total acquisition time
FOV	field of view	t_{HB}	time of one heartbeat
T	tesla	t_{BH}	time of breath-hold
CART	Cartesian	Δt	temporal resolution
RA	radial	N_{pc}	number of phase-cycled images
GA	golden angle	N_{proj}	number of projections
GA SToST	golden angle stack-of-stars	Ng	number of groups
GRAPPA	Generalized Autocalibrating Partially Parallel Acquisition	p	parameter in p-norm combination
ROI	region of interest	ds	step width

Hz	Hertz	C_i	coil sensitivities
px	pixel	ϕ	phase of spoke
Muffm	multifrequency reconstruction for frequency-modulated bSSFP	n	natural number
T_1	longitudinal relaxation time	I	intensity
T_2	transversal relaxation time		
Gx	gradient on x-axis		
Gy	gradient on y-axis		
Gz	gradient on z-axis		
HB	Heartbeat		
BH	Breath-hold		
RF	radio-frequency		

II. Content

1 Introduction

Today's technology allows us a look inside the human body without invasive procedures. Ultrasound, X-rays, CT and MRI are basic equipment in all major departments of radiology in industrialized countries. Especially MRI experienced an increase in popularity in the recent years. In Germany the number of MRI scanners per 1Mio. inhabitants skyrocketed from only 4.4 in 1999 to 33.6 in 2015 (1). In 2015 the number almost reached the number of the previously dominant CT scanners (35.1 per Mio. inhabitants) (2). Major advantage of MRI, in comparison to CT or X-rays, is the generation of an image without the use of ionizing radiation. Furthermore, it provides superior soft tissue depiction and is tunable to provide different contrasts or detect biological processes (e.g., proton density, diffusion, perfusion, oxygen saturation). Despite these major advantages and its wide use for diagnostic purposes, MRI is still not the primary imaging modality in radiology. Drawbacks, like high costs, long scan times, acoustic noise, small confined spaces, limited image resolution and artifacts, remain challenges in the clinical routine and stay in the focus of research.

For acquiring an image, the MRI scanner executes a set program of magnetic field gradients and radiofrequency (RF) pulses, called pulse sequence or MRI sequence. Main types include spin-echo and gradient echo sequences, which differ in the signal generation. Spin echo sequences provide the lion's share of clinical MRI sequences and well-known image contrasts. Gradient echo sequences allow rapid imaging and have gained rising interest in recent years as the technical development provided improved gradient systems. Today's technology can produce high gradients in the magnetic field and fast and precise switching patterns, allowing to exploit the full potential of gradient echo sequences.

The most important representative of gradient echo sequences is the balanced steady-state free precession (bSSFP, also known as trueFISP) sequence as it allows rapid imaging with exceptional high signal gain. In fact, balanced steady-state free precession provides the highest SNR per unit time of all known sequences (3). Next to imaging speed, bSSFP produces a specialized image contrast, that is, for example, sensitive to differences between fluids and soft tissue. The combination of speed, high signal levels and the uncommonly strong contrast between blood and myocardium make it a highly interesting candidate for cardiac imaging. Unfortunately, the sequence is very sensitive to field inhomogeneities, which result in dark banding artifacts and can spoil the diagnostic value of the whole image.

The signal drops at certain offresonances, that manifest as banding artifacts in the image, were already shown by Carr (4), who first described a steady-state free precession sequence in 1954 and termed an “intensity anomaly” by Freeman and Hill in 1971 (5). In 1986, Oppelt et al. first established their detrimental effect for imaging purposes as “higher field inhomogeneity lead to intolerable artifacts” (6). The technical afford to get reliable imaging was seen as huge, and it was considered to be “impossible to obtain a true FISP image with one scan whose signal contrast is independent of static local field inhomogeneities” (7). Thus, up to the beginning of the century applications for bSSFP at 1.5T were limited and they were rarely used in clinical settings (8,9). Only with new and improved shimming technique and high-performance gradients, which allowed significantly shorter repetition times, the challenges were overcome for first applications, “artifact-free [b]SSFP images can now be obtained in a single acquisition” (10) at 1.5T. At this time the value for cardiac imaging was not questioned. With the recent advances and improvements in image quality and acquisition speed “a new era in non-invasive cardiovascular imaging” was opened (11).

The introduction of high field scanners in the clinical environment, lead to a repetition of challenges just overcome. Although 3T seemed promising to increase the signal level and therefore allow faster acquisition or higher resolution, again field inhomogeneity and banding artifacts impaired image quality. High-quality bSSFP imaging at 3T was only possible using extensive and time-consuming techniques (12). As before, the technical advancement allowed the spreading of high-end hardware, fast gradient systems and sophisticated shimming routines. So already in 2005, bSSFP was seen as “a powerful sequence for cardiac imaging”, also at 3T (13).

Today research facilities and specialized MR centers implemented the first ultra-high field scanners at 7T or even 9.4T. The increase in field strength is accompanied by the same (and more) challenges as the change from 1.5T to 3T was before. Banding has become an issue again (14,15). Unfortunately, the former technical solution of advanced shimming and lowering of the repetition time might not be expandable forever and alternative approaches are of high interest.

This work is concerned with an alternative approach to banding free bSSFP imaging, the frequency-modulated bSSFP. First, a short excursion into the theoretical background of gradient echo imaging and especially bSSFP is given in chapter 2 and general methods used in this work are described in chapter 3. Afterwards, in chapter 4, specialized applications that benefit from the use of frequency modulation are examined. To compensate the inherent signal loss in an fm-bSSFP acquisition, a novel advanced reconstruction algorithm is presented in chapter 5. Finally, fm-bSSFP acquisition is employed for water-fat separation in conjunction with a phase-sensitive separation approach in chapter 6.

2 Theory

This chapter first focusses on the imaging sequence. In MRI a sequence describes a set series of RF pulses and gradients in the magnetic field. A short overview of gradient echo sequences (GRE) is given in 2.1 followed by a more detailed description of the balanced steady-state free precession sequence (bSSFP) in 2.2 and the modification to a phase-cycled sequence in 2.3 or a frequency-modulated balanced steady-state free precession sequence (fm-bSSFP) in 2.4. Also, the simulation of MRI signals resulting from such measurements is considered in 2.6, as they provide a powerful tool for testing, analysis and prediction of the signal behavior. The data of MRI measurements is acquired in the Fourier-domain, so-called k-space. As the manner of collection has a significant impact on the resulting images, a very short overview of the most common k-space trajectories is given in 2.7. Finally, as chapter 6 focuses on an application for separation of water and fat in an MRI image, some details on such separation methods is given in 2.8.

2.1 Gradient echo sequences

With the ongoing development of gradient systems and power amplification technology, more powerful hardware becomes available for MRI scanners. New possibilities include increasing overall field strength, and rapid imaging. High gradient amplitudes and slew rates allow fast gradient switching patterns and thus lead to the recent popularity of Gradient Echo sequences (GRE)(16).

While a spin echo sequence relies on refocusing RF pulses to realign dephased magnetization, a GRE sequence uses the magnetic gradient fields. A gradient echo is created by applying a gradient reversal, i.e., for all applied gradients a gradient with an opposed polarity is played out as well. The peak signal intensity occurs when all spins are coherent, which is whenever the net gradient area is zero (17). A typical GRE sequence consists of repeated blocks of RF excitation, imaging gradients and acquisition. The repetition time (TR) between successive RF pulses limits the ability of the spins to relax into the thermal equilibrium (5). Also referred to as a dynamic equilibrium, a steady-state is established between the effects of the relaxation processes and the effects of the RF pulse (18). Different steady-states will evolve depending on the relation between TR, longitudinal relaxation time T_1 and transversal relaxation time T_2 (5). If TR is sufficiently long ($TR > 2T_1 > 2T_2$) the magnetization relaxes completely and equilibrium magnetization M_0 is established before the next pulse. For TR values below $2T_1$, longitudinal relaxation is incomplete, while for TR values below $2T_2$ both longitudinal and transversal relaxation are incomplete (17).

The second main feature of GRE sequences is the gradient switching scheme applied in between two RF pulses. A multitude of acronyms has been established to describe and distinguish different GRE sequences. Basic types are (17):

- balanced SSFP: (Other names include: TrueFISP, FIESTA, balanced FFE)
  All gradients are balanced, meaning that the overall gradient moment on each axis is zero. Transverse magnetization is recovered within one TR.
- Gradient spoiled SSFP: (Other names include: SSFP-FID, FISP, GRASS, FFE)
  A spoiler gradient is placed after the imaging gradients, at the end of TR. Thus, the overall gradient moment is no longer balanced. The spoiler averages the transverse magnetization across one voxel at the end of TR.
- Reversed Gradient spoiled SSFP: (Other names include: SSFP-ECHO, PSIF, T2- FFE)
  A spoiler gradient is placed before the imaging gradient, at the beginning of TR. Thus, the spoiler averages the transverse magnetization before imaging.
- Double Echo imaging: (Other names include: FADE, DESS)
  A spoiler gradient is included in the middle of a TR interval and thereby combines a gradient spoiled and a reversed gradient spoiled signal.
- RF spoiled SSFP: (Other names include: FLASH, SPRG, T1-FFE)
  In addition to a spoiler gradient, the phase of the RF pulses is incremented in a quadratic fashion, eliminating the transverse magnetization.

As this work focuses on a balanced gradient scheme, a more detailed description is given in the following sections. More details on the pulse sequences, applications, contrast and modifications of other types can be found in dedicated literature (16,17,19–21).

2.2 Balanced steady-state free precession

A gradient echo sequence with a fully balanced gradient scheme on all three axes is called a balanced steady-state free precession sequence (bSSFP). Historically, this sequence was simply referred to as “steady-state free precession (SSFP)” and first mathematically described by Carr (4) for the special case of $T_1 = T_2$. Later, Ernst and Anderson (22) and Freeman and Hill (5) and many others (3,17,18,23–25) described the signal properties in a more general fashion. Increasing popularity of rapid imaging sequences also lead to many different applications of bSSFP. First and foremost, it is used in cardiac imaging (12,26,27) as it allows high temporal resolution and excellent contrast between blood and myocardium. Other popular clinical applications include interventions (28), angiography (29,30), inner ear and cranial nerve (31,32), abdominal

imaging (33,34) and fetal imaging (35). Recent advances have also been made to use bSSFP in magnetic transfer imaging (36–38), diffusion imaging (39,40) or functional MRI (41–44).

2.2.1 Sequence architecture

All GRE sequences consist of a train of equally spaced RF pulses. Gradients along all three axes allow for Fourier encoding and acquisition in-between two consecutive pulses. Therefore, the minimum repetition time TR is limited by the gradient switching speed. Each RF pulse is characterized by its flipangle α and direction (or phase) θ. In a standard bSSFP sequence both parameters are either kept constant or a sign alternation is introduced for α. The latter shifts the center of the passband to the onresonant position (3) (see offresonance profile in Figure 2 in section 2.2.4) and is commonly applied in bSSFP acquisitions. Additionally, imaging sequences contain an initial preparation phase to allow the magnetization to reach the steady state. In general, the transition from thermal equilibrium to the steady state is completed after $5T_1$ using the standard sequence as described before. As it is marked by complex and oscillatory signal behavior, leading to image artifacts, different preparation schemes have been suggested to shorten the transient phase. Examples are: the inclusion of a preparatory $\alpha/2$ pulse at TR/2 before the first pulse or a preparatory train of RF pulses with linearly increasing flipangle α. The former reduces the transient phase in a clinical imaging setup to approximately 40-50 RF pulses, the latter even to 10-15 RF pulses (16).

The sequence diagram of one TR interval is schematically shown in Figure 1.

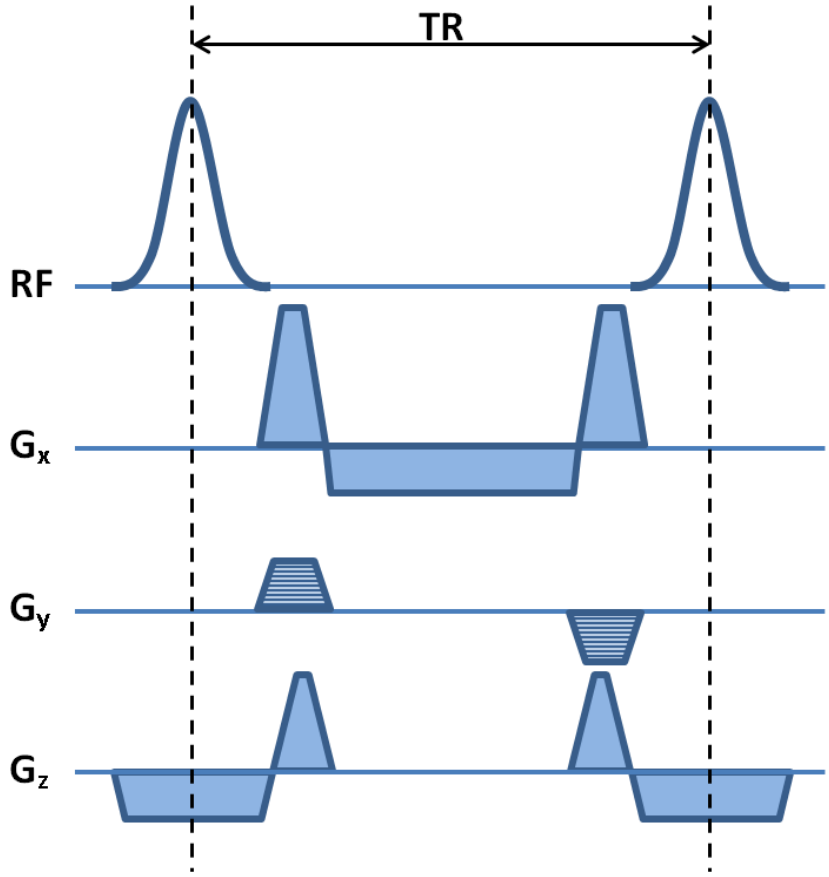

Figure 1 Sequence diagram of a standard bSSFP sequence. Equally spaced RF pulses are interspersed with periods of free precession. The sign of the RF pulse can alternate with each pulse. Within one TR the gradients on all axes (Gx, Gy, Gz) are balanced, meaning the overall gradient moment is zero. The phase-encoding gradient Gy changes when different positions in k-space are acquired but is always balanced.

2.2.2 Magnetization dynamics

To facilitate the study of motion of a magnetization vector, a reference frame rotating at the Larmor frequency ($\omega = \gamma * B_0$) is employed. Within such a rotating reference, the magnetization vector in a bSSFP experiment executes a periodic motion with the same period as the imposed pulse sequence (5).

The motion within one TR interval can be described as follows (45):

An excitation pulse with the flipangle α corresponds to a rotation of the magnetization around an axis in the transverse plane determined by the pulse direction θ. In an imaging sequence, a slice selection gradient is played out during the excitation pulse which causes linear dephasing in slice selection direction. The slice selection gradient is directly followed by a rewinder pulse of opposite polarity. Thus, the magnetization is rephrased and forms a single vector tilted by an angle of α. The

gradients along x- and y-axis enable frequency and phase encoding for imaging. In the simple case of collecting the central line in k-space the phase gradient can be neglected. While the initial read gradient causes dephasing of the magnetization, a rewinder gradient is played out along the same axis with opposite polarity directly afterwards. Again, the magnetization is rephased to a single magnetization vector, forming the gradient echo at timepoint TE (echo time). As the read gradient is still active the magnetization dephases again after TE. As the gradient scheme in bSSFP is supposed to be balanced on all axes, another lobe of the read gradient is added for rephasing. The magnetization vector just before the next RF pulse is a single vector nearly identical to the vector at the beginning of the respective TR interval. Differences occur due to relaxation processes. T_1 relaxation manifests in an increase in the longitudinal component, while T_2 relaxation shortens the transverse component of the magnetization vector.

As all gradient effects are canceled out within the TR interval, only the influence of RF pulses and relaxation as well as free precession need to be considered in a bSSFP sequence. Regarding only the onresonant case, the bSSFP excitation pulse train with the alternating flipangle scheme leads to a simple oscillation of the magnetization vector around the z-axis. In this steady-state, the amplitude of the echo signal, neglecting damping due to relaxation, can be estimated as (45):

$$S = M_0 * sin\left(\frac{\alpha}{2}\right), \qquad [1]$$

where M_0 is the magnetization in termal equilibrium and α is the flipangle.

2.2.3 Offresonance

So far, only the onresonant case was considered. As in most practical applications the field homogeneity is limited, even with modern shimming systems, the resonance frequency varies across the field of view. Offresonance, here defined as the difference in frequency between radiofrequency synthesizer and actual local precession frequency, will lead to a phase advance of

$$\phi = 2\pi * \Delta f * TR \qquad [2]$$

within one TR interval (45). This additional dephasing around the z-axis alters the steady-state established by the train of RF pulses. For small offresonance values only small changes in signal amplitude occur, but if the offresonance causes a dephasing of $\phi \approx \pi$, the steady state signal nearly collapses completely. The change in signal intensity with offresonance or dephasing is shown in Figure 2, Figure 3, Figure 4 and Figure 5 for different measurement and tissue parameters.

Such offresonance profiles show a 2π periodic signal. The sharp and significant drop-outs at $\pi \pm 2n\pi$ manifest as dark lines across the field of view in imaging applications, so called banding artifacts. To allow for the acquisition of banding free images all, excited spins must precess within a frequency range of (45):

$$\Delta f = \pm \frac{1}{2TR}. \quad [3]$$

State-of-the-art MRI scanners offer several possibilities to reach these specifics. Measurements should be conducted using short TR values and a homogeneous magnetic field can be achieved by advanced shim systems. Additionally, the position of banding artifacts can be shifted by changing the measurement frequency, which allows using a frequency scout, doing multiple phase-cycled acquisitions (see section 2.3) or frequency modulation (see section 2.4).

2.2.4 Analytical description

The signal intensity of a bSSFP experiment varies greatly with offresonance. An analytical description of the offresonance profile can be given for the signal immediately after the RF pulse. Assuming that gradients are the main source of dephasing within one interval, the balanced scheme compensates these effects. Thus, overall signal intensity S at the point in time TE = TR/2 is dependent on the dephasing angle within one TR interval ϕ, and can be derived by (24):

$$S(t = TE, \phi) = \frac{a * e^{-i\,\phi} + b}{c * \cos(\phi) + d} * e^{-\frac{TE}{T_2}} \quad [4]$$

where

$$a = -(1 - E_1) * \sin(\alpha) * E_2,$$

$$b = (1 - E_1) * \sin(\alpha),$$

$$c = E_2 * (E_1 - 1) * (1 + \cos(\alpha)),$$

$$d = (1 - E_1 * \cos(\alpha)) - (E_1 - \cos(\alpha)) * E_2^2,$$

and

$$E_1 = e^{-\frac{TR}{T_1}}, \qquad E_2 = e^{-\frac{TR}{T_2}}$$

Using an alternating flipangle pulse train changes Eq. [4] to:

$$S(t = TE, \phi) = (-1)^n \frac{-a * e^{-i\,\phi} + b}{-c * \cos(\phi) + d} * e^{-\frac{TE}{T_2}} \quad [5]$$

Next to offresonance, the tissue parameters T_1 and T_2, as well as the sequence parameters TR, TE and flipangle α influence the shape of the offresonance profile as well as overall signal intensity. Regarding only the onresonant case for fast imaging with $TR << T_2 \leq T_1$ simplifies the Eq.[5] to (3):

$$S(\phi = 0) = M_0 \frac{(1 - E_1)\sin(\alpha)}{1 - (E_1 - E_2)\cos(\alpha) - E_1 E_2} \quad [6]$$

Equation [6] shows a dependency of the signal on T_1 and T_2. bSSFP sequences therefore do not provide standard T_1 or T_2 weighted images, but have a special T_1/T_2 contrast. From the onresonant signal equation the optimal flipangle and maximum signal amplitude can be derived (3):

$$\alpha_{opt} = \cos^{-1}\left(\frac{E_1 - E_2}{1 - E_1 E_2}\right) \approx \cos^{-1}\left(\frac{T_1/T_2 - 1}{T_1/T_2 + 1}\right) \quad [7]$$

$$S_{max} = \frac{1}{2} M_0 * \sqrt{\frac{T_2}{T_1}} \quad [8]$$

As some biological tissues have similar relaxation times for T_1 and T_2 (e.g. water or fat) bSSFP can collect up to ½ M_0 in perfect conditions. As of today, no other known sequence is able to collect a higher signal per unit time than bSSFP (3,45).

2.2.5 *Signal behavior*

As shown in section 2.2.4 the signal level of bSSFP depends on the tissue parameters T_1 and T_2 as well as on the measurement parameters α and TR, and the offresonance. The offresonance profile for an alternating pulse scheme calculated from Equation [5] with $\alpha = 50°$, $T_1 = 1000ms$ and $T_2 = 200ms$, TR$= 4ms$, TE$= 2ms$ is shown in Figure 2. Highest signal level is achieved at zero offresonance or whenever dephasing reaches multiples of 2π. This level is sustained for small deviations in resonance frequency, but drops down to zero when the dephasing approaches $\phi \approx \pi \pm 2n\pi$. Thus a periodic profile results. The phase of the signal is constant with a sudden change of π at the position of the signal Nulls.

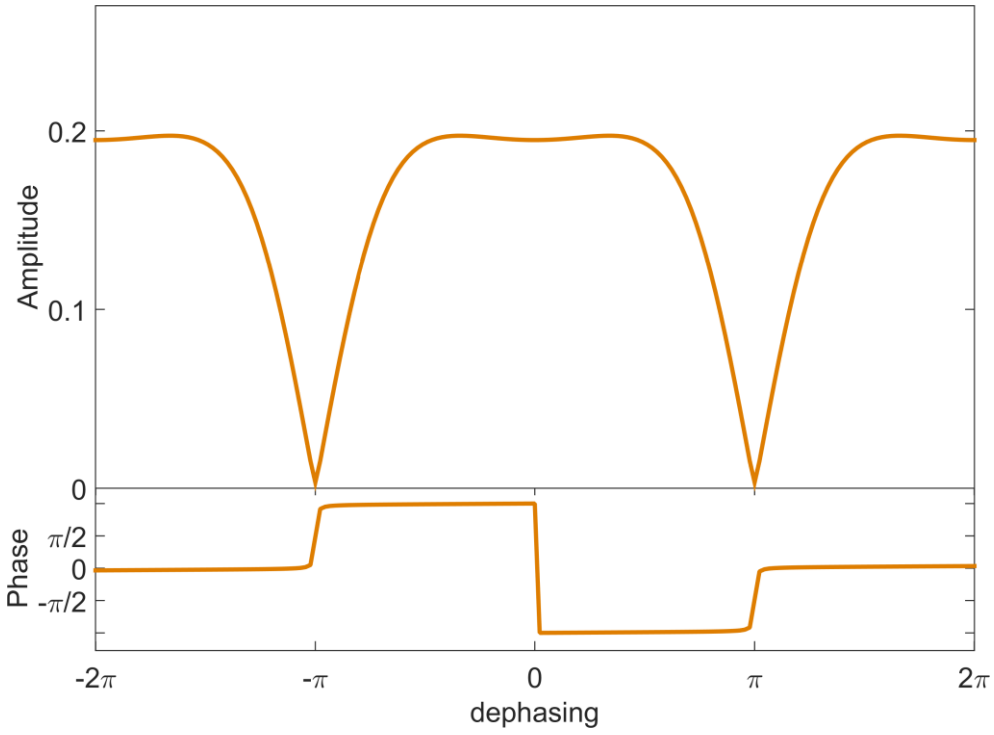

Figure 2: Signal behavior of bSSFP. Magnitude and phase of an exemplary bSSFP signal. Parameters are $\alpha = 50°$, $T_1 = 1000ms$, $T_2 = 200ms$, TR $= 4ms$, TE = TR/2.

The influence of variations in flipangle is shown in Figure 3. The optimal flipangle for collecting maximum signal intensity is dependent on the T_1/T_2 ratio (see Eq. [7] in section 2.2.4). For the examples given in Figure 3, the optimal flipangle is $\alpha_{opt} = 48.2°$ and is closely represented by the yellow line ($\alpha = 50°$). For values higher than the optimum ($\alpha > \alpha_{opt}$), an increasing flipangle will lower overall signal intensity and cause the plateau around the perfectly onresonant case to become narrower (red and blue in Figure 3). For angles smaller than the optimum ($\alpha < \alpha_{opt}$), the plateau develops a dip around zero, such that the onresonant case does not provide the highest signal amplitude anymore (purple in Figure 3) (3). The phase behavior is not influenced by changes in the flipangle.

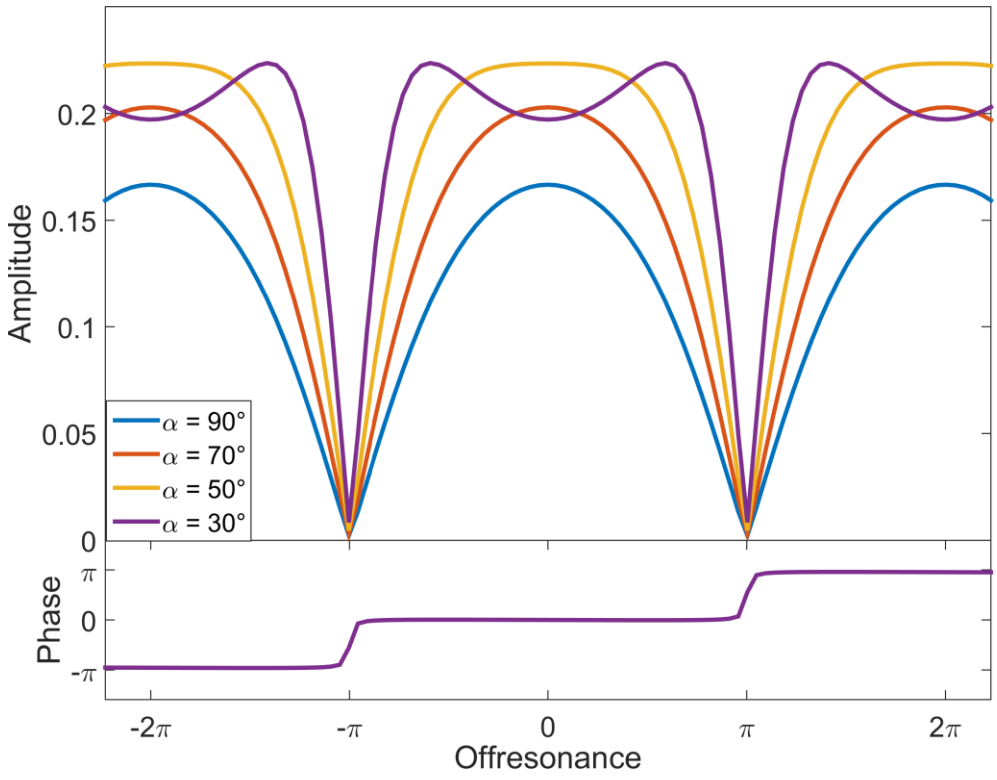

Figure 3: bSSFP signal behavior for varying flipangle at TE = TR/2 for $T_1 = 1000\text{ms}$, $T_2 = 200ms$, TR $= 4ms$ after 500 preparation pulses. The shape of the offresonance profile varies with flipangle. For decreasing flipangle the plateau widens and onresonant signal level increases. At a certain angle, depending on T_1/T_2, a dip starts forming which leads to the maximum signal intensity being shifted away from zero offresonance. The phase behavior is independent of the flipangle.

The influence of T_1 and T_2 always needs to be regarded in unison as variation is only significant if the ratio between the two values changes as shown in Figure 4. Changing T_1 and T_2 simultaneously, such that the ratio remains constant does not influence the signal (compare red and yellow in Figure 4). A higher or lower T_1/T_2 ratio will decrease or increase overall signal intensity, respectively. Additionally, the optimal flipangle changes, thus the T_1/T_2 ratio influences the signal shape for a given flipangle. Again, the phase behavior is independent.

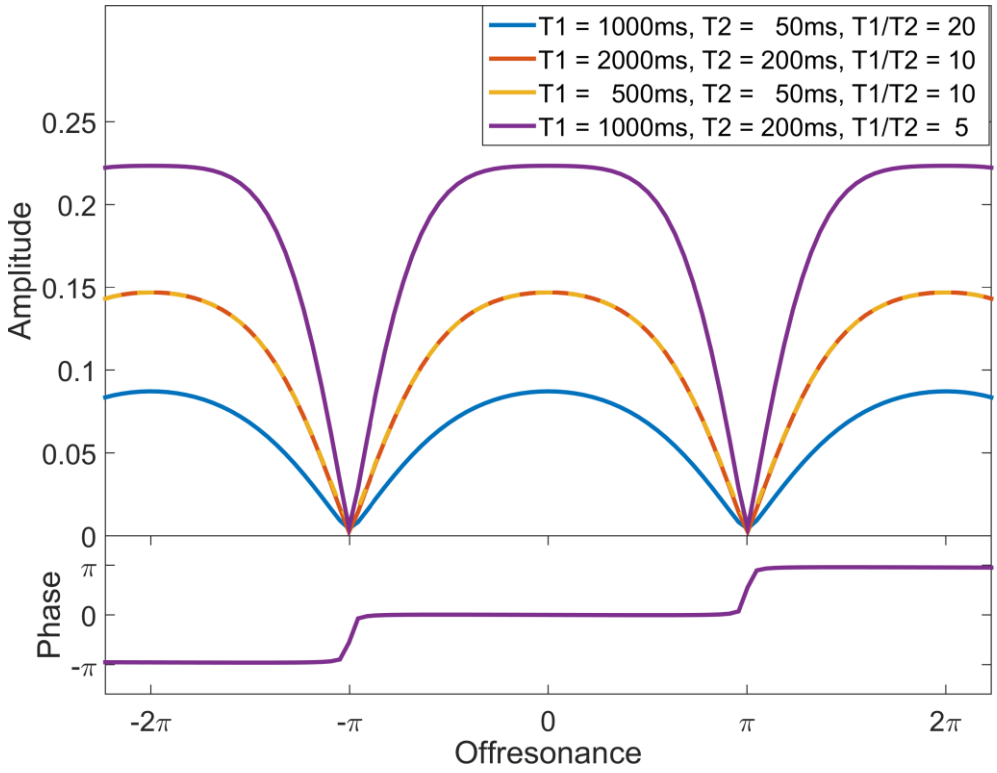

Figure 4: bSSFP signal behavior at TE = TR/2 for $\alpha = 50°$ and TR $= 4ms$ after 500 preparation pulses. The shape of the offresonance profile depends on T_1 and T_2. As choosing different value pairs for T_1 and T_2 with the same ratio does not affect the signal, the behavior depends on the ratio T_1/T_2 only. With increasing T_1/T_2 the signal level decreases. The phase behavior is independent.

The measurement parameter TR does not influence the bSSFP offresonance profile in shape or height. But as the dephasing is dependent on TR and the difference in frequency (Eq. [2]) the TR values define the range in Hz were banding free imaging is possible: $\Delta f = \pm\frac{1}{2TR}$ (45).

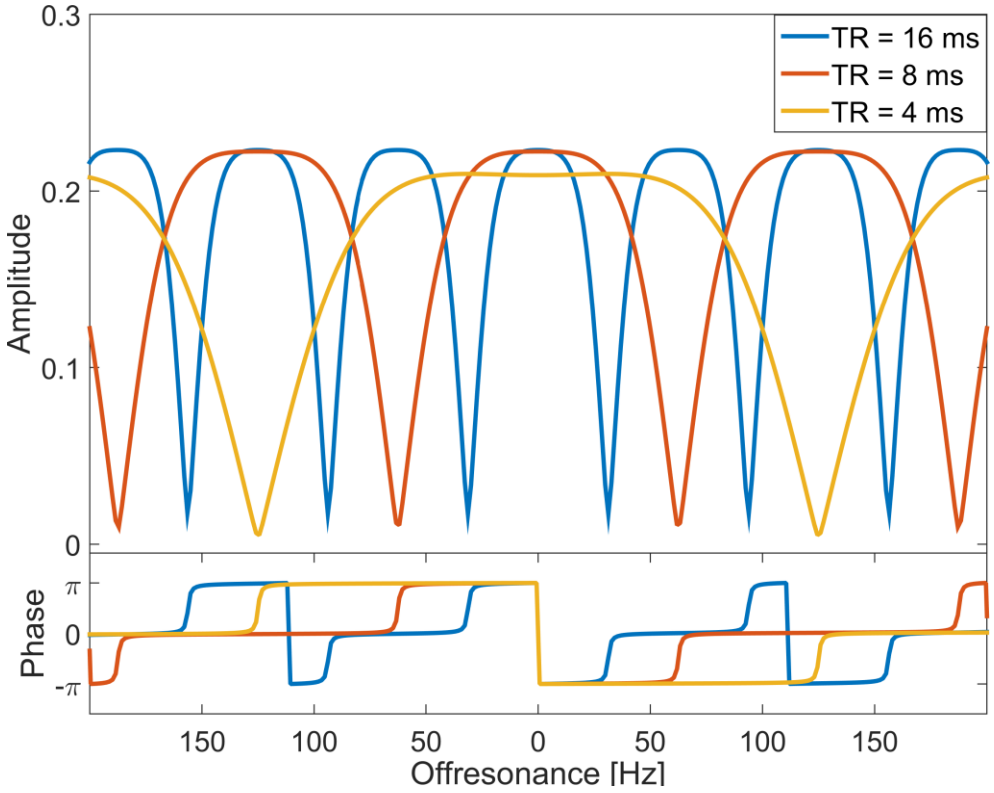

Figure 5: bSSFP signal behavior at TE = TR/2 for $\alpha = 50°$, $T_1 = 1000ms$ and $T_2 = 200ms$ after 500 preparation pulses. Note that offresonance is given in Hz rather than degree to show differences. Decreasing TR increases the period of the offresonance profile, thus showing less frequent signal drop outs. Short TR values are recommended for robust imaging without banding artifacts. Signal phase shows the same lengthening in period as the magnitude signal.

2.3 Phase-cycled bSSFP

Each RF pulse in the pulse train during a GRE experiment has a characteristic flipangle α and phase θ. In a standard bSSFP measurement the phase is kept constant over the whole acquisition while the flipangle can alternate between α and $-\alpha$ for consecutive RF pulses. If the phase of the pulse is increased by a constant value $\Delta\theta$ for each pulse the offresonance profile gets shifted by $\Delta\theta/2$ and bandings appear at different positions (see offresonance profile in Figure 6, simulation in Figure 27 or in vivo acquisition in Figure 36). In this context the aforementioned alternating flipangle scheme can be described as constant flipangle α and phase increase of $\Delta\theta = \pi$. The phase of the n-th RF pulse can be calculated as (46):

$$\theta(n) = \theta_0 + \Delta\theta \cdot n \qquad [9]$$

Phase-cycling describes the procedure of acquiring multiple bSSFP measurements with different $\Delta\theta$. In the complex plane the signal for different linear increments $\Delta\theta$ forms an ellipse. Interestingly, for even spaced $\Delta\theta$ distances the magnetization is not uniformly distributed but bunches together (5) at $\phi = \pi$ or at $\phi = 0$ for the alternating flipangle scheme shown in Figure 6.

Commonly in phase-cycled acquisitions, the values for $\Delta\theta$ are chosen to be equally spaced, e.g. $\Delta\theta = 0$, $\Delta\theta = \pi/2$, $\Delta\theta = \pi$, $\Delta\theta = 3\pi/2$ for $N_{pc} = 4$ phase-cycled images. As using a different phase-cycle shifts the offresonance profile spatially, i.e. the position of banding artifacts in the FOV shifts as well. The position can thus be tuned to not overlay the structures of interest as long as bandings are spaced far apart. These so-called frequency scouts, a successive spatial shift of bandings, are common in clinical routine, although they can be time-consuming (47,48). Additionally, two or more phase-cycled acquisitions can be combined to form one image with suppressed banding (49–53).

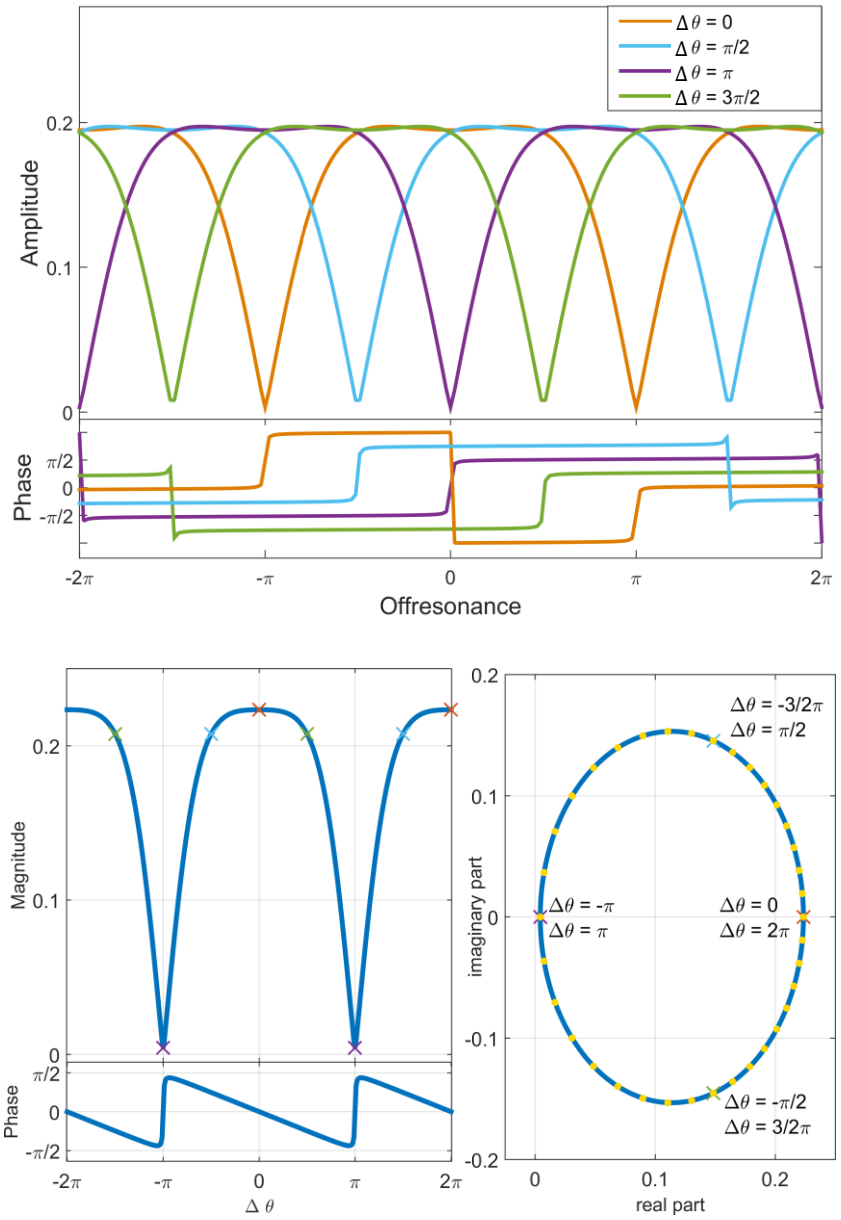

Figure 6: Signal behavior of bSSFP. Magnitude, Phase and complex signal of an exemplary bSSFP signal. Parameters are $\alpha = 50°, T_1 = 1000ms,\ T_2 = 200ms$, TR = 4ms, TE = TR/2. Markers in the same color show equivalent points in the magnitude and complex signal. Note that signal points are not evenly spaced in the complex plane (yellow dots).

Combination algorithms for phase-cycled bSSFP differ in their banding artifact reduction, SNR efficiency and possible influences on image contrast. For all procedures, the result depends on the number of phase-cycled images acquired and the shape of the offresonance spectrum. Most commonly used, and easily implemented, procedures include maximum intensity, complex sum, magnitude sum or sum-of-squares combination. A detailed analysis of the performance of these combination methods is given by Bangerter et al. (49) and summarized below.

For the maximum intensity (MI) combination all phase-cycled acquisitions are reconstructed individually, and the maximum magnitude value of all images is chosen in a pixel-wise manner to

form the final image. The implementation using $N_{pc} = 2$ phase-cycled images, termed “constructive interference in the steady-state (CISS)” (53), is routinely used in clinical practice. MI provides good results but only in a limited parameter space.

Maximum intensity signal: $$I_{MI} = \max(|m_1|, |m_2|, \dots, |m_n|), \quad [10]$$

where m_n is the signal intensity in the n-th image.

A complex sum combination adds the complex k-space or image data of all acquisitions. It performs well regarding banding reduction but has non-optimal SNR due to phase differences in the images. For a very high number of phase-cycled acquisitions, the complex sum converges to a gradient spoiled SSFP image.

Complex sum signal: $$I_{CS} = \left| m_1 + m_2 + \cdots + m_n \right|, \quad [11]$$

where m_n is the signal intensity in the n-th image.

Near-optimal SNR efficiency is reached by a sum-of-squares combination where each image is squared, all images are summed, and a square-root operation provides the final image. The procedure is comparable to the standard combination of single coil images from phased-array coils. The procedure performs well for large numbers of phase-cycled images but otherwise provides suboptimal banding removal.

Sum-of-squares signal: $$I_{SOS} = \sqrt{|m_1^2| + |m_2^2| + \cdots + |m_n^2|}, \quad [12]$$

where m_n is the signal intensity in the n-th image.

Furthermore, weighted combinations of the phase-cycled images have been proposed (54). The weights for each phase-cycled image can be derived directly from the image magnitude m_n:

Weighted combination: $$P_{wc} = \left| \sum_n |m_n|^P m_n \right|^{\frac{1}{p+1}}. \quad [13]$$

Here, with increasing value of p, the banding artifact reduction improves but SNR efficiency decreases. The so-called p-norm combination (55) derives the weights from the image sensitivity profiles C_i:

p-norm combination: $$m_n = M * C_n, \quad P_{norm} = |M| * \left(\sum_n |C_n|^P \right)^{\frac{1}{p}}. \quad [14]$$

For each given set of sensitivities, there exists a value of p which provides the flattest overall profile. This optimal p can be found empirically by computing images for a wide range of practical p values.

Next to the combination algorithm, the quality of the result mainly depends on the severity of the field distortions and the number of images collected. In general, the more inhomogeneous the field, the more individual images are required (49,51). As each image necessitates a delay and new preparation phase the total measurement time t_{tot} increases with the number of images N_{pc}:

$$t_{tot} = t_{single} * N_{pc}. \quad [15]$$

Thus, phase-cycled bSSFP acquisitions always present a tradeoff between measurement time and optimal banding removal.

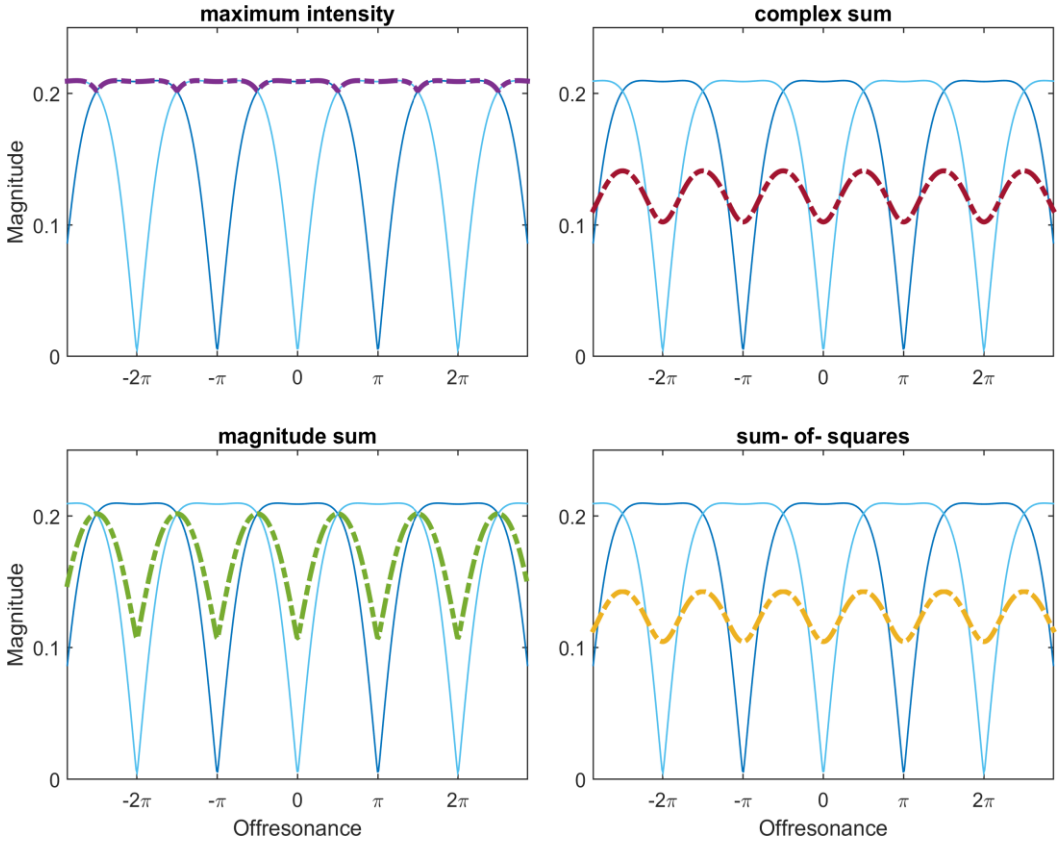

Figure 7: offresonance profile for two phase-cycled bSSFP experiments ($\Delta\theta = 0$ in blue and $\Delta\theta = \pi$ in dark blue) and combination methods. Changing the linear phase increment shifts the profile such that signal drop-out and consequently bandings appear at different positions. Combining two or more phase-cycled signals can alleviate bandings. Shown are maximum intensity (purple), complex sum (red), magnitude sum (green) and sum-of-squares combination (yellow).

2.4 Frequency modulation

The concept of frequency modulation (fm) in bSSFP was first described by Foxall in 2002 (56) and suggests a continuous linear change in the frequency of the excitation pulse. As in MR imaging, the frequency is commonly used to encode the slice position, a change is not practical, as it would induce a slice shift. Therefore, the frequency-modulated sequence used in this work was implemented based on a phase change with each RF pulse. The same effect as by a literal frequency modulation can be achieved by adding a quadratic term to the phase of the n-th RF pulse. The phase of the n-th RF pulse can then be calculated as (57):

$$\theta(n) = \theta_0 + \Delta\theta \cdot n + \psi \cdot n^2, \qquad [16]$$

where θ_0 is a constant phase offset and $\Delta\theta$ describes the aforementioned linear phase-cycle. While high values for the quadratic term ψ are used for RF spoiling in nonbalanced SSFP sequences (e.g. common spoiling values are 117° or 50° (58)), small values generate a smooth shift. Theoretical and experimental considerations estimate the maximum change tolerable for the steady-state to be 3° per sequence cycle, preferably less (56,57). When implemented in a standard Cartesian imaging sequence, the slow and continuous variation eliminates the need for a delay or multiple preparation phases for the acquisition of phase-cycled images. Even more promising is the combination with a radial sampling pattern as recently proposed by Benkert (57,59). Here, each projection is acquired with a different phase-cycle and the scan time remains as short as the time to acquire one single measurement: $t_{tot} = t_{single}$. As all projections in a radial acquisition overlap in the centre of k-space, a major part of the signal from all phase-cycled projections is averaged, leading to an effect similar to complex sum combination. Nevertheless, the images resulting from a radial acquisition will suffer from a loss in signal intensity as all lines differ in phase and can interfere destructively.

Furthermore, it is possible to use a k-space weighted image contrast filter (KWIC-filter) which allows reconstructing multiple images at different positions in the offresonance profile from one frequency-modulated acquisition. In this case, the combination methods for phase-cycled bSSFP measurements described in section 2.3 can be applied as well (46).

A more advanced algorithm, the multifrequency reconstruction, which allows conserving the initially high signal level, was invented and is described later in this work (see Chapter 5).

2.4.1 Signal behavior

Due to the constantly changing situation, the current magnetization in a frequency-modulated bSSFP (fm-bSSFP) experiment strongly depends on the past and cannot be described analytically. Nevertheless, simulations of the signal evolution allow an investigation of the behavior with changing parameters.

In general, the offresonance profile of an fm-bSSFP experiment is similar to the standard bSSFP behavior. Characteristic features, like periodicity or distinct signal drop-outs are preserved. The main difference is a distortion and asymmetry introduced by the frequency modulation. The profile becomes more asymmetric and the plateau narrows to peaks with increasing step size ψ as shown in Figure 8. Additionally, faster changes prolong the transient phase and thus slow the formation of new states. The profiles seem shifted. Furthermore, a linear trend is introduced in the phase behavior.

Apart from that, the overall signal behavior is similar to standard bSSFP as described in section 2.2.5.

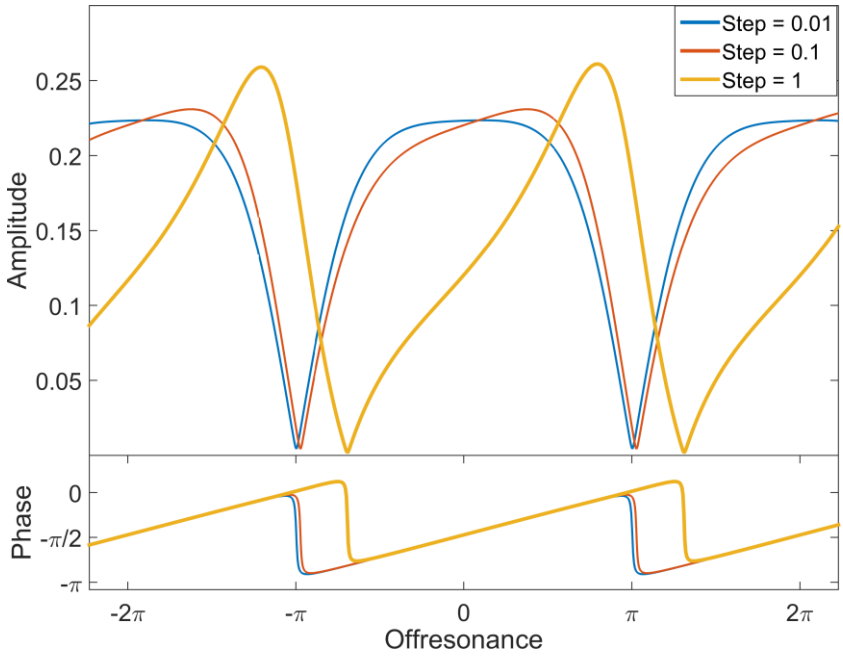

Figure 8: fm-bSSFP signal behavior at TE = TR/2 for $\alpha = 50°$, $T_1 = 1000ms$, $T_2 = 200ms$ and TR $= 4ms$ after 500 preparation pulses. With increasing quadratic increment the asymmetry and attenuation increase.

The overall signal level rises with decreasing flipangle and the now tilted plateau widens (see Figure 9). When a critical value is reached a dip starts forming around zero offresonance. Here, due to the overall asymmetry, the maxima are not equal anymore. The signal phase shows a linear trend and sudden jumps at the position of the signal Nulls.

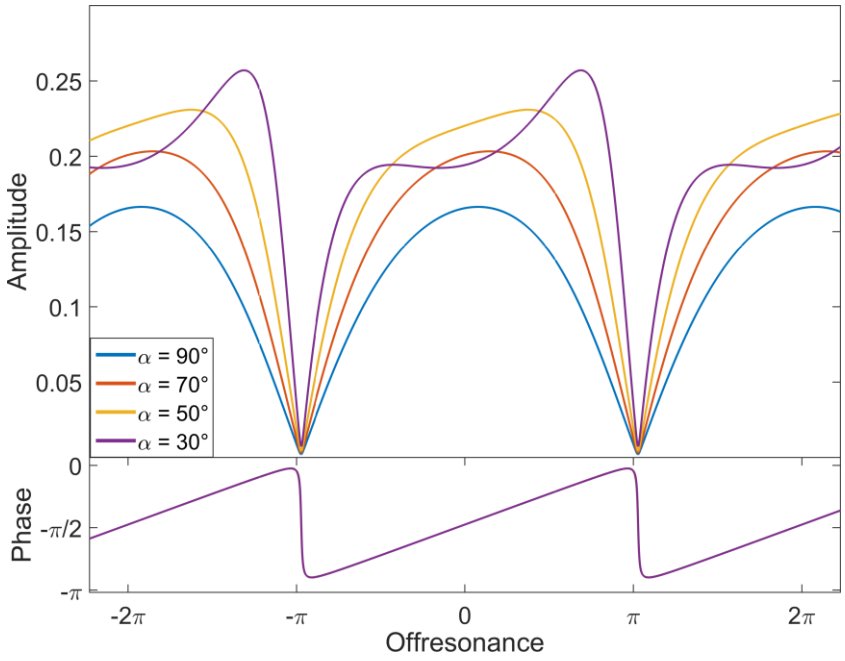

Figure 9: fm-bSSFP signal behavior at TE = TR/2 for $T1 = 1000ms, T2 = 200ms$, TR $= 4ms, \psi = 0.1$ after 500 preparation pulses. The shape of the offresonance profile varies with flipangle. For decreasing flipangle the asymmetry increases and onresonant signal level rises. At a certain angle, depending on T_1/T_2, a dip starts forming which leads to the maximum signal intensity being shifted away from zero offresonance. The phase behavior is independent of the flipangle.

Here too, a higher or lower T_1/T_2 ratio will decrease or increase the overall signal intensity, respectively (see Figure 10). As before, the T_1/T_2 ratio changes the optimal flipangle and therefore the signal shape for a given flipangle. But in contrast to standard bSSFP the profiles with two different sets of T_1 and T_2 are not identical anymore. Although overall signal intensity is comparable, higher values introduce a stronger asymmetry, probably due to the strong dependence of the current magnetization on its history. A flattening in the signal magnitude also translates to smoothing of the sudden jumps in phase.

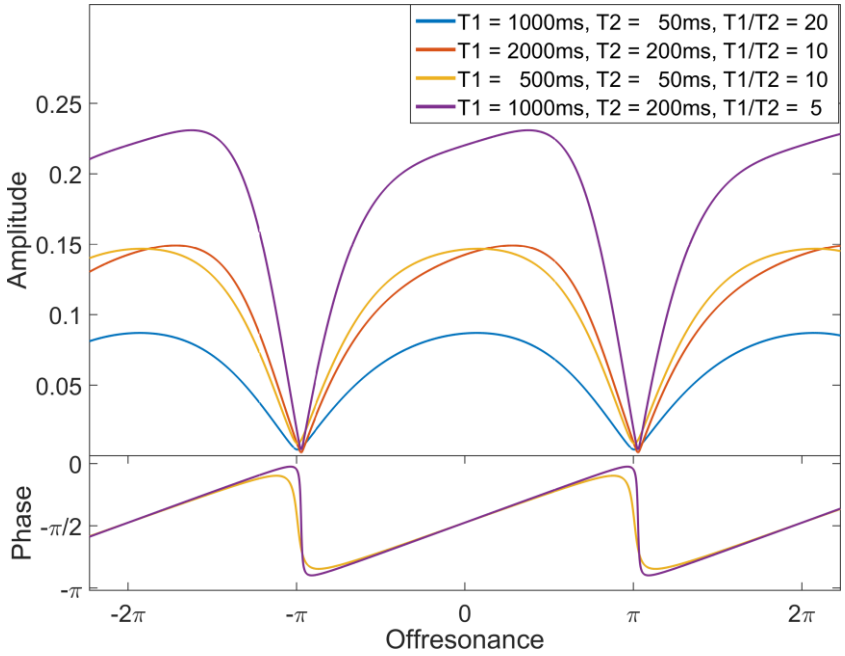

Figure 10: fm-bSSFP signal behavior at TE = TR/2 for $\alpha = 50°$, TR $= 4ms$ and $\psi = 0.1$ after 500 preparation pulses. The shape of the offresonance profile varies with T_1 and T_2. With increasing T_1/T_2 the signal level decreases. In contrast to standard bSSFP choosing different value pairs for T_1 and T_2 with the same ratio does affect the signal. The phase behavior is independent.

In analogy to standard bSSFP, the choice of TR does not influence the bSSFP offresonance profile in shape or height but only in its periodicity (Figure 11).

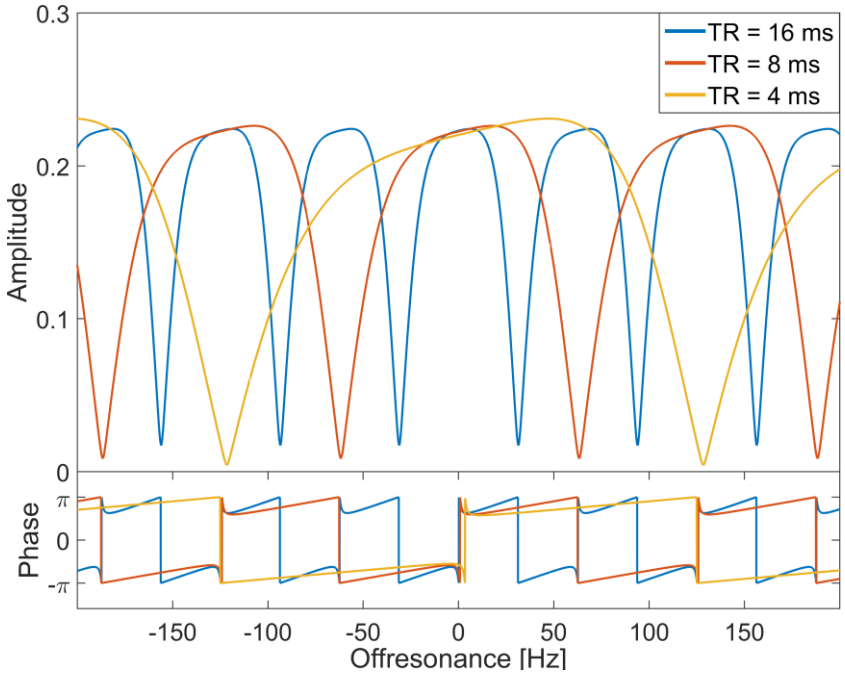

Figure 11: fm-bSSFP signal behavior at TE = TR/2 for $\alpha = 50°$, $T_1 = 1000ms$, $T_2 = 200ms$ and $\psi = 0.1$ after 500 preparation pulses. As in standard bSSFP decreasing TR increases the period of magnitude and phase behavior in the offresonance profile.

2.5 Comparison of phase-cycled and fm-bSSFP

The main difference in the application of the phase-cycled and frequency-modulated approaches is the minimum measurement time. While multiple instances of k-space need to be filled in the phase-cycled approach, only one single k-space is acquired in frequency modulation. Therefore, the total scan time in the latter is lower by a factor of N_{pc} (the number of acquired phase-cycled images). The minimum N_{pc} necessary for sufficient banding suppression depends on the severity of the field distortions. Generally, higher N_{pc} provides a more robust banding suppression but also longer scan times. Thus, the number of acquired phase-cycled images is always a tradeoff between image quality and acquisition time. In a frequency-modulated measurement the ellipse in the complex plane is always sampled at N_{proj} points. As in general $N_{proj} >> N_{pc}$ a robust removal of bandings can be expected almost independent of the severity of the initial distortions of the magnetic field. Both methods will fail in the case of inhomogeneity so strong, it causes significant intravoxel dephasing. In a phase-cycled measurement a fixed number of images is acquired at preset offresonances, which cannot be altered after the acquisition. The dynamic fashion of the frequency modulation collects data at many different offresonance values and allows retrospective reconstruction of images at arbitrary shifts of the offresonance profile. As only a part of k-space is collected at each point, only undersampled images are available at any given position or a filter is needed to introduce a weighting favoring the desired offresonance.

2.6 Signal simulation

Simulations present a convenient way to examine the behavior of a spin ensemble during a specific MRI sequence. While a measurement only provides the resulting state at a given time point (whenever the receiver is open), simulations allow investigating arbitrary time points and tracking the signal evolution over time. All input parameters, e.g. material properties like relaxation times or sequence parameters like flipangle, repetition time or echo time, can be chosen freely and independently. This allows the investigation of a large range of parameter combinations without the need for dedicated phantoms and without hardware or software limits. The impact of changing one parameter is directly discernible as no complex side effects or interdependencies are taken into account. All in all, they can often provide a time and cost-saving alternative to real measurements.

MRI uses the influence of RF pulses and magnetic field gradients on the magnetic moments of protons to generate an output signal. In macroscopic physics, such interactions are described by the Bloch equations. Each MRI measurement consists of a set succession of such gradients and pulses which influence the matter to be imaged. To simulate the signal resulting from such an experiment,

the behavior of the spin ensemble can be calculated step by step using matrix transformations, based on the Bloch equations.

2.6.1 Bloch equations

The Bloch equations are a set of differential equations first published by Felix Bloch in 1946 (60). They provide a macroscopic description of the behavior of a great number of nuclei in a sample of matter influenced by two external magnetic fields: a strong constant field and a weak radiofrequency field perpendicular to it. Within this setting the change of the nuclear magnetization $M = (Mx, My, Mz)$ over time can by described as follows (19):

$$\frac{dM}{dt} = \gamma\, Mx\bar{B} - \frac{M_x}{T_2} e_x - \frac{M_y}{T_2} e_y - \frac{M_z - M_0}{T_1} e_z \qquad [17]$$

Where γ is the gyromagnetic ratio, T_1 and T_2 are the characteristic relaxation times for longitudinal and transversal relaxation, respectively. M_0 describes the constant part of the magnetization and $\bar{B}$ the overall magnetic field. Solving the differential equations yields three independent dynamics: T_1-relaxation, T_2-relaxation and free precession.

To describe the evolution of the Magnetization between two points in time the combined effect of all three dynamics must be considered. In matrix notation the magnetization $M(t + \tau)$ at time $t + \tau$ can be calculated from the magnetization $M(t)$ at time t (61):

$$M(t + \tau) = A * M(t) + B \qquad [18]$$

where A is a 3x3 matrix and B a 3x1 vector. In general, both A and B depend on relaxation parameters and different rotation and precession angles.

2.6.2 bSSFP signal simulation

The matrix formalism, first described by Jaynes (62), is often used to characterize the magnetization behavior in bSSFP simulations (3,5,61). A clear and descriptive explanation was given by Hargreaves (63) and is summarized in this section.

The bSSFP sequence consists of evenly spaced excitation pulses and a balanced gradient scheme (for details see section 2.2.1). Within one TR the total gradient moments on all axes are zero, which means their overall effect within one TR is zero (see Figure 1). Neglecting motion, to simulate a bSSFP experiment only excitation, relaxation and free precession need to be considered.

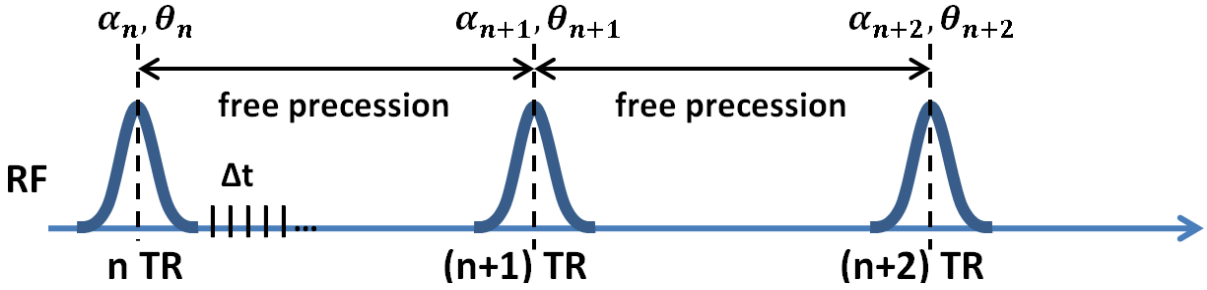

Figure 12: Simplified sequence diagram for simulation. As all gradients are balanced, only RF pulses and free precession are considered. Each pulse is characterized by its flipangle α and its direction in the x-y-plane θ. Δt represents the temporal resolution of the simulation.

In the context of these simulations all RF pulses are assumed to be very short and all effects on the magnetization instantaneous. This allows to separate the time course into basic units Δt and apply the Bloch equation as piece-wise constant functions. Therefore, the equation for each time step can be explicitly solved and applied successively.

Excitation of the spins with a flipangle of α by a pulse from direction θ can be described as a rotation about an axis in the x-y-plane using the rotation matrix F:

$$F(\alpha,\theta) = \begin{pmatrix} \cos^2\alpha + \sin^2\alpha * \cos\theta & \sin\alpha * \cos\alpha\,(1-\cos\theta) & \sin\alpha * \sin\theta \\ \sin\alpha * \cos\alpha\,(1-\cos\theta) & \sin^2\alpha + \cos^2\alpha * \cos\theta & -\cos\alpha * \sin\theta \\ -\sin\alpha * \sin\theta & \cos\alpha * \sin\theta & \cos\theta \end{pmatrix}$$

The precession of the spins can be described likewise, as a rotation around the z-axis. Matrix notation supplies the rotation matrix around the z-axis by an angle of ϕ:

$$Rz = \begin{pmatrix} \cos(\phi) & -\sin(\phi) & 0 \\ \sin(\phi) & \cos(\phi) & 0 \\ 0 & 0 & 1 \end{pmatrix}$$

In this experiment, the vector B in Equation [18] considers the effects of the longitudinal relaxation within one timestep Δt, while matrix A describes both longitudinal and transversal relaxation phenomena within Δt and can include precession effects as well. For simulating the shown bSSFP experiment A, B and ϕ ought to be set up as:

$$\phi = 2 * \pi * \Delta f * \Delta t \quad [19]$$

$$A = \begin{pmatrix} E_2 & 0 & 0 \\ 0 & E_2 & 0 \\ 0 & 0 & E_1 \end{pmatrix} * \begin{pmatrix} \cos(\phi) & -\sin(\phi) & 0 \\ \sin(\phi) & \cos(\phi) & 0 \\ 0 & 0 & 1 \end{pmatrix} \quad [20]$$

$$B = \begin{pmatrix} 0 \\ 0 \\ 1 - E_1 \end{pmatrix} \quad [21]$$

$$E_1 = e^{-\frac{\Delta t}{T_1}}, \; E_2 = e^{-\frac{\Delta t}{T_2}}$$

After defining a starting magnetization M_0 ($usually\ M_0 = M_z = 1$) and setting values for flipangle α, longitudinal relaxation T_1, transversal relaxation T_2, offresonance Δf and temporal resolution Δt, the signal evolution is calculated step by step in a recursive fashion. Simulation of the signal evolution between nTR and $(n+1)TR$ consists of the following steps (see Figure 12):

RF-Excitation at time point nTR (blue line Figure 13 a)

- Rotation of the magnetization by α_n about an axis in the x-y-plane
- $M(nTR + \Delta t) = A * F(\alpha_n, \theta_n) * M(nTR) + B$

Free precession for time $nTR + \Delta t$ to $(n+1)TR$ (purple line Figure 13 a)

- Relaxation and free precession
- $M(nTR + 2\Delta t) = A * M(nTR + \Delta t) + B$
- $M(nTR + 3\Delta t) = A * M(nTR + 2\Delta t) + B$
- …

RF-Excitation at time point $(n+1)TR$ (red line Figure 13 a)

- Rotation of the magnetization by α_{n+1} about an axis in the x-y-plane
- $M((n+1)TR + \Delta t) = A * F(\alpha_{n+1}, \theta_{n+1}) * M((n+1)TR) + B$

…

Figure 13 b shows the signal evolution in the following TR interval between a $-\alpha$ pulse at $(n+1)TR$ and a $+\alpha$ pulse at $(n+2)TR$. The signal is most commonly collected at $TE = TR/2$.

In this simplified depiction slice-encoding, phase-encoding or readout gradients are neglected. Each gradient would cause internal dephasing of the spin ensemble. As the main feature of bSSFP is the balanced gradient scheme, this dephasing is completely rewinded whenever the overall gradient

moment is zero, which is true just before and after each RF pulse. Assuming the signal is collected at $TE = TR/2$, dephasing is minimized (17).

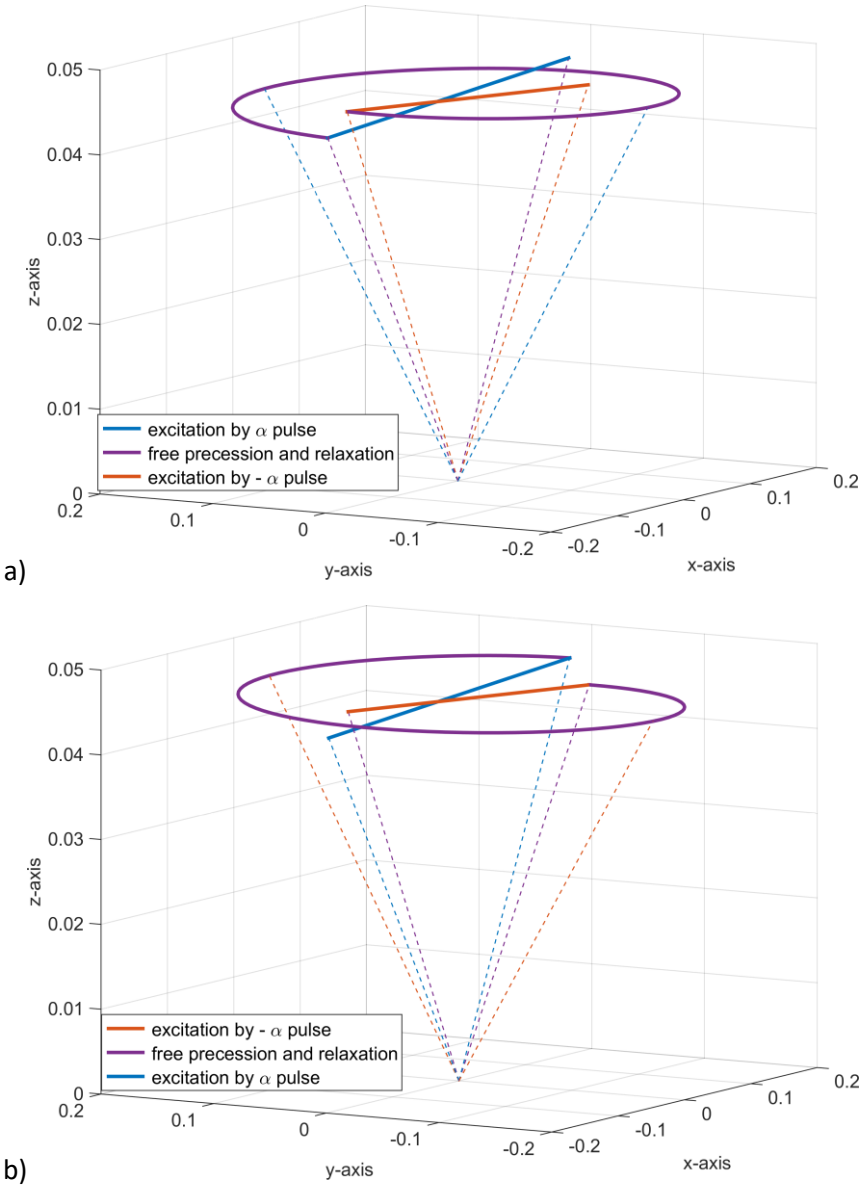

Figure 13: Evolution of magnetization in a standard bSSFP simulation. Example simulated using $\alpha = 50°$, $T_1 = 800\ ms$, $T_2 = 100\ ms$, $TR = 4\ ms$, $TE = 2\ ms$, $\Delta t = 0.05\ ms$, onresonant. Shown are two TR intervals after the steady state was fully established. a) The α pulse (blue) tips the magnetization by the flipangle α and is followed by a period of free precession and relaxation (purple). During one TR, i.e. between two pulses, the magnetization precesses around the z-axis. Relaxation processes increase the component in z-direction while the transversal component shortens. The $-\alpha$ pulse (red) starts the next TR interval. b) The $-\alpha$ pulse tips the magnetization (red) and is again followed by free precession until the next α pulse. This alternating behavior is repeated until the end of the acquisition. To simplify the depiction all dephasing by slice selecting, phase encoding or readout gradients is neglected as the balanced nature of the sequence ensures rephasing.

2.7 Data acquisition in k-space

In an MRI measurement the signal is not collected directly as an image but in the Fourier space, also called k-space. In order to obtain images free of artifacts, the Nyquist theorem needs to be fullfilled. In general, the Nyquist criterion states that the sampling rate needs to be at least twice as high as the highest frequency in the signal (19). For MRI it links the distance between two values sampled in k-space (Δk) to the FOV to be acquired:

$$FOV \propto 1/\Delta k \quad [22]$$

Additionally, the maximum extend of the k-space measured (kmax) determines the resolution (Δx) in the final image:

$$kmax = n * \Delta k \propto 1/\Delta x \quad [23]$$

Thus, a sufficient number of data points must be collected to fill the k-space of a given FOV with a given resolution. To omit points in k-space, also called undersampling, leads to artifacts in the image. If the undersampling follows a specific pattern, like missing lines or wedges, distinct types of artifacts occur.

The way k-space is filled can vary and different patterns, called trajectories, are common in MRI imaging. Most prevalent is a Cartesian trajectory, covering k-space line by line (Figure 14 a top). A Cartesian acquisition can be easily reconstructed by simple Fourier transformation (FT) and is robust towards eddy currents or gradient delays. On the other hand, it often suffers from aliasing or wrap-around artifacts, requires long scan times and is sensitive to motion during the acquisition. Another common method, especially in scientific setups, is the radial trajectory, where all lines are acquired similarly to spokes of a wheel in set angles (Figure 14 a top). As all lines traverse the center of k-space, it is insensitive towards motion or flow artifacts and produces incoherent artifacts in case of missing signal points. But the changing direction of acquisition renders it more sensitive to eddy currents and gradient delay artifacts. Furthermore, reconstruction of a radial sampling scheme requires a gridding operation prior to FT or a nonuniform FT. Both schemes can be extended to the acquisition of a three dimensional k-space as well (Figure 14 b, c). Exciting a whole 3D block has the advantage of a high SNR, the possibility to acquire thin slices and reconstruct slices in arbitrary planes as well as overlapping slices. The phase encoding of two directions in general prolongs scan time.

A multitude of other trajectories have been proposed over time, further examples are rosettes (64), lissajous patterns (65), concentric ring or the spiral trajectory (66).

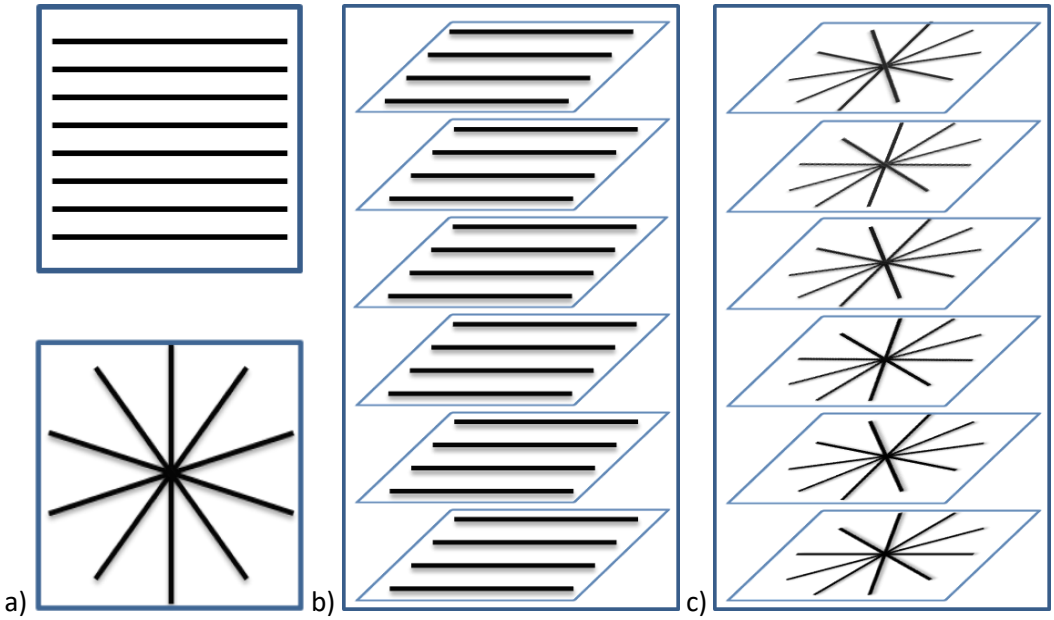

Figure 14: Examples for k-space trajectories in MRI. a) A Cartesian sampling scheme (top) sampling k-space in parallel lines and a radial sampling scheme (bottom), where each read-out line traverses the center of k-space, analog to spokes of a wheel. b) The 3D Cartesian sampling pattern multiplies the 2D plane by adding a second phase encoding direction perpendicular to the plane. c) 3D radial sampling scheme, also called stack of stars, multiplies the radial sampled 2D plane in the third dimension.

2.7.1 Cardiac acquisition

The main challenge in cardiac imaging is the heartbeat. Usually, an electrocardiogram (ECG) is acquired during the MRI acquisition and based on the ECG signal the sequence can be gated, either prospectively or retrospectively. For the prospective approach, the ECG signal is used as a trigger for the pulse sequence. One predefined part of the imaging sequence (e.g. one part of k-space) is played out during a preset imaging window after the trigger event, usually in the diastole. The length of the imaging window needs to be carefully chosen, in order to allow for a sufficiently large part of data to be acquired, but not to be too long and miss the next trigger event. This can be especially challenging in cases of arrhythmia.

Another approach uses the logged ECG data to retrospectively accept, reject, interpolate or resort the acquired data. In CINE imaging (67) the heartbeat is divided into several cardiac phases according to the logged ECG. Now for each cardiac phase, k-space lines acquired during multiple heartbeats can be combined into one k-space. For radial acquisitions, this can be achieved by collecting single lines or segments. The first possibility continuously acquires spokes spaced one golden angle apart over multiple heartbeats and retrospectively combines all spokes acquired within

one cardiac phase (Figure 15 a). Due to the nature of golden angle spacing, each line provides new information but only a subset of consecutively acquired lines will uniformly sample k-space, which is not given in the case of retrospective selection of disconnected subsets. To ensure an even distribution in k-space, a small subset of spokes can repeatedly be collected during one heartbeat followed by the next subset during the next heartbeat (Figure 15 b).

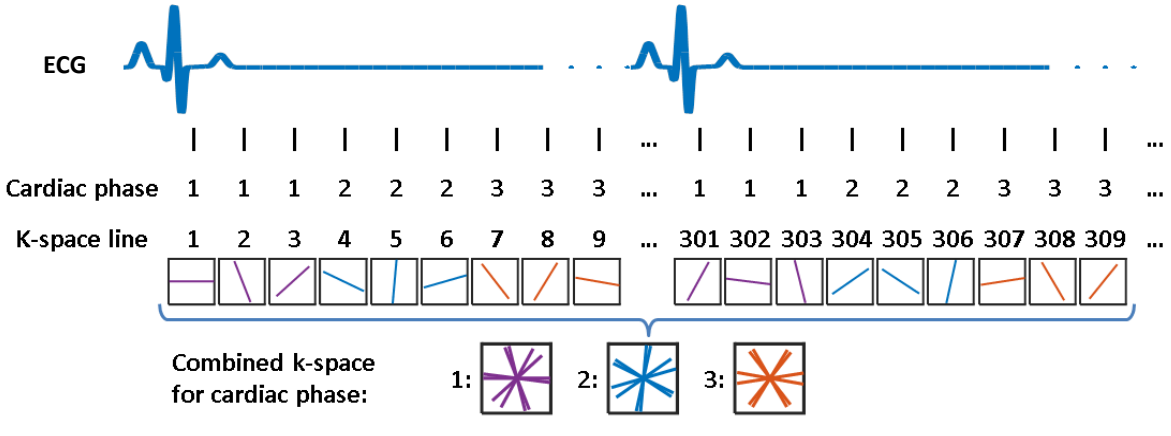

a)

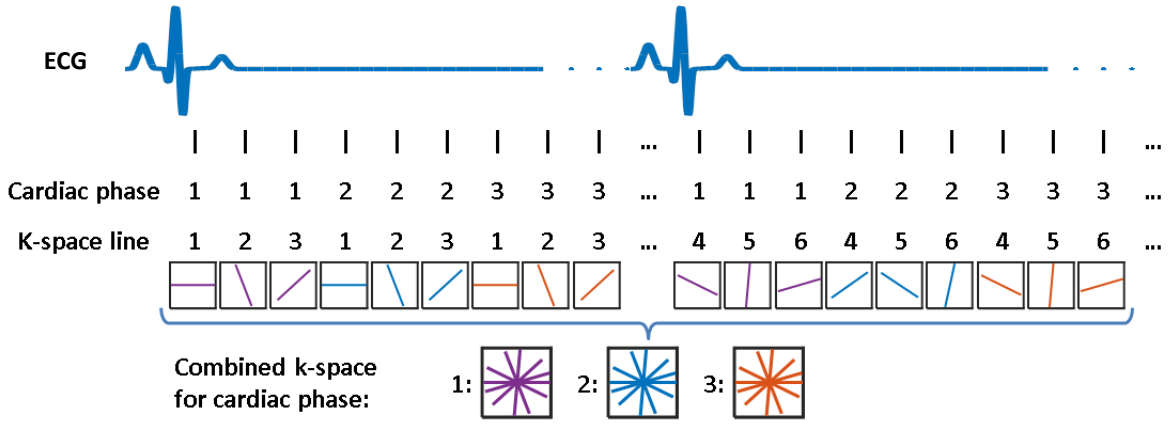

b)

Figure 15: Acquisition schemes for CINE imaging. a) radial spokes are sampled with a continuous golden angle increment thus creating unique spokes that complement the information in all previous spokes. After acquisition, all lines acquired in the same heartphase (e.g. purple, blue or orange) are collected to form one image. Note that retrospective reordering can cause spokes with similar angles to be grouped and therefore uneven coverage of k-space. b) radial spokes are collected in a segmented fashion. While here not all spokes are unique, retrospective reordering will create a good distribution of angles.

2.8 Water-Fat separation

The main components of the human body, visible in the MRI, are water and fat. To distinguish between the two different tissues in the final image can be of high diagnostic relevance. As fat has a comparably high signal intensity in most acquisition techniques, it can dominate the image and overlay other important structures. Thus, it is desirable to exclude the fat signal from the image, either during acquisition or in a subsequent image processing step. Furthermore, it can be of diagnostic relevance to conclude the composition of a specific tissue from the image (68).

2.8.1 Chemical shift

The backbone of MRI are spins rotating in the magnetic field with a distinctive frequency. The Larmor frequency is defined by the gyromagnetic ratio and the local magnetic field of the spin considered:

$$\omega = \gamma * B_0. \qquad [24]$$

As each proton within a molecule is set in a slightly different microscopic environment, the resonance frequency can change. The total change Δf is proportional to the resonance frequency f of the respective proton. To describe this chemical shift the resonance frequency of a proton in tetramethylsilane ($Si(CH_3); TMS$) is set as a reference value ($\delta = 0$). For all other materials the chemical shift is given relative to this reference and usually stated in parts per million [ppm]. It can be calculated as:

$$\delta\,[ppm] = (f - f_{TMS})/f_{TMS} \qquad [25]$$

where f is the resonance frequency of the substance in question and f_{TMS} the resonant frequency of the reference TMS. The two ^1H nuclei in pure water have an identical chemical shift of $\delta = 4.7\,ppm$. In organic tissues multiple protons are bound in different microscopic settings, resulting in different δ. In subcutaneous fat at least six different peaks can be identified by spectroscopic means (69). The methylene (CH_2) peak has the highest intensity and is shifted by $\delta = 1.3\,ppm$. Overall combination of all fat peaks results in a broad spectrum ranging from $\delta = 0.9\,ppm$ to $\delta = 5.7\,ppm$. Despite this rather complex spectrum, for measurement purposes the chemical shift between water and fat is commonly approximated as 3.3 to $3.5\,ppm$ as the main peak dominates the fat spectrum.

2.8.2 Separation procedures

To achieve a separation of water and fat in the final image, many different strategies were proposed (68,70,71), from suppression of fat during the excitation to complex post-processing strategies.

As water and fat have different resonance frequencies, the spins in the different tissues can be excited separately. Therefore, the radiofrequency pulse can be shaped to result in a rectangular function in the spectral domain, centered around the major fat peak and not touching the water peak. Such a chemically selective fat suppression pulse can crush the transversal magnetization in fat-protons, leaving the magnetization of water protons intact (72). Another way is the breakdown of the excitation pulse into several small steps, tipping the magnetization only by a small angle at a time. With carefully adjusted timing these so-called spatial-spectral pulses, will constructively add up for water spins but cancel each other out for fat spins (73). Both methods can be combined with any pulse sequence but are sensitive to field inhomogeneities as they rely on the existence of specific frequencies for both tissues.

The short TI inversion recovery technique exploits the difference in relaxation time between water and fat. After an initial inversion pulse, the acquisition is timed in such a way that the magnetization from fat is nulled, thus providing reliable suppression in the final image (74). Relaxation times are independent of field inhomogeneities but introduce, a possibly unwanted, T_1 weighting in the image.

Fundamentally different approaches separate the signal originating in water and fat after the acquisition, instead of avoiding the formation of a signal in fat altogether. The most common post-processing algorithms, known as DIXON separation, rely on the difference in phase between signals acquired in water and signals acquired in fat. Two to four images are collected at different echo times to encode the phase information. Combination of these can not only provide fat-suppressed images but also water-suppressed images for the same acquisition (70). While the procedure of a two-point DIXON algorithm again suffers from field inhomogeneities, three or four point techniques are robust towards it. The main drawback of DIXON like methods is the long scan time.

With the recent rise of interest in steady-state gradient echo sequences the possibilities for combining these with fat suppression or water-fat separation techniques were explored. In general bSSFP sequences are compatible with all common fat-suppression acquisition techniques, e.g. selective pulses (75,76), magnetization preparation (77,78) or multi-echo (79). Additionally, images can be post-processed using DIXON like algorithms (80,81) to gain water and fat images.

Due to the dependence on offresonance, the signal behavior of bSSFP in itself is highly interesting for water-fat separation (9,79,82,83). As the dephasing in a bSSFP experiment depends on TR (see Equation [2]), adjustment of the TR value allows the positioning of water and fat signal at a set distance in the offresonance profile. In case of known local resonance frequency, it is thus possible to place the water signal at the position of maximum intensity, while the fat signal is nulled (Figure 16). In a real setting, the exact value is hardly ever known and varies over the FOV rendering this technique unfeasible for fat suppression. But, although the definite position remains unknown, the difference in offresonance is given by the chemical shift. The TR value, therefore, remains a mean to control the relative positions in the offresonance profile, e.g. spacing water and fat a set number of passbands apart (Figure 17). This feature is exploited in a phase sensitive separation procedure.

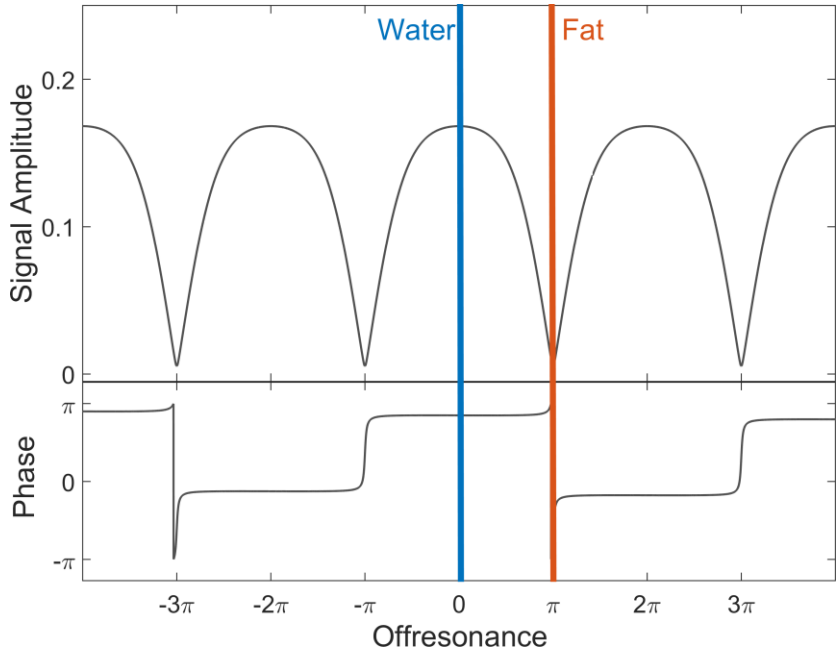

Figure 16: bSSFP offresonance profile for water (blue line). Shown is the respective position of the main fat peak (red line). Note the difference in magnitude caused by the different resonance frequencies of water and fat. For the settings shown here, the fat signal can even be suppressed as it is placed in the stopband, while water signal is maximized.

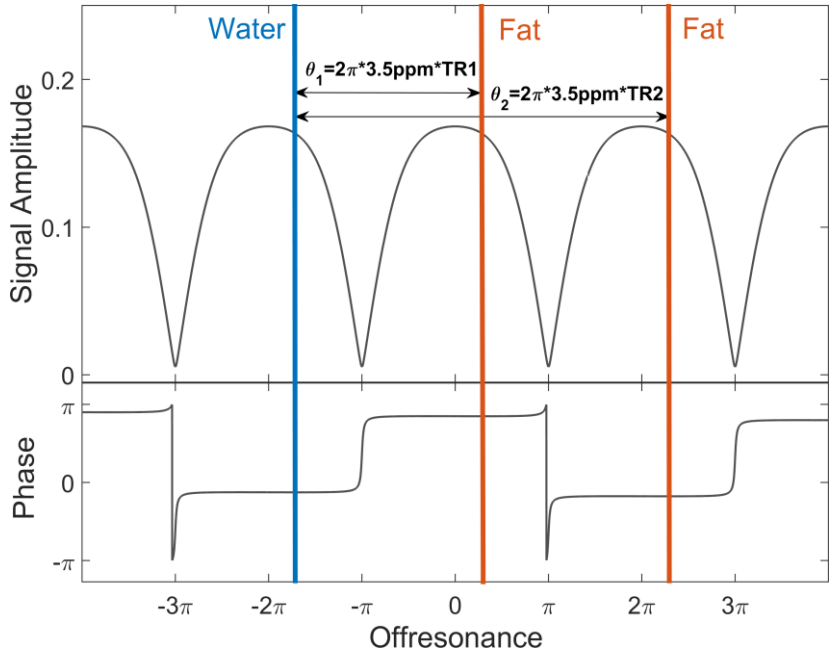

Figure 17: bSSFP offresonance profile for water (blue line). As the offresonance is connected to the TR of the measurement, the position of the main fat peak, in relation to the water peak, can be shifted by adjusting TR. Shown are two examples where the distance between water and fat equal one (for TR1) or two (for TR2) periods of the bSSFP profile.

2.8.3 Phase-sensitive water-fat separation

As shown before, the TR value can be used to define the distance between water and fat in the offresonance profile. If TR is chosen as the reciprocal of the chemical shift $TR1 = 1/(\delta_{water} - \delta_{fat})$ the signal from water and fat is placed in adjacent passbands. As each signal null is accompanied by a phase jump of π this distance will create a phase difference between the two tissues (e.g. TR1 in Figure 17). The same is true for any odd multiple n of TR1: $TR = n/(\delta_{water} - \delta_{fat})$. For even multiples there is no phase difference (e.g. TR2 in Figure 17).

In the phase-sensitive water-fat separation approach (84–86) such a phase difference is deliberately created by appropriate choice of TR and consequently exploited to separate the signals originating from water or fat. Unfortunately, a phase jump can also be caused by field inhomogeneities within one and the same tissue, leading to inconclusive allocations. To remedy these swaps a dual acquisition approach for a phase sensitive separation was suggested (87). Here, two standard bSSFP acquisitions are acquired in a phase-cycled manner, such that the difference in offresonance is 180° or π. Subsequent combination via complex sum leads to a smoother magnitude and a linear phase behavior, but the initial difference in phase of π is preserved (Figure 18).

Depending on sequence and tissue parameters residual rippling is visible in the signal of a dual acquisition. It is known that residual oscillations decrease with increasing number of individual phase-cycled images, which are combined (51). A frequency-modulated acquisition covers a broad range of frequencies and combines them in one image, therefore signal magnitude and phase show a smooth behavior while the water-fat phase difference still pertains (Figure 19). A more thorough comparison between phase-cycled and frequency-modulated acquisitions is given in section 2.5.

Images from either dual-acquisition or frequency-modulated bSSFP show two distinct phase patterns. First, slowly varying phase along changes in the magnetic field, and second, phase jumps of π at water-fat interfaces. For a robust separation the slowly varying component can be eliminated using block regional phase correction (87,88).

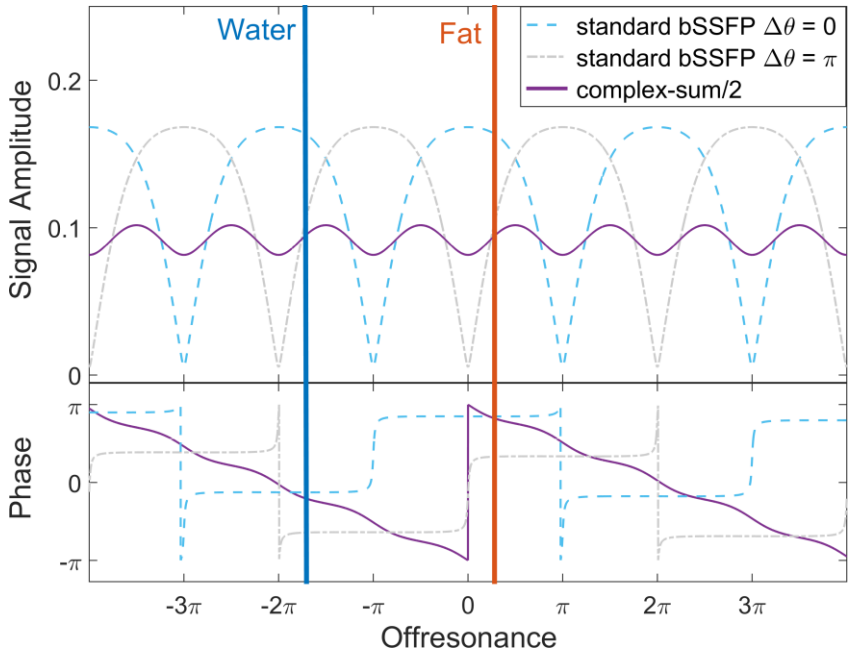

Figure 18: Water and main fat peak in the offresonance profile of two phase-cycled bSSFP experiments and their complex sum combination. TR is chosen such that the distance equals one period of the profile. Noteworthy is the difference of π in the phase of water and fat peak, which always establishes at this specific distance.

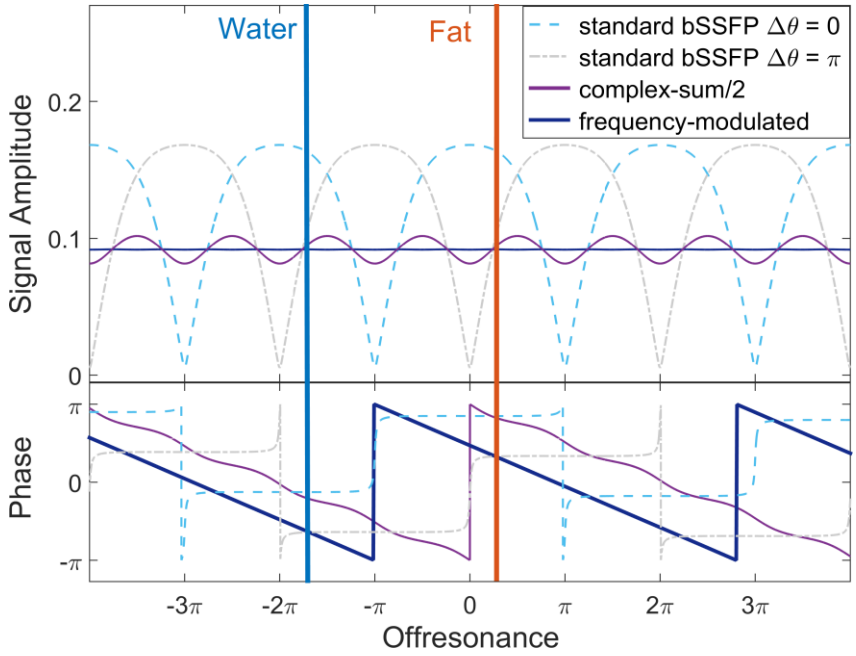

Figure 19: Water and main fat peak in the offresonance profile of two phase-cycled bSSFP experiments, their complex sum combination and frequency-modulated bSSFP with similar parameters. Again, TR is chosen such that the distance equals one period of the profile. Signal behavior with offresonance is similar for fm-bSSFP and complex sum signal, with the complex sum showing ripples not present in fm. The phase difference of π, important for the separation algorithm, is retained in fm.

2.8.3.1 Block regional phase correction

A vital part of the phase sensitive separation technique is the distinction between phase differences caused by offresonance and differences caused by a change of tissue. The former is expressed as a slowly varying change while the latter produces sudden jumps of π. To accomplish the distinction a block regional phase correction algorithms, first described by Ma (88), was modified and employed (87). The resulting region growing algorithm eliminates slowly varying components as well as jumps of 2π caused by phase wrapping. Jumps of 1π are preserved. Firstly, the image is divided in blocks of several pixels, (e.g. 4 x 4px in 2D or 4 x 4 x 4px in 3D) and a so-called block-phase is assigned. To determine the block phase, the complex signals of all pixels in the block are plotted in the complex plane. In this scatter plot a straight line is fitted by linear interpolation with the constraint of crossing the origin. The angle of the fitted line provides the block phase. Secondly, a map of the slowly varying component is obtained by initially removing phase jumps of π. Starting from a chosen start block, the algorithm moves outward, always updating the phase of the block nearest to the already corrected area. Phase of π is added to the current block if necessary in order to keep it within small range to the neighbouring pixels. In the final step the so obtained map of slowly varying changes is substracted from the original image. The result is an image with an almost binary phase distribution of values close to 0 or π.

3 Material and Methods

This chapter focuses on the practical implementation of MRI measurements to gain the results shown in chapters 4, 5 and 6. All settings mentioned here are generally valid for all acquisitions, next to the specific parameters given in the respective chapters. First, the measurement procedure is explained in section 3.1 and an overview of the different employed trajectories is given in section 3.2. Next, section 3.3 provides details on the bSSFP pulse sequence and its modifications to allow for phase-cycled and frequency-modulated imaging. After collection of the raw data from the MRI scanner, a standard reconstruction is performed for all measurements as explained in section 3.4. Specialized reconstruction schemes for fm-bSSFP or water-fat separation are elucidated in the following chapters. Section 3.5 focuses on the shimming procedure and section 3.6 provides details on SNR determination to compare the established methods.

3.1 Measurement procedures

All measurements were performed at the university hospital in Würzburg, were three MRI scanners are available for research purposes, 1.5T MAGNETOM Aera, 3T MAGNETOM Skyra and a 3T MAGNETOM Trio, now upgraded to 3T MAGNETOM Prisma. For phantom measurements, differently shaped plastic containers filled with deionized water and $NiSO_4$ are available, as well as a structured phantom containing various plastic compartments and wedges of different shape and size. Additionally, a phantom containing deionized water and vegetable oil was constructed.

For all in vivo measurements, healthy volunteers and approval of the local ethics committee were acquired. The procedure complies with the regulations of the Declaration of Helsinki and informed consent was obtained from all volunteers before scanning.

An overview of all measurements, parameters and scanner settings is given in the Appendix. Measured raw data was transferred to a PC workstation, where reconstruction and postprocessing was performed in MATLAB®, using existing functions and code specifically developed as part of this work.

3.2 Trajectories

3.2.1 Cartesian (CART)

In all Cartesian measurements k-space was collected in horizontal lines, filling k-space in linear order from top to bottom (see Figure 14 a top). The number of lines always equals the size of the chosen base matrix. Thus no undersampling due to voids in k-space occurs.

3.2.2 Radial (RA)

When using a radial trajectory, the k-space is traversed on multiple straight lines. Each line starts at the edge of k-space, crosses the center and travels straight on to the opposite edge (see Figure 14 a bottom). To successively fill k-space, multiple lines are collected at various angles. For a standard radial trajectory, a full circle (360°) was divided by the desired number of spokes (N_{proj}) and lines were collected with linearly increasing angles: $angle(line_n) = n * 360°/N_{proj}$. Therefore, the data fills k-space uniformly only at the end of an acquisition.

3.2.3 Radial golden angle (GA)

In all radial golden angle acquisitions, a radial trajectory was collected spacing each line one golden angle apart from the former, with the golden angle being defined as $GA = 2 * \pi \,/\, (\sqrt{5} + 1) \; = 111.246°$ (89). The spacing results in each spoke falling into the largest empty space between the two previous spokes. Therefore, a golden angle trajectory always minimizes the distance between two unsampled points in k-space after each step. This allows to abort acquisitions or retrospectively choose consecutive subsets of the acquired k-space.

3.2.4 Golden angle Stack-of-stars (GA SToST)

All 3D volumes were acquired using a stack of stars trajectory (90). Two dimensions of the k-space were collected in a radial fashion resulting in a star-like pattern. These 'stars' were stacked along the third dimension to cover a cylindrical volume in k-space. Within one star, all spokes are collected in a golden angle fashion and each star is lightly twisted towards the next such that lines covered in one partition do not equal lines covered in a neighboring partition (see Figure 14 c). During one measurement lines were collected in a PAR-IN-LIN fashion, meaning that one spoke was collected in each partition before starting to collect the next spoke within each partition.

3.2.5 Golden angle CINE trajectory (GA CINE)

In cardiac acquisitions, the total number of spokes was divided into several subsets, according to the TR, the estimated length of one heartbeat t_{HB} and the number of heartphases to be reconstructed Hp. One group contained $n_{gr} = \frac{t_{HB}}{Hp * TR}$ spokes. All lines within one group were repeatedly acquired for one heartbeat before the next group was acquired within the next heartbeat (see Figure 15 b). As total measurement time is limited to the length of one breath-hold t_{BH} , the total number of acquired spokes is limited by $N_{proj} \; = \frac{t_{BH}}{TR}$ as well. In the given measurement the total number of lines was set in accordance with the volunteers' ability to hold their breath.

3.3 Frequency modulation and phase-cycling

Within this work, frequency modulation is implemented as a change of phase in the RF- pulse, as an actual frequency modulation would cause slice shifts. As explained in section 2.4 a quadratic term was added to the determination of the RF-phase of the n-th RF pulse (see Eq. [16]). Each frequency-modulated measurement was collected in such a fashion, that one measurement covers one period in the offresonance profile. Therefore, a step width of $ds = 360°/N_{proj}$ was chosen as quadratic increment. The same is true for 3D measurements, were all lines acquired in all partitions are considered together to cover one period.

For comparison, all subjects were also scanned using at least one standard bSSFP measurement. To allow for comparison with different combination algorithms most standard acquisitions were repeated with different phase-cycling. Depending on the total number N_{pc}, these phase-cycled acquisitions were always collected to be evenly spaced across one period of the offresonance profile, i.e. $\Delta\theta(n) = n * 360°/N_{pc}$.

3.4 Standard reconstruction

After conversion of raw data to MATLAB® data, a 2- or 3-dimensional Fourier transform conveys the collected k-space to image space. Standard computer software algorithms include a Fast Fourier Transformation (FFT) which computes the discrete Fourier transform of a sequence. FFT works with discrete data on a grid and can be applied straightforward to data acquired in a Cartesian fashion. However, the position of a data point acquired in a radial acquisition is a continuous value and needs to be transferred to a grid before an FFT can be applied. For standard gridding reconstruction, values were transferred to a grid using self-calibrated GRAPPA operator gridding (91), which was then followed by FFT.

3.5 Shimming

Banding artifacts occur due to inhomogeneity in the magnetic field. Most state-of-the-art MRI systems are equipped with a sophisticated shim system to avoid these inhomogeneities. For many phantom measurements and certain in vivo applications at clinical 1.5T or 3T scanners this shimming is sufficient to supply banding-free images (or parts thereof). To simulate worst-case scenarios, like ultra-high field scanners, high susceptibility variation or technical difficulties in the shim system, the settings were manually manipulated to introduce a linear change of the magnetic field across the FOV. Phantom measurements, shown in Figure 29 and Figure 32, were performed using the tune-up settings, meaning the dedicated fine-tuning for the current setup was not performed. Manipulation

as well as omittance of shim procedures leads to extensive artifacts not common in clinical routine but are employed for testing of the proposed methods.

3.6 Signal to noise ratio

To determine the signal to noise ratio (SNR) in an MR image the signal and noise levels need to be evaluated. Traditionally, region of interest (ROI) based methods are used to determine these in different areas of one image. Especially in vivo MR images cannot be assumed to include large homogeneous areas without physiological modulations and the procedure is not compatible with new acquisition strategies like phased-array coils or parallel imaging (92). Therefore, in a ROI based approach, signal variations cannot be assumed to be caused by noise only. The straightforward approach to obtaining multiple measurements for one pixel would be the acquisition of a high number of similar images. Again, this procedure is limited in its application as patient movement, physiological noise and instrument drift will influence the signal in each pixel and highly prolonged scan times are undesired, especially in a clinical setting.

To calculate image noise propagation through image reconstruction without overly long scan times a pseudo multiple replica method was proposed (93). Next to the actual measurement, the same dataset is acquired without excitation pulses being played out. From this 'noise-only' measurement a noise covariance matrix is determined which describes the level and correlation of noise within the acquired signals. From this matrix an arbitrary number of correctly scaled and correlated random noise data sets can be produced synthetically and added to the acquired k-space. Thus, an image stack of independent image replicas is determined which can then be used for SNR calculations.

All SNR values shown in this work were determined using this pseudo multiple replica method. For each image 100 synthetic noise data sets were calculated using the respective 'noise-only' scans. The so created noise was added to the k-space data and a stack of 100 images was reconstructed. Within this stack the SNR was calculated as:

$$SNR = \hat{S} / \sigma, \qquad [26]$$

where $\widehat{S}$ is the mean pixel value and σ the standard deviation in each pixel.

4 fm-bSSFP and selected applications

This chapter shows measurements using the frequency-modulated scheme and compares it to standard bSSFP acquisitions. The advantages and disadvantages of both variations are discussed as well as specialized applications. Also, two examples of successful employment of a frequency modulation are given. First, the application in real time cardiac imaging and second, the application in measurements with long TR values. Parts of the results were presented at the annual meeting of the ESMRMB (94).

4.1 Measurements

4.1.1 Phantom scan

One slice of 5mm thickness was scanned in a standard phantom using the CART trajectory with a base resolution of 256 x 256 and FOV of 300 x 300mm^2 at a 3T scanner (MAGNETOM Prisma, Siemens Erlangen, Germany). The same slice was then acquired using the RA and GA trajectory with 402 spokes each and the same resolution and FOV. Further measurement parameters were: flipangle $\alpha = 69°$, TR = 4.2ms, TE = 2.1ms, bandwidth: 574Hz/Px. The total measurement time was 1.1s for the Cartesian scan and 1.7s for each radial scan. See Appendix 1) for all details.

Additionally, a metal implant was inserted into the phantom and one transversal slice was acquired at the same 3T scanner, using the GA trajectory, a resolution of 0.7 x 0.7mm^2 and FOV of 300 x 300mm^2. Further measurement parameters were: flipangle $\alpha = 60°$, TR = 5ms, TE = 2.5ms, bandwidth: 574Hz/Px. The total measurement time was 20s. See Appendix 2) for all details.

4.1.2 Cardiac acquisition

One 5mm slice, showing a short axis view of the heart of a healthy volunteer was collected at a 3T MRI scanner (MAGNETOM Trio, Siemens Erlangen, Germany). A total of 6000 spokes were acquired along the GA radial trajectory over 23 heartbeats and during one breath-hold. Other measurement parameters were: flipangle $\alpha = 36°$, TR = 3.48ms, TE = 1.72ms, resolution: 2.3 x 2.3mm^2, FOV: 300 x 300mm^2. The total measurement time was 23s. See Appendix 3) for all details.

4.1.3 Acquisitions using long TR

The structured phantom was scanned at a 3T MRI scanner (MAGNETOM Skyra, Siemens Erlangen, Germany) using different TR values of TR = 8ms, TR = 20ms and TR = 40ms. One 8mm slice was acquired in a GA radial fashion using 1000 spokes. Other measurement parameters were:

flipangle $\alpha = 70°$, TE = TR/2, resolution: 2.3 x 2.3mm^2, FOV: 300 x 300mm^2. The total measurement time was 8, 20 and 40s for the different TR values. See Appendix 4) for all details.

Longer than usual TR values were also used in the acquisition of the lower leg and the water-oil phantom, described in section 6.1.2.

4.2 Sliding window reconstruction

A sliding window reconstruction allows to generate a time series of images in short succession and is especially interesting for real-time imaging (95). The approach was used for the GA cardiac acquisition to track the movement of the heart. One image is reconstructed from 100 consecutive spokes, while the window is shifted by 50 spokes for each image. Thus, two consecutive images share half of the spokes used for image reconstruction. This results in a real temporal resolution of 2.5 images per second and an apparent temporal resolution, or framerate, of 5 images per second.

4.3 Results

4.3.1 Frequency modulation

Frequency-modulated bSSFP was used for Cartesian and radial acquisitions in 2D on a phantom and an exemplary slice is shown in Figure 20. The Cartesian acquisition resulted in aliasing artifacts along the phase encoding direction, due to the varying signal intensity through k-space. Images were not usable for further evaluation or clinical purposes. In radial acquisitions, the varying signal magnitude leads to spokes with very low signal intensity, which translates to streaking artifacts in image space. In a standard radial acquisition, these spokes are concentrated in one area, such that streaking is bundled and directed. As the golden angle acquisition distributes the position of consecutive spokes in k-space, dark areas are substantially smaller and spread out over the k-space. The result manifesting in the image is less severe streaking spread out in various different directions. In general, these radial artifacts are incoherent and less detrimental to the image.

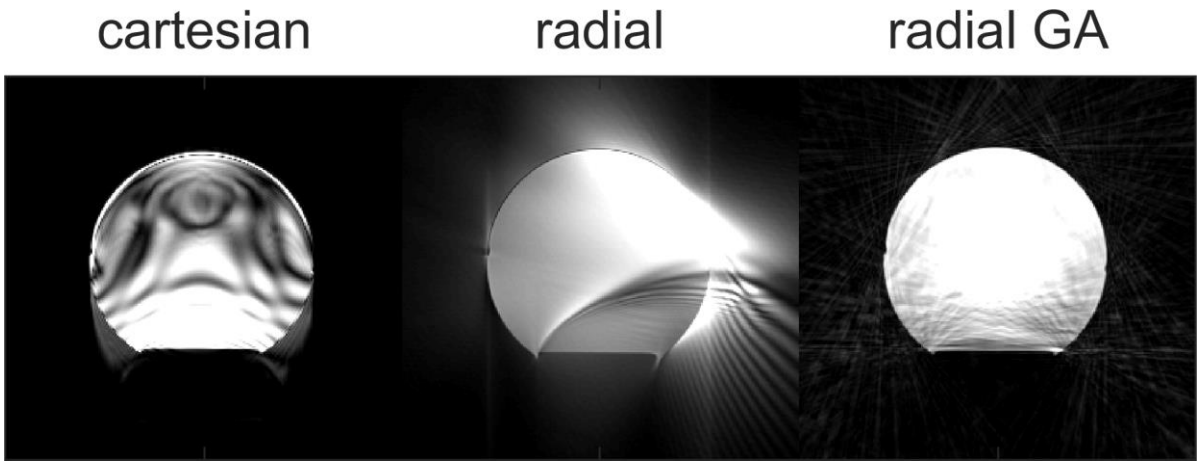

Figure 20: fm-bSSFP for different trajectories. The varying signal intensity in fm-bSSFP causes undersampling artifacts typical for each sampling scheme: aliasing in Cartesian sampling and streaking in radial sampling.

The combination of fm-bSSFP with a golden angle radial trajectory can provide images with suppressed bandings, as shown for various examples throughout this work. In cases of severe distortions of the magnetic field, like in the presence of metal objects, residual banding can remain even in fm-bSSFP. One example is given in Figure 21, where inhomogeneity is caused by a metal implant. Standard bSSFP shows the typical shape of banding artifacts distributed over a large area of the phantom. In fm-bSSFP, banding is suppressed, except for the region close to the phantom. Additionally, an overall loss in signal intensity is apparent.

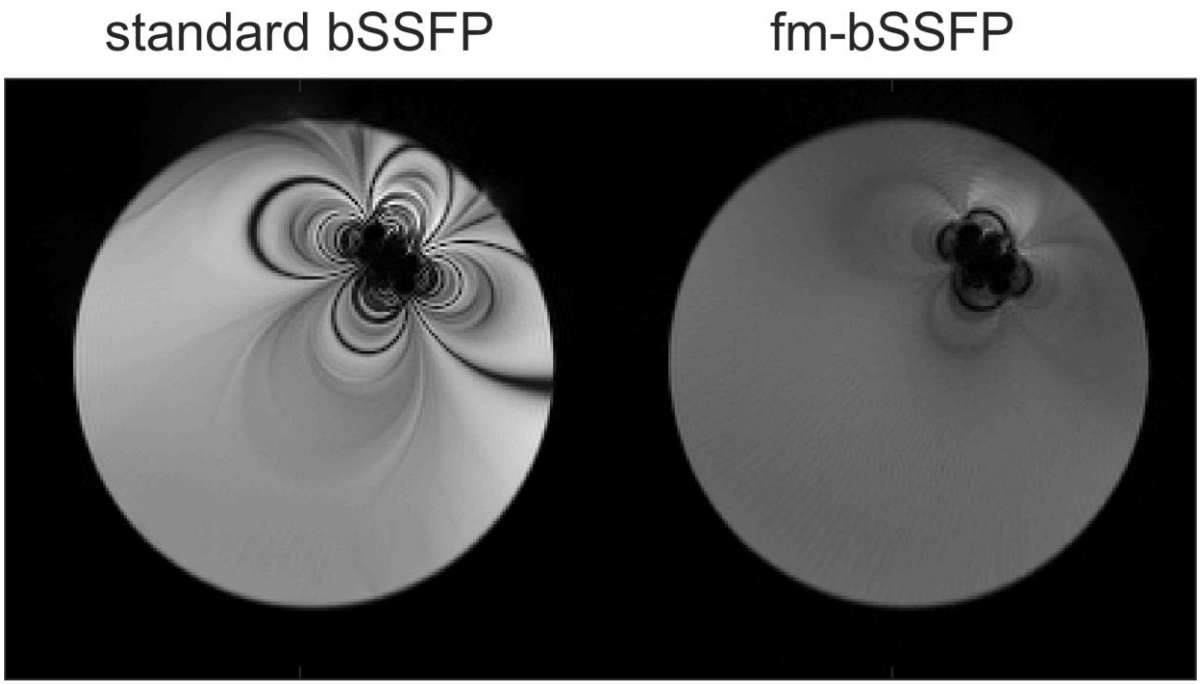

Figure 21: Phantom containing a metal implant. Banding artifacts are present in standard (left) and subdued in fm-bSSFP (right). The residual banding seen in fm-bSSFP are caused by intravoxel dephasing as the metal object distortes the magnetic field severely. A difference in overall signal intensity is apparent between the two acquisitions.

4.3.2 Real-time CINE

Reconstruction of continuously acquired, golden angle spaced, spokes can be performed using a sliding window. Resulting images provide a temporal series of the underlying anatomy, i.e. the beating heart. Standard bSSFP, as expected, provides images with a good depiction of the heart and excellent contrast between blood and myocardium (Figure 22 left). But images also suffer from banding artifacts, which follow the dynamics of the heart as the local field varies with motion. Examination of their position at different time points and different heartphases shows that they stay in the same anatomical region during the cardiac cycle.

The same acquisition over several heartbeats was performed with fm-bSSFP (Figure 22 right). As the frequency varies slowly over the whole acquisition the data considered for each image covers only a narrow frequency band. Banding artifacts establish in pixels where the local resonance frequency is at a set difference away from the reconstructed frequency band. However, as the mean frequency moves from one image to the next, the banding artifacts move in the field of view as well. The resulting time series provides a dynamic anatomical impression as well as different artifact positions.

Streaks are apparent in both implementations, due to voids in k-space where no information is collected. They are more frequent in fm-bSSFP as additional regions in k-space are subdued due to offresonance. During systole, the ventricles appear extremely bright as a result of the inflow effect. Streaking, radiating from these areas, appear uncommonly bright as well. At the bottom of Figure 22, a maximum intensity projection over the time series is shown for systole and diastole for each acquisition strategy. In standard bSSFP the constant position of the banding artifacts is retained by the projection. Opposed to that, the artifacts are alleviated in a projection of the fm-bSSFP images, similar to a combination of phase-cycled images.

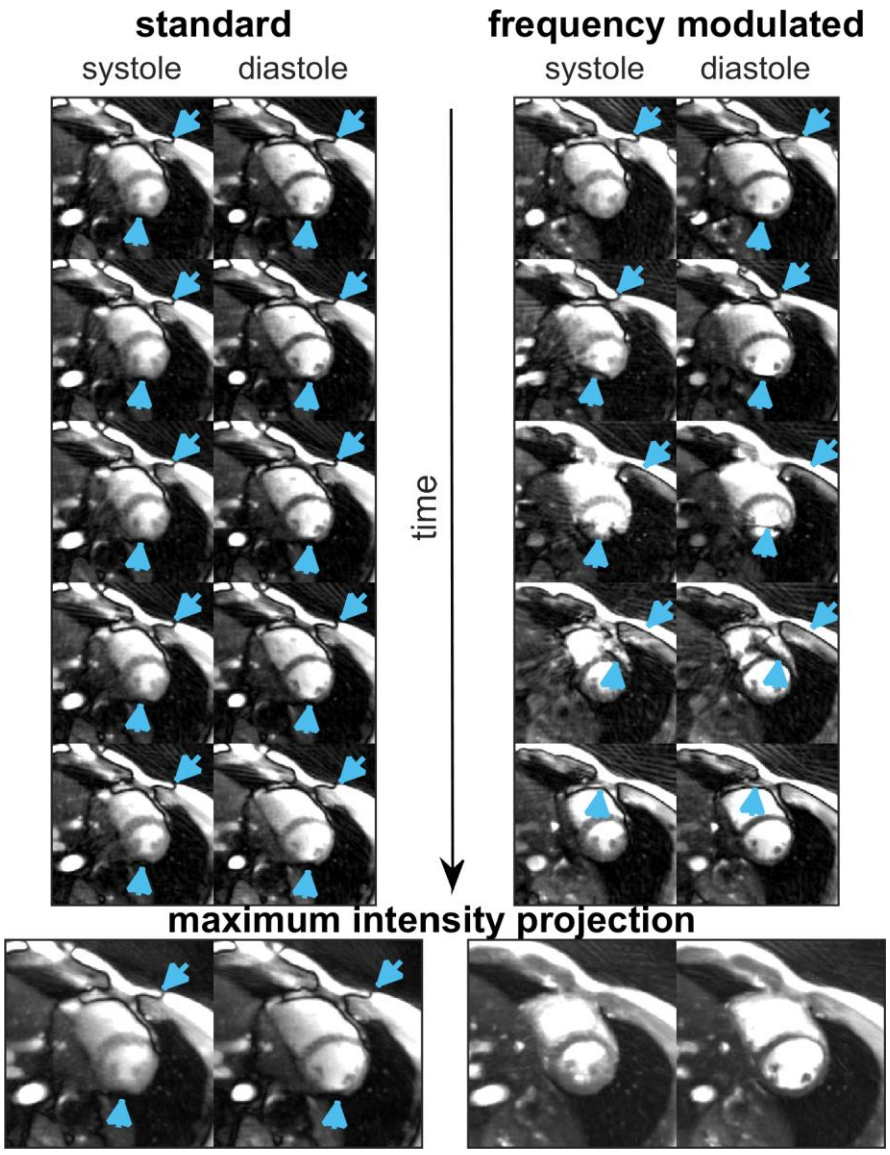

Figure 22: Real-time CINE imaging. A short axis view of the human heart is given for standard bSSFP (left) and fm-bSSFP (right). A time series was reconstructed using a sliding window reconstruction for systole and diastole, as shown in the first and second panels, respectively. All images in the time series show banding artifacts as indicated by the blue arrows. But, while artifacts appear at the same position in the heart in standard bSSFP, they shift across the image in fm-bSSFP. Thus, in fm-bSSFP, for each structure to be examined, there exists a point in time where no bandings cross that particular image section. Additionally, a maximum intensity, from images of the same heartphase in different heartbeats is shown at the bottom. MIP in standard bSSFP preserves the artifacts at their constant position. If the bandings shift, as in fm-bSSFP, the MIP combination provides banding-free images.

4.3.3 Long TR

Measurements using different TR values of the structured phantom, the water-oil phantom and of the lower leg of a healthy volunteer are shown in Figure 23 and Figure 24, respectively. As expected from theory, standard bSSFP measurements show an increasing number of banding artifacts with increasing TR. The frequency-modulated acquisition shows no banding artifacts for any of the chosen TR values.

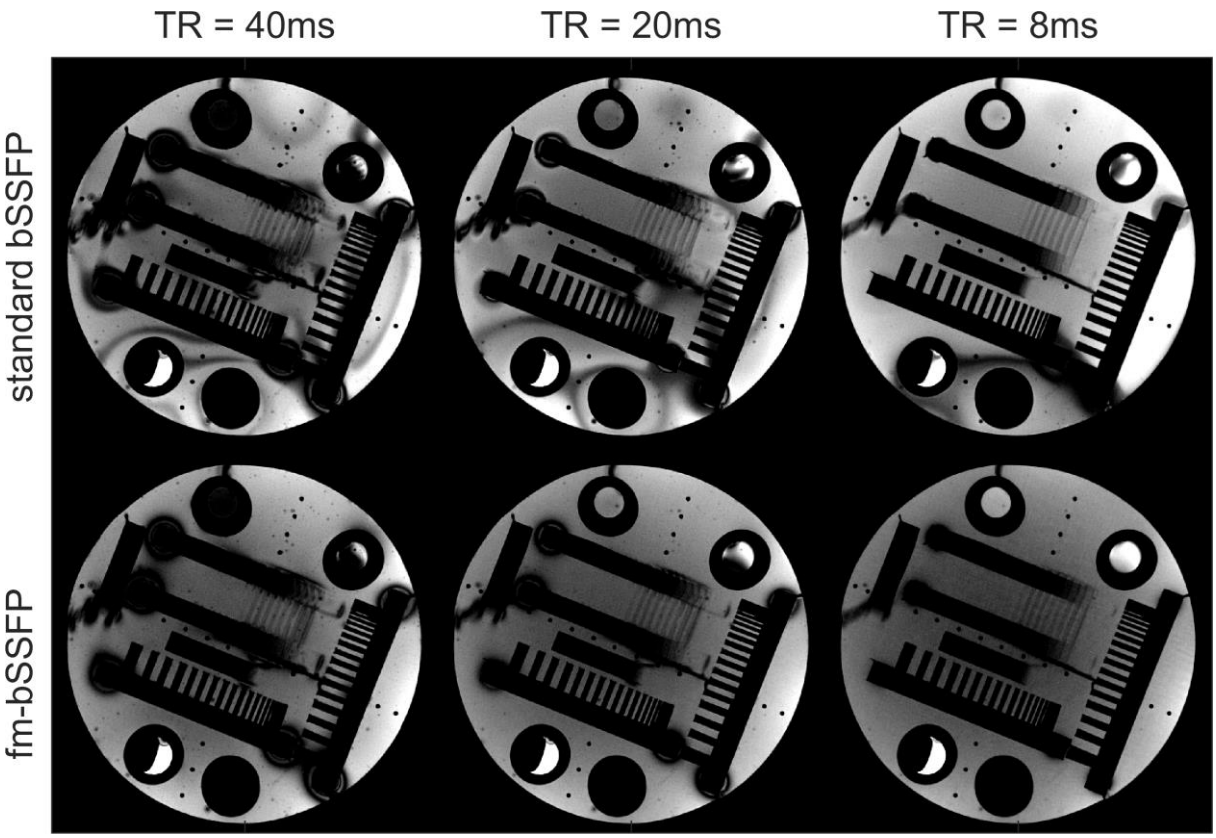

Figure 23: Phantom measurement with different TR values using the non-optimized tune-up shim. Banding artifacts are severe for long TR values in standard bSSFP and lessen with shorter values. No banding is visible in fm-bSSFP independent of the TR value.

The water-oil phantom contains two substances with different resonance frequencies, similar to the leg measurement which shows muscle and fat. Both are shown in Figure 24. Again, banding artifacts always appear for standard bSSFP. Especially in the phantom measurement a shift in the position of one banding is apparent at the interface between the substances. The artifact is shifted to the left in the oil layer in comparison to the water layer. Additionally, a change in contrast between muscle and fat can be seen in the leg with increasing TR.

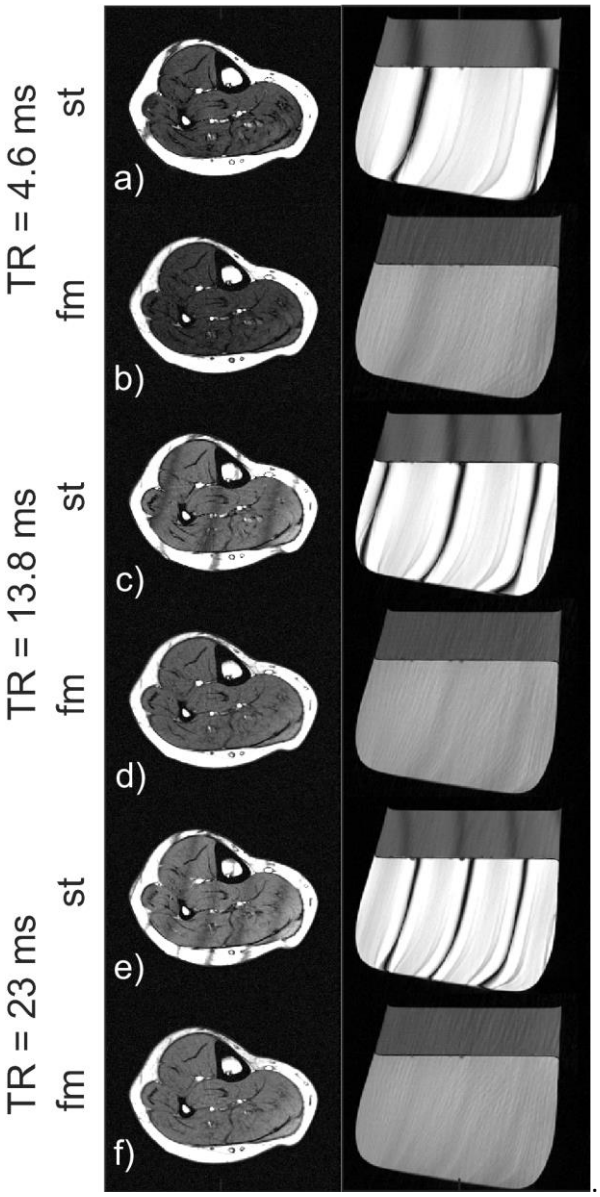

Figure 24: Lower leg and phantom measurement with variable TR values. Banding artifacts increase with higher TR in standard bSSFP. They are robustly suppressed by fm-bSSFP even for high TR values.

4.4 Discussion

Within this work a fm-bSSFP sequence was implemented and run at 1.5T and 3T MRI scanners for phantom as well as in vivo scans. The feasibility of fm-bSSFP in general is based on the fact that the steady-state is tolerant to small deviations in the pulse frequency or phase. As shown by simulations and experiments before, this is true up to a certain limit of ca. 3° dephasing per TR interval (46,96). As the overall signal behavior remains similar to standard bSSFP, especially for very slow changes, the use of fm-bSSFP for all applications of standard bSSFP seems feasible. The contrast between different tissues in bSSFP and fm-bSSFP was found to be similar by Foxall (96). Opposed to that, Benkert et

al. (46) found differences, especially in radial 2D acquisitions. These differences were most prominent in fluids and predicted a possible reduction of the high contrast between blood and myocardium typical for bSSFP. Still, 3D acquisitions of the brain and knee have shown vast similarities between the two acquisition techniques, like high contrast between brain and Cerebrospinal fluid (CSF) or cartilage and synovial fluid (59).

A comparison of images acquired in this work at different anatomical regions shows the same similarities in contrast. The 2D slices in cardiac imaging are comparable but fm-bSSFP shows slightly diminished signal intensity in the blood, thus less contrast between blood and myocardium (Figure 31 in section 5.3.1). For 3D acquisitions, distinctive features like good contrast between CSF and brain (Figure 30 in section 5.3.1) or the high signal intensity in fat (Figure 28, Figure 31 in section 5.3.1 and Figure 36 in section 6.3) are preserved.

Standard bSSFP images generally suffer from banding artifacts. Elimination of the dark bands requires advanced hardware, like high order shimming systems or fast gradient systems to realize very fast repetition times. Other options include the use of a frequency scout to shift bandings away from the region of interest or multiple acquisitions in a phase-cycled manner with a subsequent combination of these. The former cannot by itself eliminate artifacts from the whole FOV, while both procedures significantly increase scan time. The main advantage of fm-bSSFP is the inert elimination of banding artifacts due to the acquisition and combination of multiple different offresonance states in one measurement. As k-space is only filled once, only one preparation block is needed to establish the steady state and no delays occur in between measurements. Additionally, misregistration is no concern as it might be in phase-cycled acquisition.

The efficiency in eliminating bandings usually depends on the gradient of the magnetic field in the FOV. Generally, more phase-cycled acquisitions are needed for satisfactory banding removal, the steeper the gradient across the FOV. Thus, the underlying field needs to be known to estimate the number of images needed to sufficiently suppress bandings. In fm-bSSFP, a high number of different states is generally collected and combined, which ensures elimination up to the level of intravoxel dephasing. Residual banding remains in areas of very high inhomogeneity where intravoxel dephasing occurs. Nevertheless, the same is true for standard bSSFP and the phase-cycled approach. Especially in rather thick 2D slices, through-plane variations can cause unavoidable signal losses.

The main drawback of the use of fm-bSSFP with a radial trajectory is a loss in signal intensity. The frequency-modulation introduces a linear trend in the phase of each read-out line. A consequent gridding procedure combines the information from several lines into one point, thus leading to destructive interference effects. The overall image intensity is therefore lower than in standard

bSSFP. A possible remedy is provided by a specialized reconstruction method described later in this work (see chapter 5).

An additional disadvantage arises in form of artifacts, caused by the varying signal intensity during the acquisition and therefore along the k-space trajectory. As the offresonance profile includes signal drops to or close to zero, undersampling artifacts typical for the chosen trajectory can appear, like aliasing in Cartesian sampling or streaking in radial sampling. So far only a golden angle spaced radial trajectory (57) or different 3-dimensional radial trajectories have proven to provide acceptable images (97). Nevertheless, other trajectories can be realized using oversampling. This prolongs scan time to be more than that of one standard acquisition. But, as no additional preparation pulses are necessary the total time of acquiring an image, with an oversampling factor of two, will still be shorter than the total acquisition time of two phase-cycled acquisitions. The shortened acquisition time is especially advantageous in a clinical setting, as it shortens scan times per patient in general, and required breath-hold times in particular. The compatibility with recently developed trajectories, like spirals, stack of spirals, cones and many more to come, provides interesting objectives for further studies.

As the steady-state only tolerates small changes in frequency, the maximum step width in frequency (or phase) is limited. Otherwise a considerable loss in signal intensity is imminent. Therefore, to cover one period in the offresonance profile, as necessary for efficient banding removal, a minimum number of lines exists, which needs to be collected. Consequently, high resolution or 3D imaging, which necessitate to collect a high number of lines in themselves, is especially suitable for a modulated acquisition. Not least so, because long scan times make a repeated phase-cycled acquisition exceedingly inconvenient. Most in vivo application shown within this work show high-resolution 3D data, to fully exploit the advantages of fm-bSSFP.

In this chapter, two specialized applications, that show the benefits of a fm-bSSFP experiment over a standard bSSFP measurement are shown, cardiac real-time imaging and measurements using long TR values. While cardiac imaging is a standard clinical application of bSSFP imaging, long TR values are commonly avoided and only become feasible by using the frequency-modulated approach.

bSSFP is especially suited for cardiac imaging as the sequence provides a sufficiently fast acquisition to catch the motion of the heart and therefore provide images of different cardiac phases. Additionally, the sequence shows a special contrast as signal intensity varies with T_1/T_2, which is useful for the distinction between blood and myocardium. Traditionally, MRI images are either T_1 or T_2 weighted or scale with proton density. As shown before, fm-bSSFP exhibits a specialized contrast comparable to standard bSSFP.

The clinical routine CINE approach for cardiac imaging combines the information from one distinct cardiac phase during several heartbeats into one image of said phase. This assumes a completely repetitive motion and will suffer from changes between two heartbeats, like incomplete breath-holds or general motion of the patient. Additionally, most acquisitions will suffer in cases of arrhythmia as k-space coverage is not ideal for all heartphases in retrospective reordering or scan time can be prolonged in prospective/triggered cases. Opposed to that, real-time imaging captures the actual situation including overall motion and possible one-time events.

The chosen approach of a sliding window reconstruction, allows for the direct reconstruction of images after a sufficient number of spokes is collected to fill k-space to an extent were streaking does not obstruct the image view. Updates can be created even faster by renewing part of the k-space data. Reconstruction of the radial GA trajectory requires a standard gridding operation and Fourier transform. While not implemented, the simple procedure allows a complete online real-time reconstruction pipeline at the scanner. Due to the nature of a golden angle acquisition, where each collected spoke complements the information in the previous ones, the framerate is freely adjustable. With a higher framerate, more information from the previous image is reused and the truly new information decreases. Maximum framerate is given by TR, in which case only one spoke per image is updated. The minimum framerate equals the real temporal resolution and includes updating the whole k-space with newly acquired information. Here, visual impression and computational power need to be weighted. Real temporal resolution can only be improved by shortening TR or lowering the number of lines necessary for one image, i.e. lower resolution, different trajectory or the acceptance of a certain degree of undersampling.

As expected from the nature of banding artifacts and also shown in this work, their position in a reconstruction of real-time data of standard bSSFP remains almost constant. The artifacts follow the movement of the heart but always obstruct the view of the same tissue region (Figure 22). In contrast, the frequency-modulated approach shifts the position continuously across the image, which means the position changes in relation to the tissue. Examining a given structure unobstructed is therefore always possible by choosing the appropriate heartbeat.

The second application of fm-bSSFP shown concerns measurements with long TR values. As the incident of banding artifacts increases with longer TR values, the common practice is to minimize TR as far as possible. Nevertheless, sufficiently short values are not always achievable. Constrains on the minimum repetition time include, for example, hardware limits, limits in the deposited energy per time (SAR-specific absorption rate) and the danger of nerve stimulation and excessive noise. Additionally, long TR values might be of interest is some applications, e.g. ultra-high resolution,

magnetic transfer or functional MRI. Here, a robust elimination of banding artifacts, besides the short TR and advanced shimming approach, is of high value. Certain applications will even only become possible using a frequency-modulated approach.

5 Muffm - Multifrequency reconstruction for frequency-modulated bSSFP

This chapter concentrates on a reconstruction algorithm for fm-bSSFP as invented for this work and published in Magnetic Resonance in Medicine (98). Parts of the results were also presented at the annual meetings of ISMRM (99,100) and ESMRMB (101). It is shown that a simple gridding reconstruction suffers from signal losses and a multifrequency reconstruction approach is suggested as a remedy. This newly invented multifrequency reconstruction for frequency-modulated bSSFP (Muffm) algorithm is explained in detail, results are analyzed, some variations are discussed and applications to inner ear, leg and cardiac imaging are shown.

5.1 Measurements

5.1.1 In silico phantom

A 256 x 256 px in silico phantom was created containing three compartments with different material properties: a) $T_1 = 3000ms$, $T_2 = 200ms$, b) $T_1 = 300ms$, $T_2 = 80ms$, c) $T_1 = 800ms$, $T_2 = 50ms$. The signal as obtained by standard or frequency-modulated bSSFP were simulated using the following parameters: TR = 4ms, TE = 2ms, flipangle $\alpha = 50°$. Within the phantom offresonance varied linearly in each compartment from left to right.

5.1.2 2-Dimensional phantom

One slice of 5mm thickness was scanned in a standard phantom at 3T (MAGNETOM Skyra, Siemens Erlangen, Germany) using the GA trajectory with 800 spokes. Further measurement parameters were: flipangle $\alpha = 70°$, TR = 5.4ms, TE = 2.7ms, bandwidth: 574Hz/Px, resolution: 0.6 x 0.6mm^2, FOV: 300 x 300mm^2. The total measurement time was 6s. All measurements were repeated as noise-only scans, i.e. without radiofrequency-excitation, to enable the pseudo-replica method for SNR estimation described above. See Appendix 6) for all measurement details. Here, for the multifrequency reconstruction, lines were pooled to form Ng = 1, 2, 3, 4, 5, 10, 20, 30, 50, 100, 500 or 800 groups to evaluate the impact of the group size on the image quality.

5.1.3 3-Dimensional phantom

The 3D measurements of the phantom were acquired at a 3T MR scanner (MAGNETOM Skyra, Siemens Erlangen, Germany) using the GA SToST trajectory, covering a FOV of 300 x 300 x 32mm^3 with a spatial resolution of 2.3 x 2.3 x 2mm^3 and 16 partitions, each comprising 214 spokes. To avoid aliasing in slice direction an oversampling of 37.5% was added in this direction. Further imaging

parameters were: flipangle $\alpha = 41°$, TE = 1.4ms, TR = 2.8ms, bandwidth: 550Hz/Px. The total scan time for each acquisition was 14s and all measurements were repeated as noise-only scans to allow determination of the SNR. For multifrequency reconstruction groups of 20 lines were formed in the second step. See Appendix 7) for all details.

5.1.4 2-Dimensional cardiac

In a 3T scanner (MAGNETOM Prisma, Siemens Erlangen, Germany) one slice of the short axis in a human heart was acquired during breath-hold using the GA CINE trajectory. Other measurement parameters are: flipangle $\alpha = 39°$, TR = 2.8ms, TE = 1.4ms and a resolution of 2.6 x 2.6mm^2, FOV: 340 x 240mm^2 in a total measurement time of 19s. See Appendix 10) for all details. All spokes were retrospectively sorted into 20 heartphases and each phase reconstructed separately.

5.1.5 3-Dimesional in vivo inner ear and leg

Datasets of the inner ear were acquired at a 3T MR scanner (MAGNETOM Skyra, Siemens Erlangen, Germany) using the GA SToST trajectory with 64 partitions, each comprising 680 projections and a field of view of: 242 x 242 x 38.4mm^3. To avoid aliasing in slice direction an oversampling of 37.5% was added. Further imaging parameters were: flipangle $\alpha = 50°$, TE = 2.6ms, TR = 5.2ms, bandwidth: 620Hz/Px, spatial resolution 0.6 x 0.6 x 0.6mm^3. The total acquisition time for each scan was 5min 9s. See Appendix 9) for all details.

Leg data sets were acquired using the same scanner and GA SToST trajectory, with 128 partitions and 208 projections each. Further imaging parameters were: flipangle $\alpha = 50°$, TE = 2.6ms, TR = 5.2ms, bandwidth: 305Hz/Px, spatial resolution = 1.1 x 1.1 x 1.1mm^3, FOV: 140 x 140 x 640mm^3. The total acquisition time was 4min 6s. See Appendix 8) for all details.

To keep reconstruction times within a feasible range, 2000 lines were pooled for the multifrequency reconstructions of these 3D volumes.

5.2 Multifrequency reconstruction

While a frequency-modulated measurement already provides banding free images, the main aim of the multifrequency reconstruction is the preservation of the initially high signal level of bSSFP. The reconstruction algorithm is based on a simple model of the phase behavior. Measuring frequency-modulated bSSFP will result in a linear phase change over all acquired lines with periodic phase jumps of π at the positions of minimum signal intensity. Standard gridding reconstruction mixes all lines regardless of their phase which leads to destructive interference and thus an overall reduced signal intensity. The range of frequencies or offresonances covered in one measurement is

determined by the number of measured phase encoding steps and the stepwidth between two RF pulses. To apply the presented reconstruction algorithm, measurement parameters need to be tuned to cover exactly one period of the offresonance profile within one measurement. An extension for measurements covering an integral multiple of one period is straightforward.

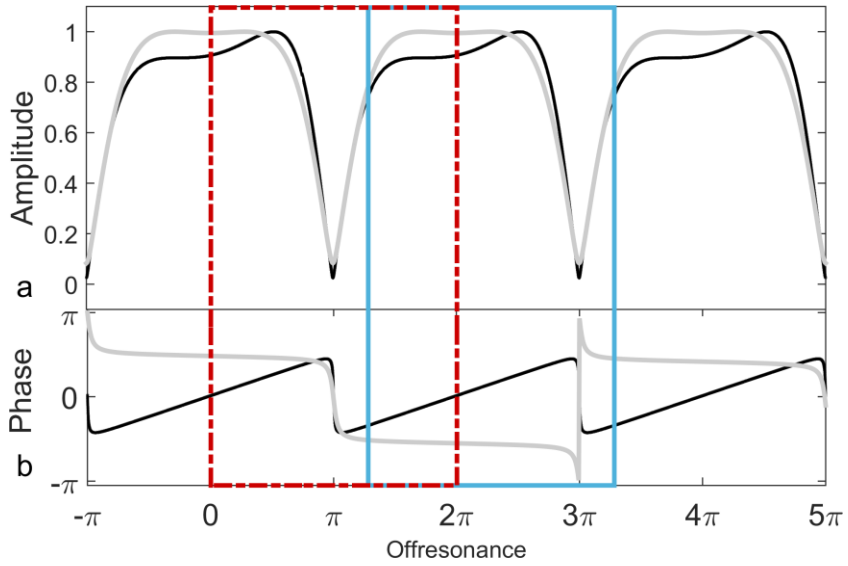

Figure 25: Shown are amplitude and phase of standard (gray) and fm-bSSFP (black). Blue and red rectangles mark exemplary areas covered by one measurement, i.e. 2π in the offresonance profile.

5.2.1 Algorithm

The multifrequency reconstruction proposed in this work consists of three steps:

Step 1: Elimination of the linear slope in the signal's phase (Figure 26 a-c)

By multiplying an appropriate linear phase term to every measured line, a binary phase distribution can be obtained. The new values $l_{n,rot}$ of the n-th measured line l_n are calculated as:

$$l_{n,rot} = l_n * \exp(-i * \frac{\pi}{N_{proj}} * n) \qquad [27]$$

where N_{proj} is the total number of measured lines. Phase values of all lines are now restricted to being either φ_0 or $\varphi_0 + \pi$. The number of lines featuring each phase value, depends on the position of the phase jump and therefore on the local offresonance.

Step 2: Binning and alignment of acquired lines (Figure 26 d-f)

Maximum signal intensity is given for constructive interference of all acquired lines, i.e. all lines having equal phase. This can be achieved by adding π to all lines of phase φ_0. Unfortunately, the

position of the jump varies with offresonance and is therefore unknown. Additionally, a joint correction for all pixels simultaneously cannot be realized as the offresonance varies spatially over the FOV. To overcome this problem different potential positions are assumed and a correction is performed accordingly. Lines are binned in agreement with the assumed position of the phase jump and π is added to one of the bins. After this, one image is reconstructed from the manipulated lines for each assumed position and therefore corresponds to a certain offresonance. The reconstructed images will be optimal for all pixels where the real offresonance equals or closely approaches the assumed case. Thus, for each pixel one of the reconstructed images provides the maximum possible signal intensity.

Step 3: Selection of pixel values (Figure 26 g)

The signal amplitude through the stack of reconstructed images shows slowly varying signal intensities depending on the number of lines with equal phase or opposite phase. For each pixel within the FOV, one value out of the image stack is chosen to create the final image. One approach is a maximum intensity projection, assuming that constructive interference will result in the highest value.

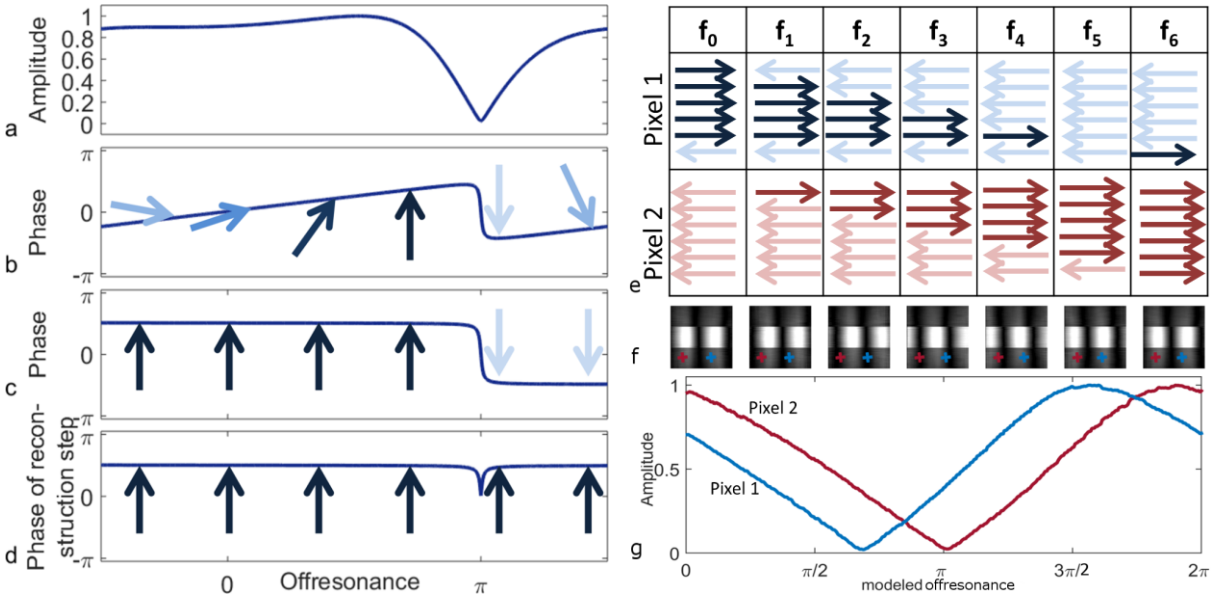

Figure 26: Steps of a Muffm reconstruction. Amplitude a) and phase b) of one measurement cover one period in the offresonance profile and include one signal Null and the accompanying phase jump. First step is the correction of the linear trend in phase, leading to a binary phase distribution with a difference of π c). An additional phase of π is added to one bin, leading to uniform phase across all lines d). The position of phase jump and with it the separation between the bins varies with offresonance and therefore between two pixels e). By successively adding π to an increasing number of lines the perfect case can be found, e.g. f_5 in pixel 1 and f_0 in pixel 2. From each case one image is reconstruction featuring different positions of the banding artifacts f). By performing a maximum intensity projection over the whole stack of images, the highest signal intensity for each pixel can be found g) .

Within the reconstruction different parameters influence the outcome. The number of assumed off resonance positions in step 2 determines the number of reconstructed images and thus influences reconstruction time as well as the number of images from which the final result is constructed. The ideal case reconstructs as many images as spokes are acquired. As this leads to high computational demand the difference between the ideal case and a grouping of several lines is evaluated.

Step 3 can be modified by choosing alternative ways of determining the perfect signal in each pixel. Originally implemented using MPI, other approaches are possible. Through the stack of reconstructed images, it can be assumed that each correctly binned line increases the resulting signal, while each wrongly assigned line decreases it. This leads to a flattened triangular shape of the signal in one pixel as seen in Figure 26 g. The slowly varying component can be extracted from the first coefficient of a Fourier series transformation. As each image represents a different offresonance the stack of images can also be treated and combined using the algorithms already described for phase-cycled images in section 2.3 (e.g. complex sum, magnitude sum or sum of squares combination).

Another valuable information, next to the highest signal in the reconstructed stack of images, is the position of constructive interference. For each reconstructed image the position of the phase jump was assumed differently. If the image has the highest possible signal amplitude the assumed position is closest to reality. Thus, the index of the maximum intensity pixel within the image stack provides a mean to deduce the offresonance and provide a qualitative field map.

5.2.2 SNR comparison

The expected gain in SNR through multifrequency reconstruction is based on the corrected phase behavior. Initially the acquired signal phase in a frequency-modulated measurement changes smoothly by one π over one period in the offresonance profile. As all lines cross the centre of k-space a gridding reconstruction will integrate the signal of each line in that point and to some extent in all points close to the center as well. Step 1 of the reconstruction eliminates the linear trend and step two aligns the phase of all lines. Therefore an estimate of the gain in signal can be given by the integration over the respective phase profiles:

fm: $\int_0^{\pi} sin\phi \, d\phi = 2$

Muffm: $\int_0^{\pi} 1 \, d\phi = \pi$

From this estimate, the gain in signal between standard gridding and multifrequency reconstruction is of a factor of $\pi/2 \sim 1.5$. This value provides an upper bound of the gain in SNR as changes in noise behavior are not accounted for.

5.3 Results

5.3.1 Multifrequency reconstruction

Standard bSSFP images show the typical banding artifacts due to field inhomogeneities. No bandings are visible in frequency-modulated acquisitions but images from standard reconstruction show an overall lower signal intensity. Multifrequency reconstruction for frequency-modulated acquisition restores the initial high signal intensity and provides bright banding free images.

An in silico phantom was established to investigate artifacts, signal levels and SNR for standard bSSFP, common combination algorithms for phase-cycled bSSFP and frequency-modulated bSSFP (Figure 27). The magnitude of standard bSSFP varies spatially with the offresonance, showing the typical profile with dark bandings interspaced by high intensity plateaus. The position of the banding artifacts can be shifted by applying different phase-cycles (e.g. $\Delta\theta = 0°$ and $\Delta\theta = 180°$). SNR varies spatially in accordance with the signal intensity. The complex sum or p-norm combination of the two phase-cycled standard bSSFP measurements, lessen the severity of banding artifacts but small signal variations at double the spatial frequency are still apparent, less so in p-norm combination than in complex sum combination. The total SNR of Muffm is comparable to that of the combination techniques, like sum of squares combination of multiple phase-cycled images. Only one of the tested specialized combination approaches, the p-norm combination provided better SNR values in some regions. The simple gridding reconstruction results in a considerably lower SNR than multifrequency reconstruction or standard bSSFP in onresonant areas. The SNR of multifrequency reconstruction is slightly lower than peak values in standard bSSFP and combination procedures, but it is smooth over the whole field of view.

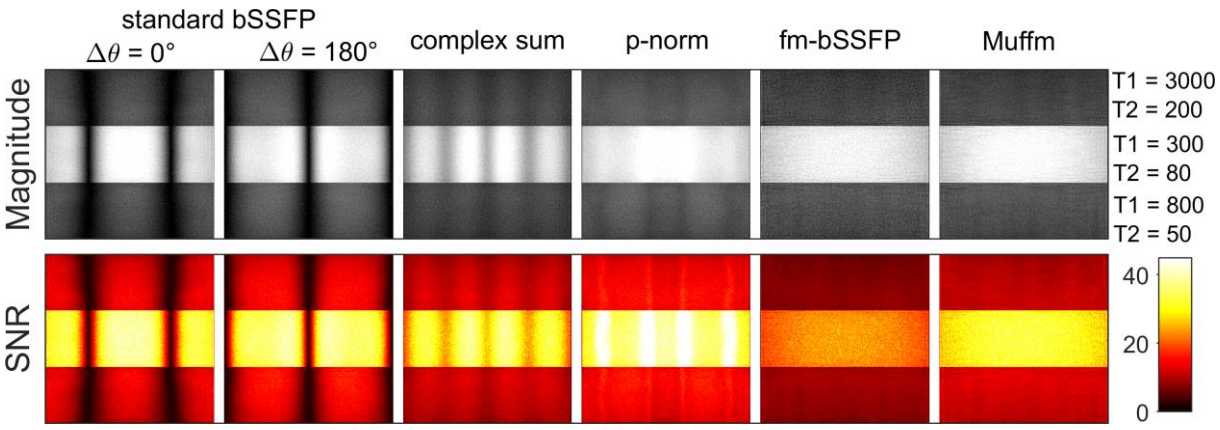

Figure 27: Comparison of magnitude and SNR in an in silico phantom. From left to right: Two phase-cycled standard bSSFP acquisitions show pronounced banding artifacts but high SNR in onresonant areas and around. In the complex sum and p-norm combination thereof, banding is alleviated and only residual rippling is visible. SNR varies across the image. P-norm combination shows high overall SNR values. Standard gridding reconstruction for fm-bSSFP and Muffm provide banding free images. The SNR gain through the specialized reconstruction is clearly discernible.

Insights from the in silico phantom were tested for in vivo imaging of the human knee. Figure 28 shows magnitude and SNR of a transversal slice from a 3D volume, again for standard bSSFP, two common combination algorithms for phase-cycled bSSFP and frequency-modulated bSSFP with two different reconstruction procedures. Conclusions from in silico testing recurred. Bandings can be seen in standard bSSFP and are partially repressed by retrospective combination of two phase-cycled measurements. Frequency-modulated measurements successfully eliminated these artifacts and multifrequency reconstruction provides higher SNR than gridding.

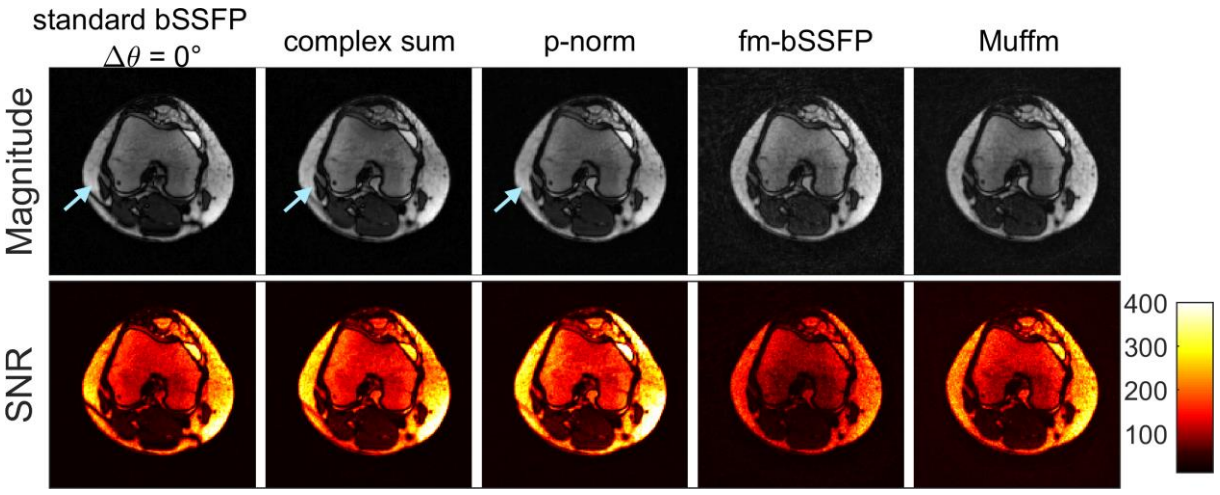

Figure 28: Comparison of magnitude and SNR in an in vivo knee measurement. From left to right: A phase-cycled standard bSSFP acquisition with banding artifact (arrow). SNR is high in onresonant areas and around. In complex sum and p-norm combination of two phase-cycled images, the banding is still visible but less pronounced, with the p-norm combination featuring superior SNR. Both standard gridding reconstruction for fm-bSSFP and Muffm eliminate visible banding, nevertheless the gridding reconstruction suffers from considerable SNR loss.

To quantify the SNR gain by multifrequency reconstruction, 3D (Figure 29 a, b) and 2D (Figure 29 d, e) measurements of a phantom were acquired using standard bSSFP and fm-bSSFP, and the latter postprocessed using standard gridding reconstruction or Muffm. Magnitude images show bandings for standard bSSFP but no artifacts in frequency-modulated bSSFP for both cases. Mean SNR is higher for Muffm by a factor of 1.49 ± 0.7 in 3D and 1.23 ± 0.11 in 2D (Figure 29 c, f).

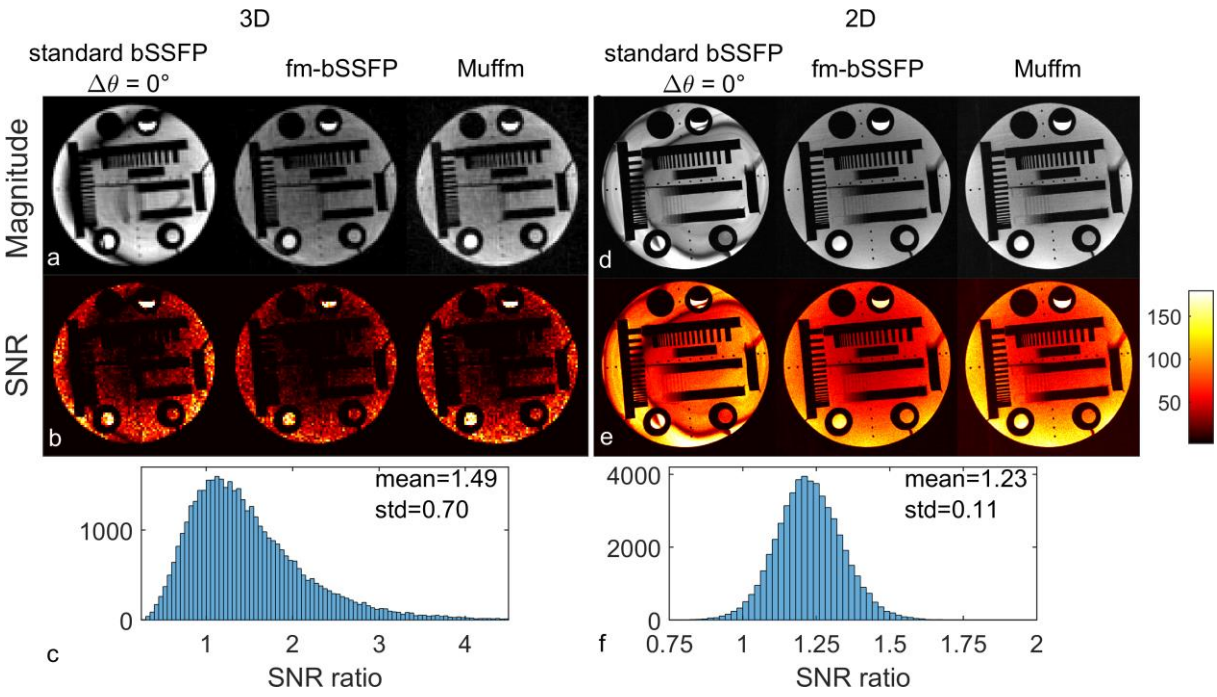

Figure 29: Magnitude and SNR of a phantom measurement. Standard bSSFP suffers from banding artifacts and varying SNR, accordingly. Signal gain is obvious when using Muffm in comparison to the standard gridding reconstruction for fm-bSSFP. The mean SNR ratio of gridding and Muffm can be quantified to be 1.49 for the 3D measurement and 1.23 for 2D, approaching the theoretical maximum gain of $\pi/2$.

As further examples for in vivo applications, 3D images of the inner ear and lower leg and a 2D slice of the human heart were acquired. Figure 30 compares magnitude images of one transversal slice of the inner ear (a-c) and MIP of several transversal slices containing the whole inner ear structure (d-f). Also shown in Figure 30, is a cross section of the lower leg (g-i). A short axis slice of the heart is shown in Figure 31. Banding artifacts from standard bSSFP disrupt important structures like the semicircular ducts (Figure 30 a, d), the subcutaneous fat layer (Figure 30 g) or the myocardium (Figure 31 left). Frequency-modulated acquisition is capable of removing these artifacts allowing an undisturbed depiction of the anatomy. Multifrequency reconstruction preserves this ability while providing a higher signal level, improving overall image quality and therefore allows an easier distinction between tissues or tissue and background, like lung and myocardium or structures in the sinuses and ear canal.

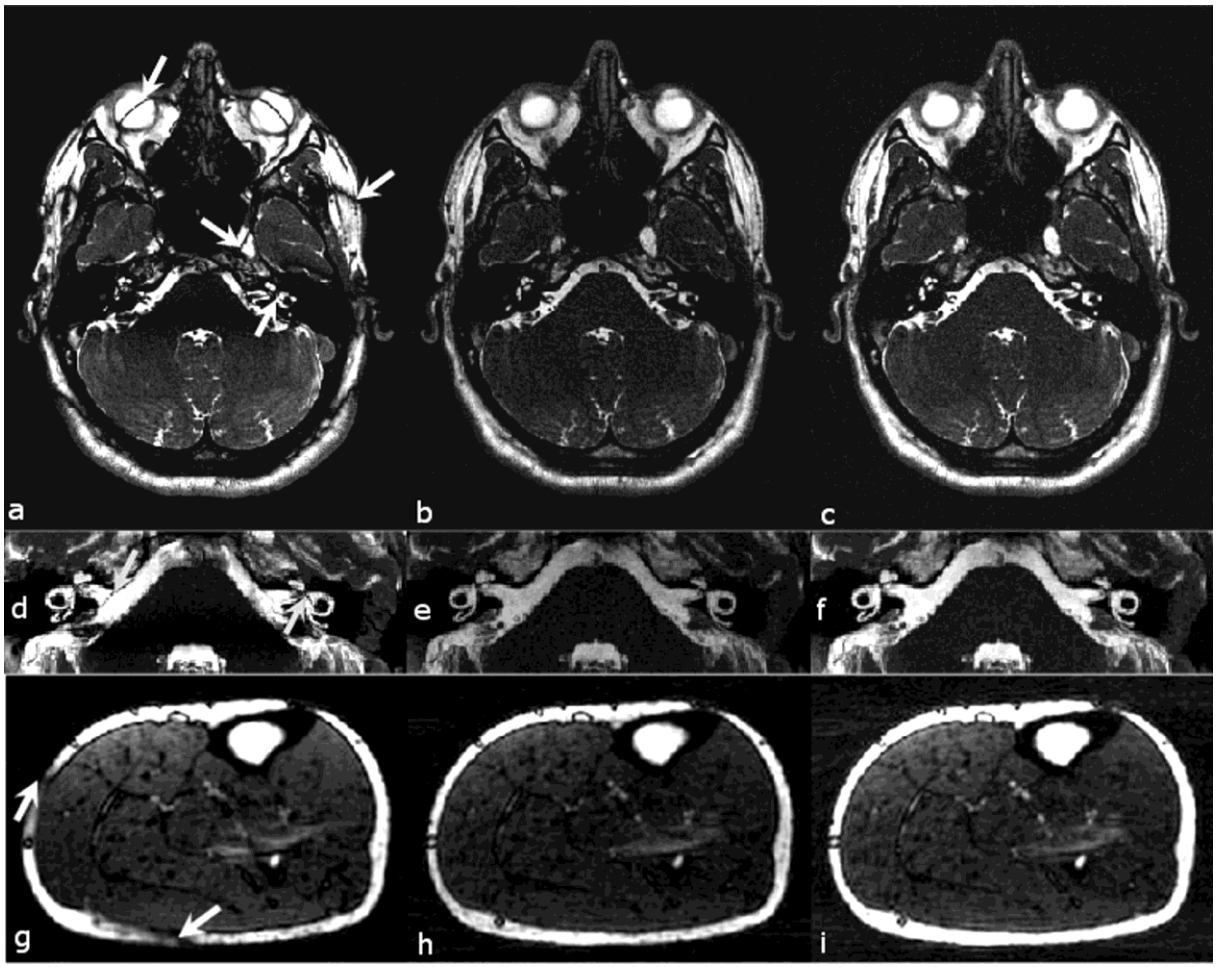

Figure 30: In vivo 3D acquisitions: transversal slice of the head showing the inner ear (a-c), maximum intensity projection of selected slices in the region of the inner ear (d-f) and a cross section of the lower leg (g-i). In the standard bSSFP acquisitions banding artifacts are visible (a, d, g arrows), which impair structures of interest, like the semicircular ducts. Images acquired by fm-bSSFP show no banding but the simple gridding reconstruction suffers from signal loss (b, e, h). Finer structures like the muscle texture in the leg do not appear as pronounced. Muffm provides banding-free images with high signal intensity (c, f, i).

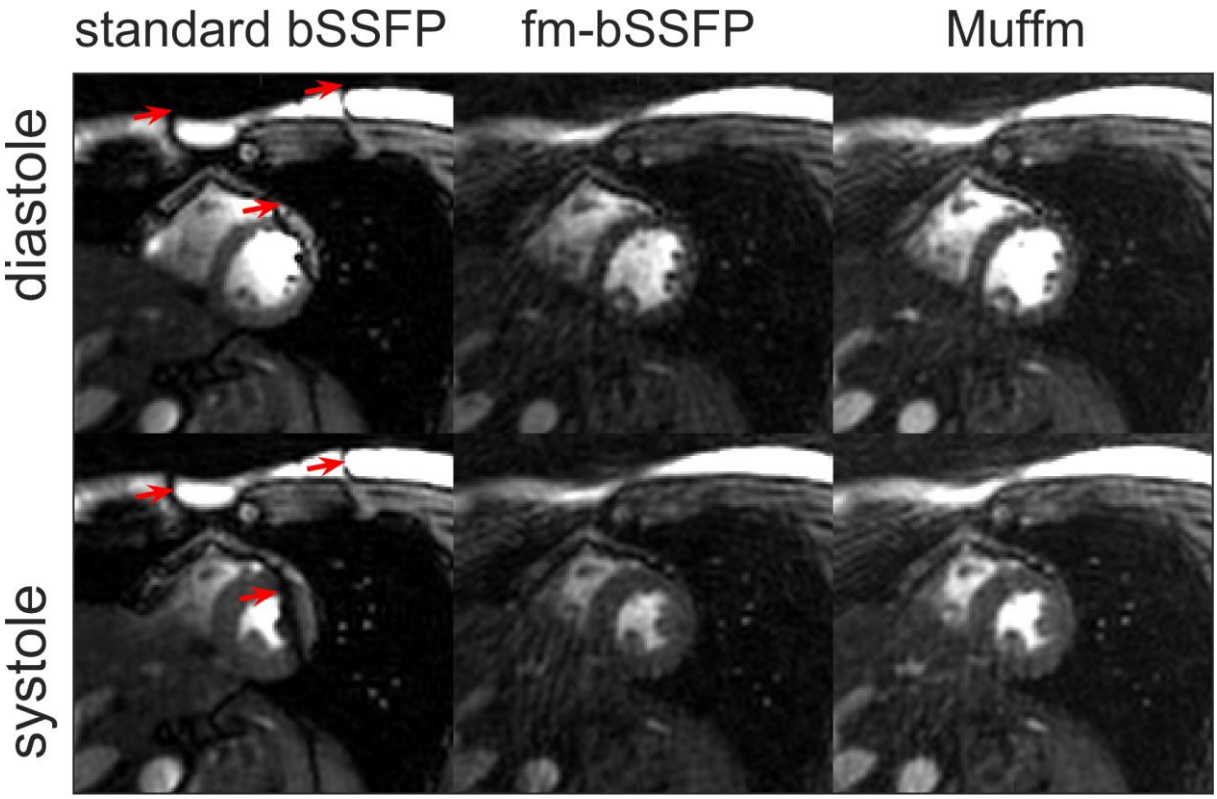

Figure 31: Short axis view of the human heart. Top: systole. Bottom: diastole. A pronounced banding artifact in standard bSSFP impairs the view of the myocardium and hinders the evaluation of the wall movement. No banding artifacts but the low signal intensity can aggravate diagnostics in the gridding reconstruction of fm-bSSFP. Muffm images have no visible banding artifacts and high signal intensity. Fm-bSSFP acquisitions alleviate banding artifacts, but on the other hand, it is more susceptible to streaking, as the signal intensity varies between spokes.

5.3.2 Different group sizes

The results of Muffm with different group sizes are shown for a 2D slice of a phantom measurement in Figure 32. Additionally,the difference between the ideal case, here meaning maximum number of groups possible, and different group sizes is shown.

A high number of lines pooled in one group results in a low number of individual reconstructed images. In all reconstructions using a small number of groups (Ng) with different assumed offresonances, banding was not sufficiently removed. In general, the impact of banding artifacts decreases with increasing Ng. For $Ng \leq 10$ this effect is clearly visible. No more bandings are discernible at $Ng = 20$ and no significant differences are visible anymore. The total difference is below 1%. For $Ng > 20$ no further improvement with increasing group number is visible and the difference is neglectable.

a)

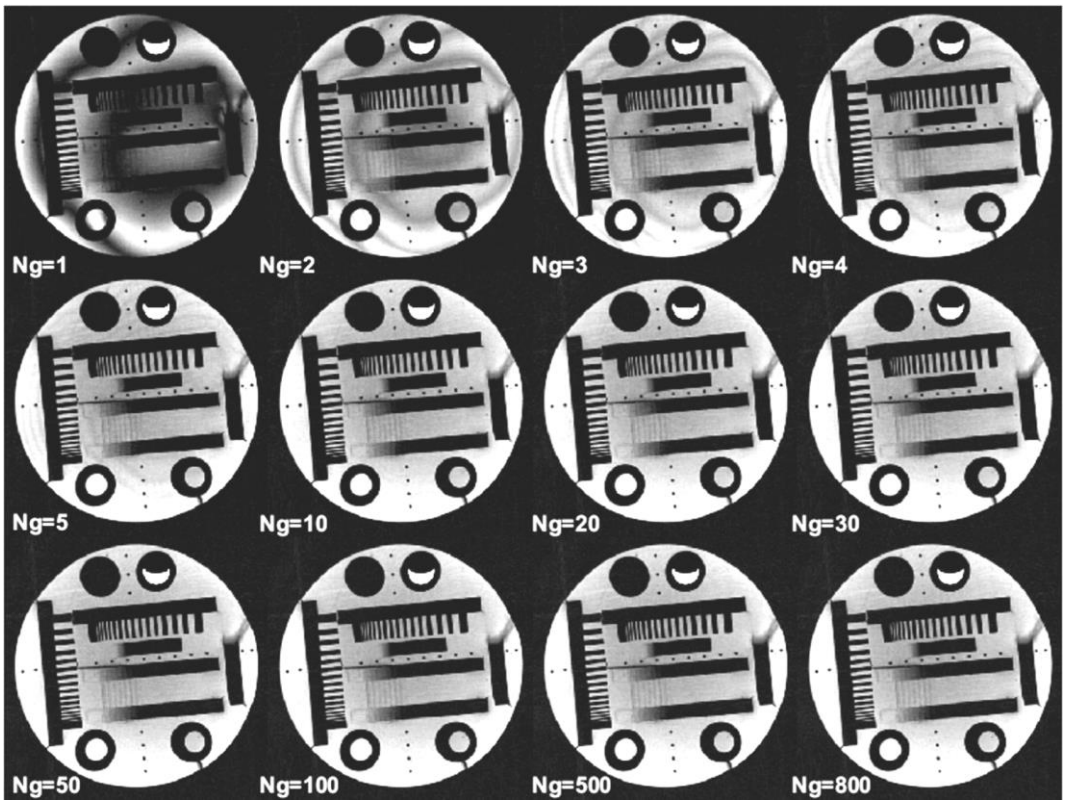

b)

Figure 32: Muffm for a 2D phantom measurement. a) Reconstructions were performed with different group sizes and according number of groups reaching from Ng = 1 to Ng = 800. The severity of banding artifacts decreases with increasing number of groups. For Ng = 10 artifacts are not visible anymore and image quality does not change visibly with further increase of Ng. b) Difference images between the ideal reconstruction with Ng = 800 and the image reconstructed from less groups. For Ng = 10 or higher the overall difference is below 1%.

5.3.3 Fieldmap estimation

The MIP cannot only determine the highest magnitude for each pixel but can also determine the image number of its origin. As each reconstructed image corresponds to one assumed position of the phase jump, this image number can again be translated to give the best fitting assumption and therefore underlying real offresonance. Plotting the image number as shown in Figure 33 provides an estimate of the fieldmap, featuring slowly varying regions within one tissue. Sudden jumps at tissue boundaries are caused by the chemical shift and the resulting change in offresonance.

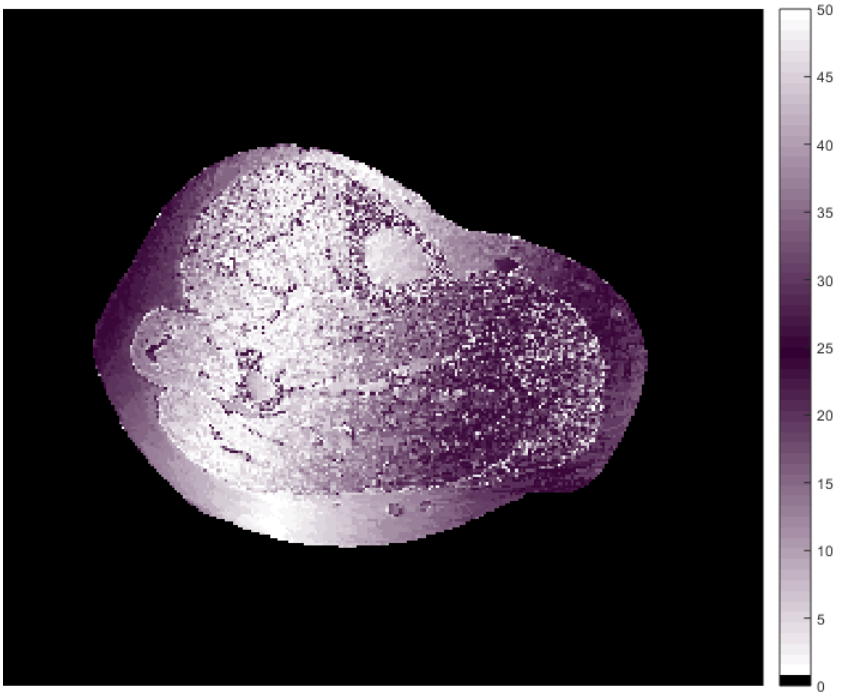

Figure 33: Cross section of the lower leg. Shown are the positions of the maximum signal intensity in the stack of images produced by Muffm. The position corresponds with the jump in phase and therefor with the local offresonance. Plotting the position can provide a quantitative estimate of the fieldmap.

5.3.4 Modifications to MIP

Figure 34 shows one cardiac phase of the CINE images in Figure 31. Different methods were used in the third step of the multifrequency reconstruction for combining the stack of 63 images. Shown are a maximum intensity, complex sum, magnitude sum and a sum of squares combination as commonly used in phase-cycled imaging as well as the slowly varying signal component as determined by a FFT. Streaking artifacts are apparent in all images, especially in the dark background and radiating from very bright fat or blood areas. The complex sum combination shows significant signal dropouts especially in the subcutaneous fat, which are not visible in the other methods. The

image resulting from the FFT main component appears noisy. The magnitude sum combination shows an elevated background which causes it to appear brighter and less contrasty. Maximum intensity projection, as well as sum-of-squares, show the least streaking, no signal variations and good contrast between different tissues.

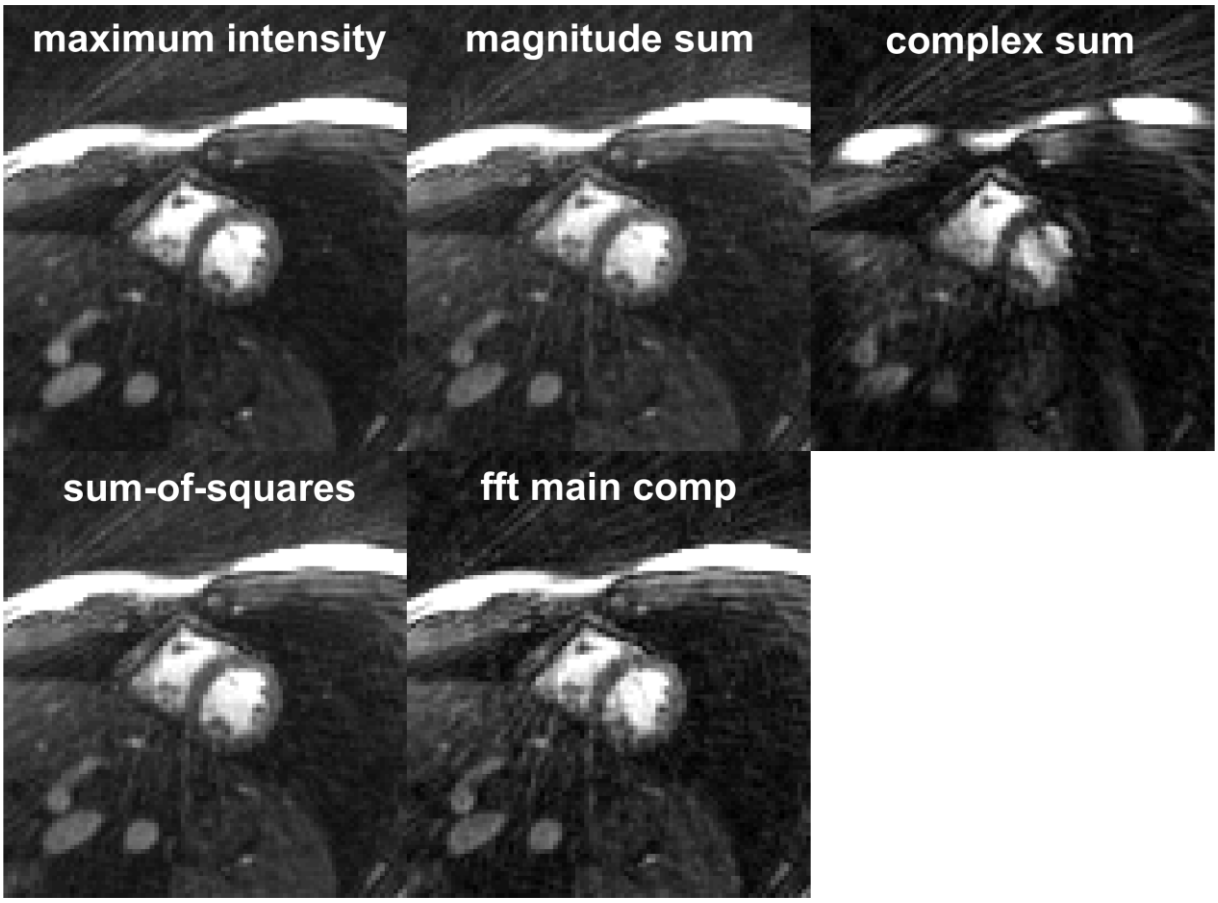

Figure 34: Alternatives to the MIP in Muffm include complex-sum, magnitude sum and sum-of-squares combination, as well as extraction of the main component from a Fourier transform and fitting of the triangular signal behavior.

5.4 Discussion

The multifrequency reconstruction improves the SNR, and therefore image quality, in frequency-modulated bSSFP images. While the frequency modulation in itself, is capable of removing banding artifacts from the images, a standard reconstruction of such data suffers from signal loss. The specialized reconstruction, based on a simple model of the phase behavior, can compensate such losses and consequently improves image quality. The increase in SNR for the given phantom measurement totals to 23% in 2D and 49% in 3D. The practical gain is close to the theoretically established maximum gain of a factor of $\pi/2$. The achievable SNR is comparable to state-of-the-art combination techniques for phase-cycled bSSFP. Nevertheless, all combination methods are based on

the acquisition of multiple phase-cycled images, which means a considerable extension of scan time. The single acquisition with comparable performance is the most valuable characteristic of Muffm.

Out of the various methods proposed for the combination of phase-cycled bSSFP acquisition, generally, all achieve better results, the more different images are combined. As Muffm provides a stack of images featuring a high number of different offresonances, the application of the known algorithms to these images is straightforward. The maximum intensity projection can find the best possible signal in cases of low noise and without artifacts. Unfortunately, it favors the bright streaking especially in areas of low background signal. Still, it provides the best result in the given example. Although complex sum provides good results in phase-cycled imaging, this is not the case here. While a shift in the measuring sequence causes an overall change in the phase, this is not the case for multifrequency reconstruction. Consequently, only two opposing phase values are present in the image stack. Depending on their proportions, signal cancellation will be more or less severe and results in new artefacts. Summing of squares or a magnitude operation eliminate this phase problem and provides reasonable and smooth results. The approach to use the first component of a FT was chosen, as real signal is expected to vary between maximum and minimum signal when covering one period in offresonance, while streaking and artifacts show more rapid variations. Although streaking is successfully lowered, the use of only one signal component leads to a very noisy appearance in the overall image. The prior knowledge about the signal variation within the stack of images, derived from the fact that each image differs from the former by turning one line in k-space, suggests a model-fitting for reconstruction. More sophisticated methods or more accurate models of the signal need to be evaluated in future work. Within this work, maximum intensity projection provides the best image in comparison to the other methods tested. As the last step, after the creation of the stack of images with different offresonances, is variable, the proposed algorithm can be modified and benefit from newly developed combination algorithms for phase-cycled bSSFP.

As the reconstruction relies on a fm-bSSFP acquisition covering at least one period of the offresonance profile, certain requirements on the measurement arise. The limited size of the quadratic increment in the phase-modulation necessitates a minimum number of acquired read-out lines. Therefore, the reconstruction is most suitable in cases where a fm-bSSFP acquisition is beneficial, like 3D or high-resolution cases. Also, residual banding in fm-bSSFP, due to intravoxel dephasing, cannot be resolved by the specialized reconstruction.

A limitation of the reconstruction algorithm itself, is given by the computationally intense reconstruction of multiple images. For each assumed position in offresonance, one reconstruction needs to be performed. Grouping of lines provides a remedy for overlong reconstruction times. In

general, the more different offresonance positions are modeled the better the resulting image quality. Nevertheless, it is shown here that an improvement is only visible up to the reconstruction of ten different images but not obvious for higher numbers. Similar results have been presented in the context of combination algorithms for phase-cycled acquisitions (51). Independent of the total number, each position of phase jump can be modeled and reconstructed independently, which allows for parallelization and major cutbacks in reconstruction time on modern hardware.

All in all, this chapter demonstrated the capabilities of Muffm in various cases. While the frequency-modulated approach allows imaging with suppressed banding artifacts, the specialized reconstruction algorithm successfully regained signal losses. Images show improved SNR after Muffm. Additionally, the reconstruction algorithm successfully retains the main advantages of a bSSFP measurement like acquisition speed and image contrast.

6 Phase sensitive water fat separation for frequency-modulated bSSFP

This chapter comprises an application of fm-bSSFP to water-fat separation. The procedure is based on the phase-sensitive approach first proposed by Hargreaves et al. (85) and subsequently modified and applied in different studies (84,87,87,102–104). Nevertheless, so far no combination of a frequency-modulated acquisition and a phase-sensitive separation approach has been shown. The combination of these two methods was shown for the first time as part of this work and is registered for patent. Parts of the results were also presented at the annual meeting of the ESMRMB (105).

6.1 Measurements

6.1.1 2D and 3D acquisitions at 1.5T

The lower legs of a healthy volunteer were scanned in a 1.5T MR system (MAGNETOM Aera, Siemens Erlangen, Germany). One frequency-modulated bSSFP and two phase-cycled standard bSSFP acquisitions were performed. All datasets were acquired using a golden angle stack-of-stars trajectory with 128 slices per slab and 526 projections each. Further parameters were: TR = 4.6ms, TE = 2.3ms, flipangle $\alpha = 30°$, bandwidth = 434Hz/Px, spatial resolution = 1 x 1 x 1mm^3, FOV = 320 x 320 x 128mm^3. The total acquisition time was 5min 55s for frequency-modulated bSSFP and each of the two phase-cycled acquisitions. See Appendix 11) for all details.

A single axial slice of the lower leg of a healthy volunteer, as well as a water-oil phantom, were scanned in the same MR system. Here, one frequency-modulated bSSFP measurement and one standard bSSFP acquisitions were performed for TR values of 4.6ms, 13.8ms and 23ms. Datasets were acquired using a 2D golden angle radial trajectory with 1000 spokes (TE= TR/2, flipangle $\alpha = 70°$, bandwidth = 674Hz/Px, spatial resolution = 0.7 x 0.7mm^2, FOV = 340 x 340mm^2). Total acquisition times were 7s, 21s and 35s for the different TR values. See Appendix 14) for leg measurement and 15) for phantom measurement details.

6.1.2 3D Acquisition at 3T

The upper legs of a healthy volunteer were scanned in a 3T MR system (MAGNETOM Skyra, Siemens Erlangen, Germany) using fm-bSSFP and standard bSSFP. A non-selective pulse was employed to realize TR = 2.3ms. The data was collected along a golden angle stack-of-stars trajectory with 112 slices per slab and 360 projections each (TE = TR/2, flipangle $\alpha = 42°$, bandwidth = 1502Hz/Px, spatial resolution = 1.8 x 1.8 x 1.8mm^3, FOV = 380 x 380 x 202mm^3). Total acquisition times were 1min 42s each. See Appendix 12) 13) for all details.

The lower leg of a healthy volunteer was scanned in the same scanner. Here, one frequency-modulated bSSFP measurement and one standard bSSFP acquisitions were performed at TR = 7.2ms using a slab-selective RF-pulse. All datasets were acquired using a golden angle stack-of-stars trajectory with 96 slices per slab and 592 projections each (TE = TR/2, flipangle $\alpha = 30°$, bandwidth = 220Hz/Px, spatial resolution = 1.1 x 1.1 x 1.1mm^3, FOV = 350 x 350 x 105mm^3). Total acquisition times were 8min 36s each. See Appendix 13)12) for all details.

6.2 Separation method

6.2.1 Water and fat masks

For water fat separation all acquisitions were reconstructed using standard gridding reconstruction. To obtain the coil sensitivities a low resolution image was reconstructed using the adaptive reconstruction algorithm described by Walsh et al. (106).

Additionally, a complex sum was formed from the images obtained from the two phase-cycled measurements (87). Block regional phase correction was performed on all images using block sizes of 4 x 4 x 4px. 2D images were replicated along the 3rd dimension in order to allow using the same implementation of the region growing algorithm, the effective block size therefor being 4 x 4 x 1. The correction was performed on each coil individually using the voxel with highest magnitude as a start point.

Images containing two disconnected structures (e.g. lower legs) were separated into two images along the background inbetween the two. The correction was performed on both images individually to avoid general swaps between the two tissues while the region growing algorithm moves through noise-only areas. After correction the two images were combined again in the former setup.

The tissue giving the main signal in the start voxel will automatically be assigned a phase of 0 while the other tissue is assigned the phase of π. As the start point is set individually the assignment might vary between different coils or image parts (lower leg cases as described before). As fat generally produces a higher magnitude than water, the assignment was checked by comparing the average magnitude in each group. If necessary, a phase of π was added to the whole image to correct unmatched coils.

After correction all coils belonging to one measurement were combined to one image S_{cmb} in a linear fashion (103):

$$S_{cmb}(r) = \frac{\sum_{i=1}^{N} S_i(r) * |C_i(r)|}{\sum_{i=1}^{N} |C_i(r)|}, \quad [28]$$

where S_i is the phase corrected single coil image and Ci are the coil sensitivities and N is the number of coils.

A mask including all voxels containing mostly signal from fat was then created from the combined image by selecting all voxels with: $real(r_{xyz}) > 0$. All voxels containing mostly water were detected as all voxels with $real(r_{xyz}) < 0$. Water and fat masks were stored as binary arrays.

6.2.2 Water-only and fat-only images

Magnitude images from all measurements, as well as the complex sum combination image, where obtained from single coil images by using the adaptive reconstruction algorithm described by Walsh et al. (106). While, a simple linear combination of the phase corrected images is useful to combine the binary phase information but results in signal losses where the tissue assignment disagrees between coils and is therefore not suitable for determining magnitude images.

Additionally, Muffm was performed for the frequency-modulated acquisitions to revoke signal loss arising from the acquisition mode.

After that, water-only or fat-only images can easily be obtained by a pixel-wise multiplication of the stored water or fat mask with the magnitude images.

6.3 Results

If the strength of the magnetic field varies spatially, the signal intensity and phase varies over the field of view. In case of a frequency-modulated measurement no variations can be seen in magnitude but the phase showcases a linear change. Figure 35 shows a sagittal view of the lower leg before (a) and after (b) block regional phase correction and (c) a binary mask, distinguishing voxels with $real(r_{xyz}) < 0$ and $real(r_{xyz}) > 0$, which correspond to water and fat.

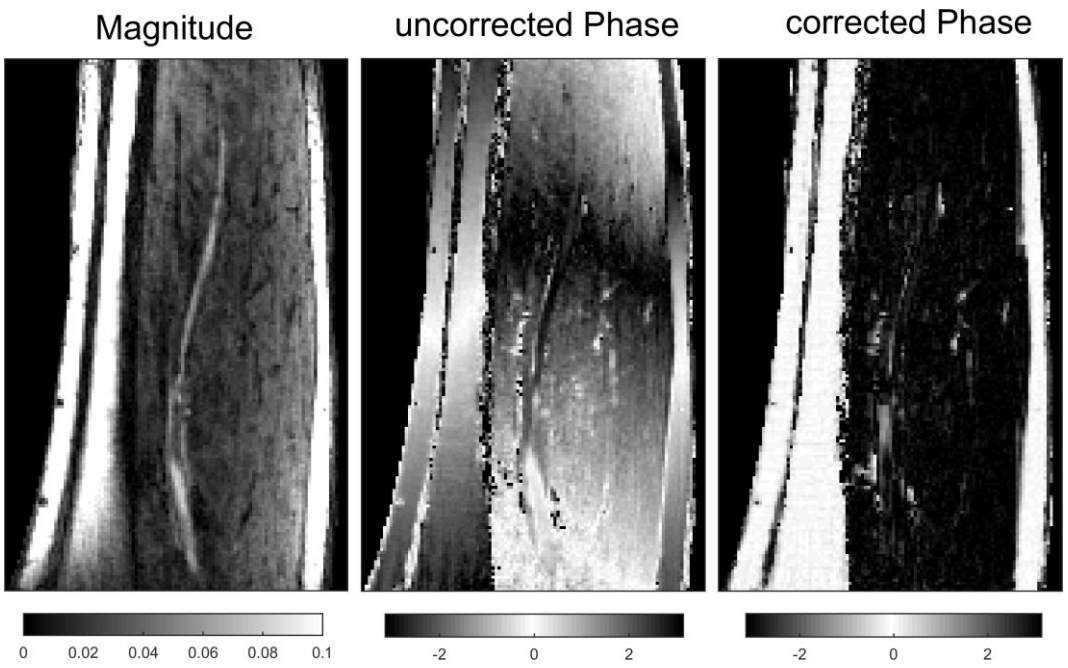

Figure 35: block regional phase correction in the lower leg. Shown is a fm-bSSFP acquisition of a sagittal slice of the lower leg as magnitude image (left), phase image before correction (middle) and phase image after correction (right). The slowly varying component seen in the middle panel is removed and an almost binary phase distribution remains.

Figure 36 shows the lower legs of a healthy volunteer scanned at 1.5T. The magnitude images of standard bSSFP acquisitions for two different phase-cycles ($\Delta\theta = 0°$ and $\Delta\theta = 180°$) display the typical banding artifacts. As can be seen in the phase image before correction each banding is accompanied by a sudden jump of π in signal phase (blue arrow). Additionally, jumps are seen at tissue boundaries as expected. The complex sum image as well as the frequency-modulated image show no bandings and subsequently only phase jumps at tissue boundaries. The slowly varying linear component is eliminated by the block regional phase correction in all images. Sudden jumps remain, regardless of their origin. As each jump is interpreted as a change in tissue, standard bSSFP images were not correctly separated into a water- or fat-only image. The complex sum image displays one minor swap of tissue (arrow), while no swaps are present in the frequency-modulated water- or fat-only images.

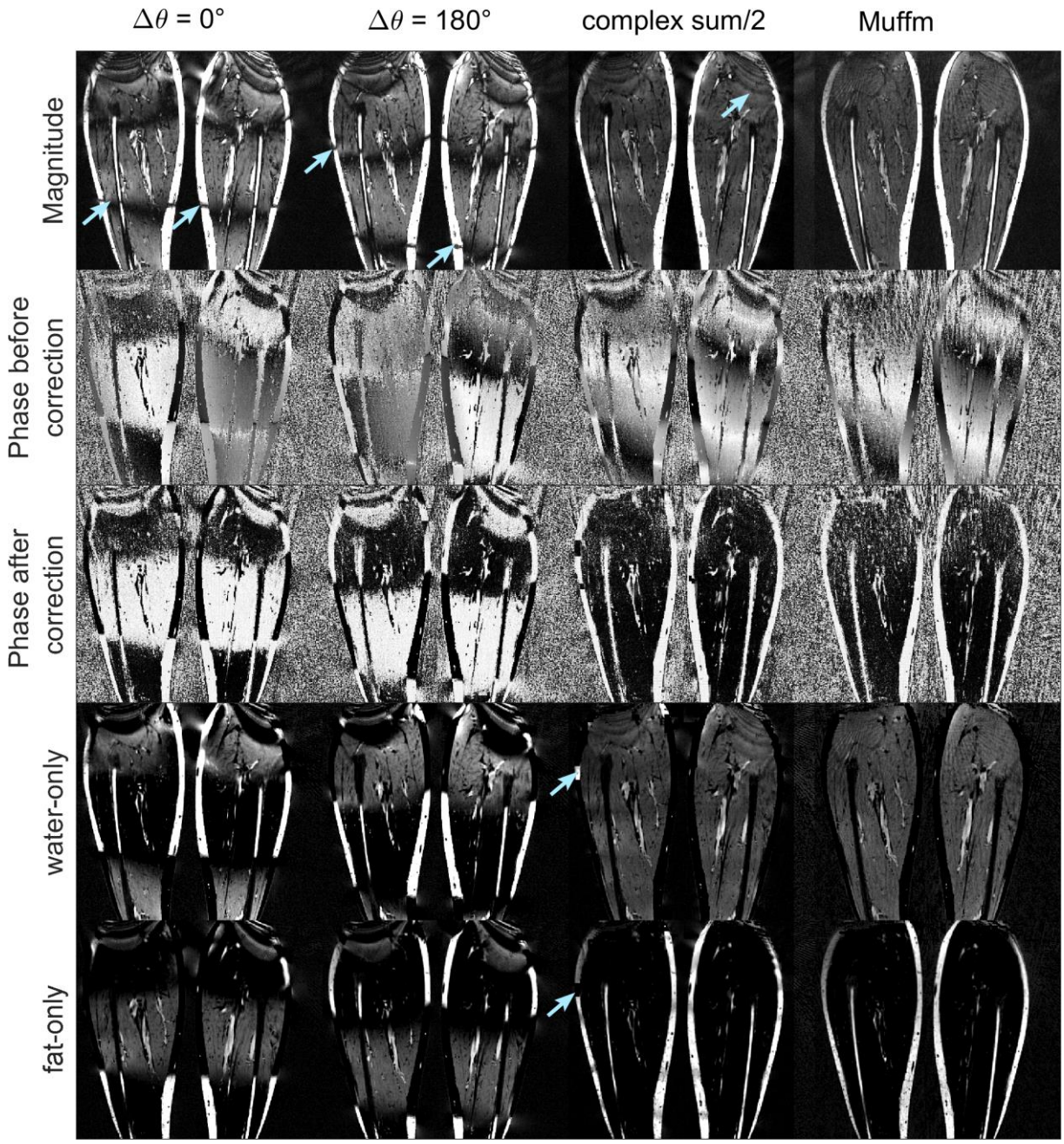

Figure 36: Coronal slice of the lower legs acquired at 1.5T. Shown is a) the Magnitude image, b) phase image before and c) after correction and d) the resulting water-only and e) fat-only images. First column: Standard bSSFP shows banding artifacts which are accompanied by a sudden jump in phase. As sudden changes are not corrected by the block regional phase correction a subsequent misinterpretation as tissue boundary is inevitable and major swaps between water and fat are seen. Second column: A different phase-cycle shifts the position of the banding artifacts but does not affect their impact. Major swaps are visible. Third column: The complex sum image shows some residual banding. Nevertheless, small swaps between tissues still occur (blue arrows). Fourth column: The fm-bSSFP image is free of visible banding. Minor swaps occur at the very edge of the FOV where strong inhomogeneities are encountered.

Measurements of the upper leg of a healthy volunteer are shown in Figure 37. They follow the same behavior as described in Figure 36. Due to the low signal and the closeness to the edge of the coil, strong streaking artifacts are present which exhibit a rapidly changing phase and therefore

disturb tissue classification in all acquisitions. While standard acquisitions suffer from general large-area tissue swaps the frequency-modulated images present stronger streaking and multiple small-scale swaps. Also, some additional minor bandings appear when using a non-selective RF-pulse, but do not influence the overall result as they are no accompanied by a phase jump.

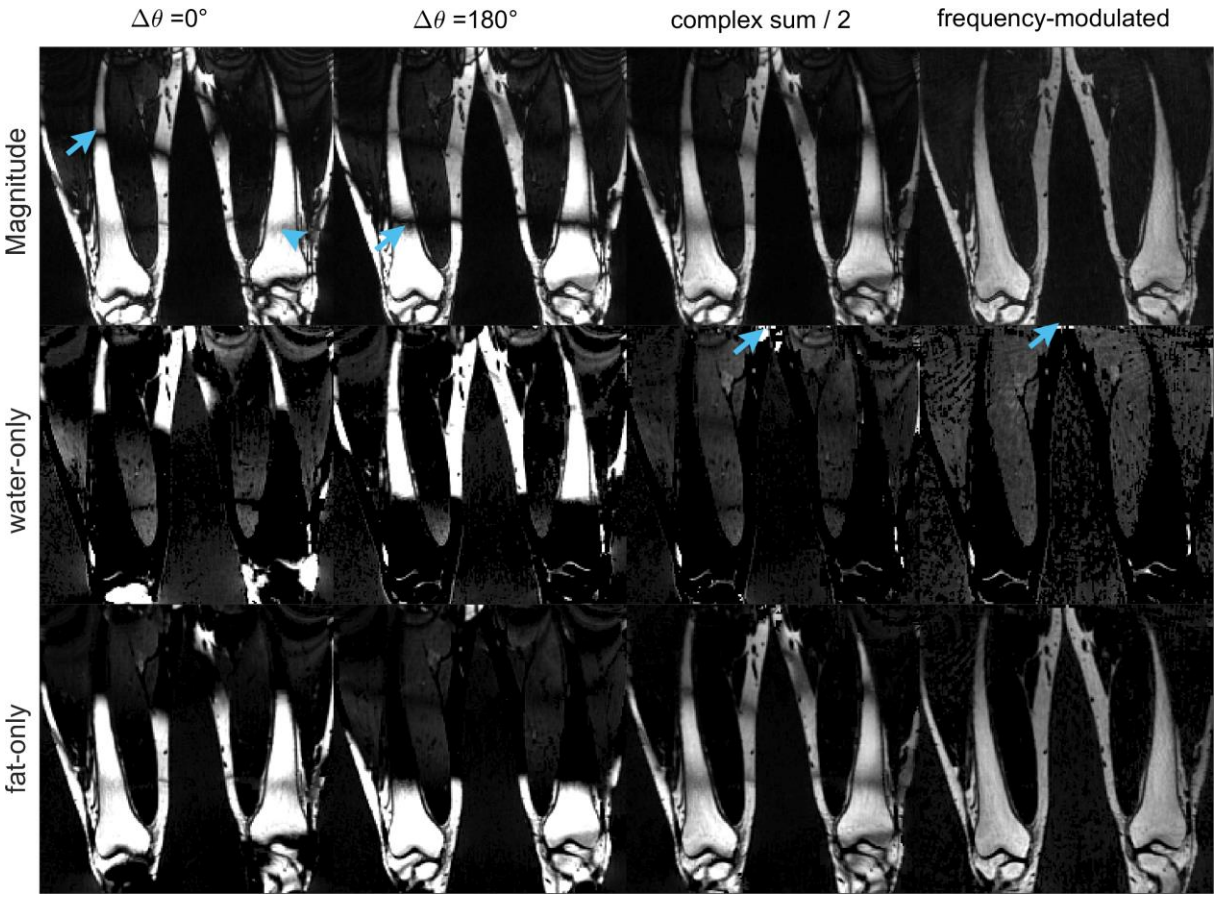

Figure 37: Coronal slice of the upper legs acquired at 3T. Shown is a) the Magnitude image, b) water-only and c) the fat-only image. First and second column: Again, standard bSSFP shows typical banding artifacts which lead to swaps in the water and fat assignments. Phase-cycling shifts the position of artifacts. When using a non-selective pulse, a dim shifted banding is visible but does not influence the outcome of the separation procedure (arowhead). Third column: Residual bandings and minor swaps in areas of high inhomogeneity can be seen in the complex sum reconstruction. Fourth column: fm-bSSFP successfully eliminates visible banding but minor swaps in areas of strong inhomogeneity remain.

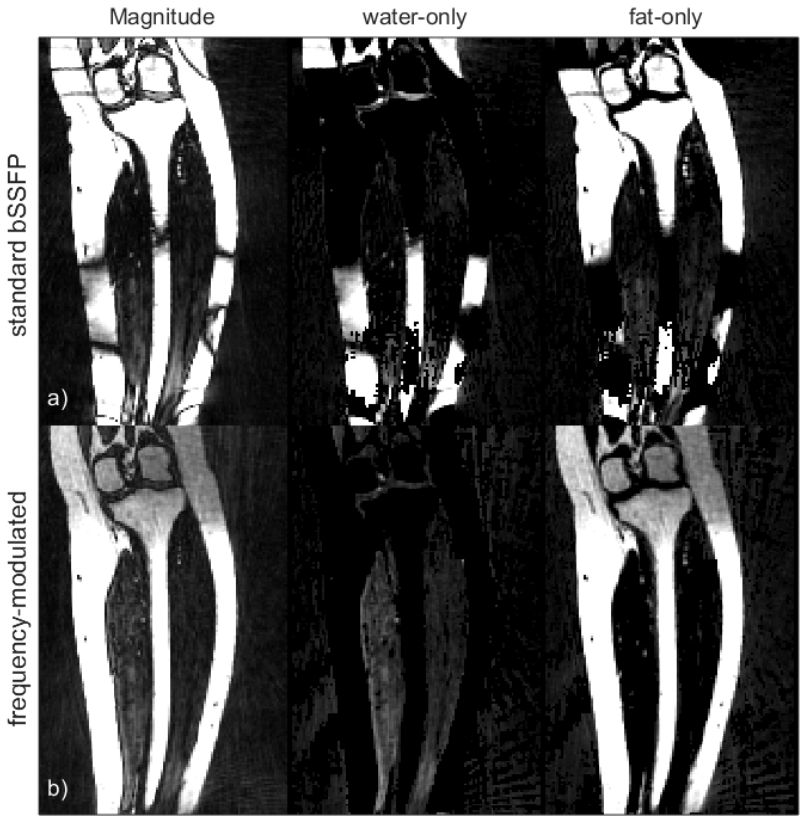

Figure 38: coronal slice of one lower leg measured at 3T using a slice selective pulse. A) standard bSSFP shows banding and unreliable tissue separation, while b) fm-bSSFP successfully suppressed banding and provides robust separation.

Displaying the maximum intensity projection of a water-only image provides an angiographic view. Figure 39 shows the same acquisition as Figure 36 plotted as a coronal MIP. In the inverted image areas of high intensity (vessels, fat) appear dark, while regions with low signal, like muscle are brighter. In standard bSSFP or even complex sum bSSFP the dark signal from falsely assigned fat tissue overlays the lighter structures of interest.

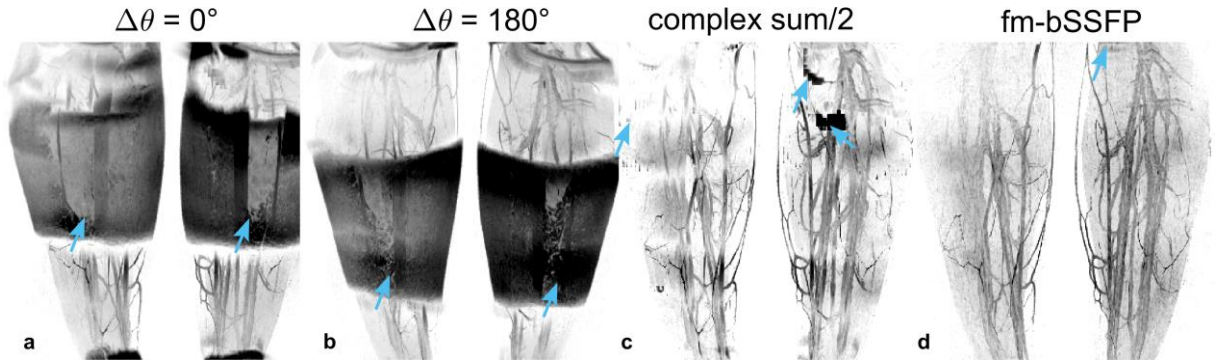

Figure 39: MIP projection of the water-only image after separation. High intensity blood vessels appear dark in the image and provide an angiographic view of the vasculature. Other water-like tissues like muscle provide a low background signal. In case of misassignment, the high signal intensity in fat overlays the desired view of the vasculature (blue arrows).

Magnitude images of the cross section of a lower leg show one, three and five bandings for TR values of 4.6, 13.8, 23 ms respectively. (Figure 40 a, c, e). The same effect can be seen for the water - oil- phantom. The increase in the spatial frequency of bandings can be nicely seen in the phantom. Also, a slight offset between the position of the same banding in water and in fat is discernible, showing nicely the effect of the chemical shift on resonance frequency.

Frequency-modulated acquisition of the same region in the leg provided banding free images. In the very homogeneous structure of the phantom residual banding is visible but greatly subdued in comparison to standard bSSFP. As before, bandings compromise the water fat separation algorithm in standard bSSFP, which performs worse with increasing TR values. In contrast, the separation works constantly fine in fm-bSSFP images, ignoring TR.

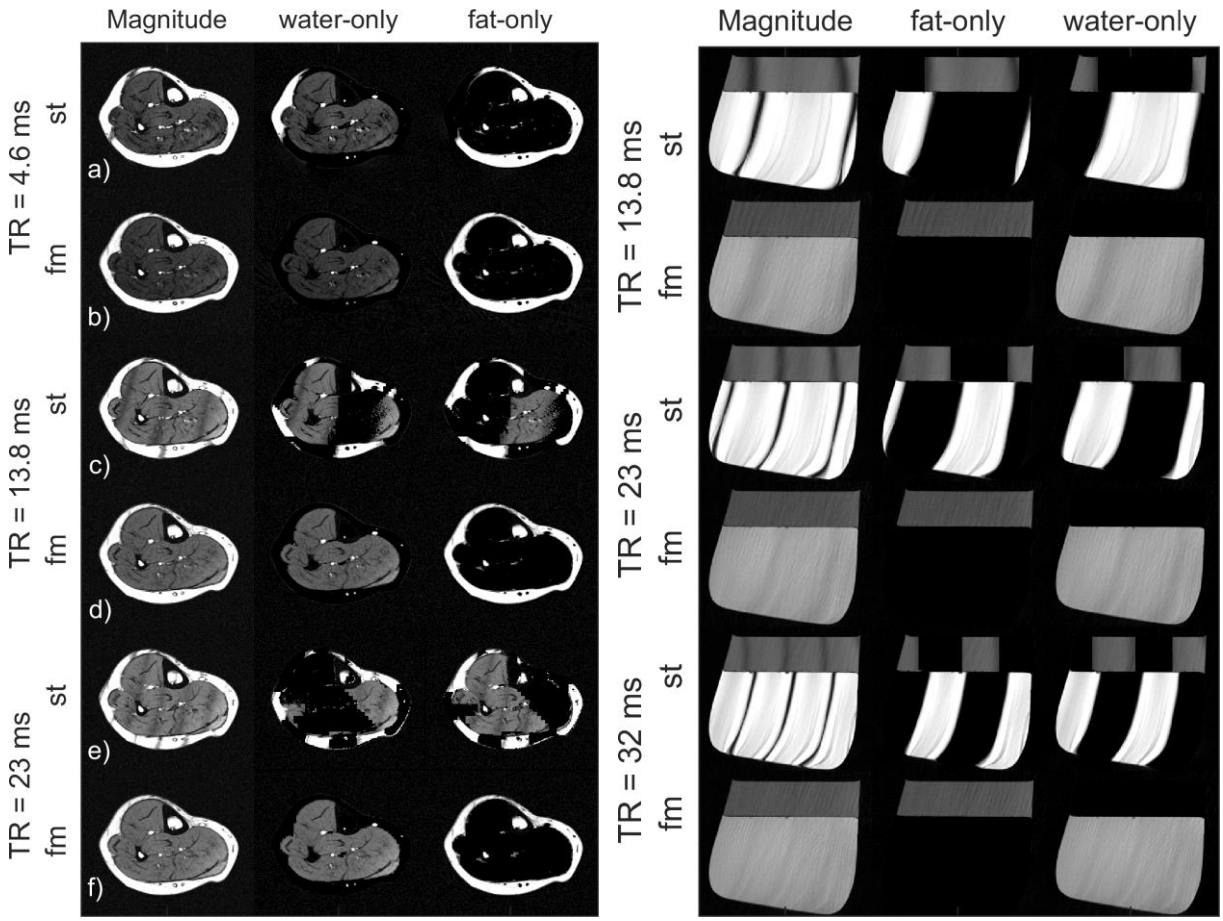

Figure 40: Water-fat separation in a phantom and the lower leg for measurements at different TR values and standard and fm-bSSFP. With increasing TR, banding artifacts become more frequent and closer spaced. Phase jumps in in the standard bSSFP (st) lead to tissue swaps, which are especially severe in high TR cases. The position of one banding is slightly shifted between water and fat due to the chemical shift between the two.

The water-fat separation procedure was also applied to measurements of the knee and the human heart, that were already shown in chapter 5.3.1. Both cases prove the robustness of the separation

process. As shown before banding free imaging is possible even in the presence of motion of the heart. The subsequent application of the separation procedure to different heartphases, shows tissue swaps in case of a standard bSSFP acquisition, but no swaps in fm-bSSFP (Figure 40).

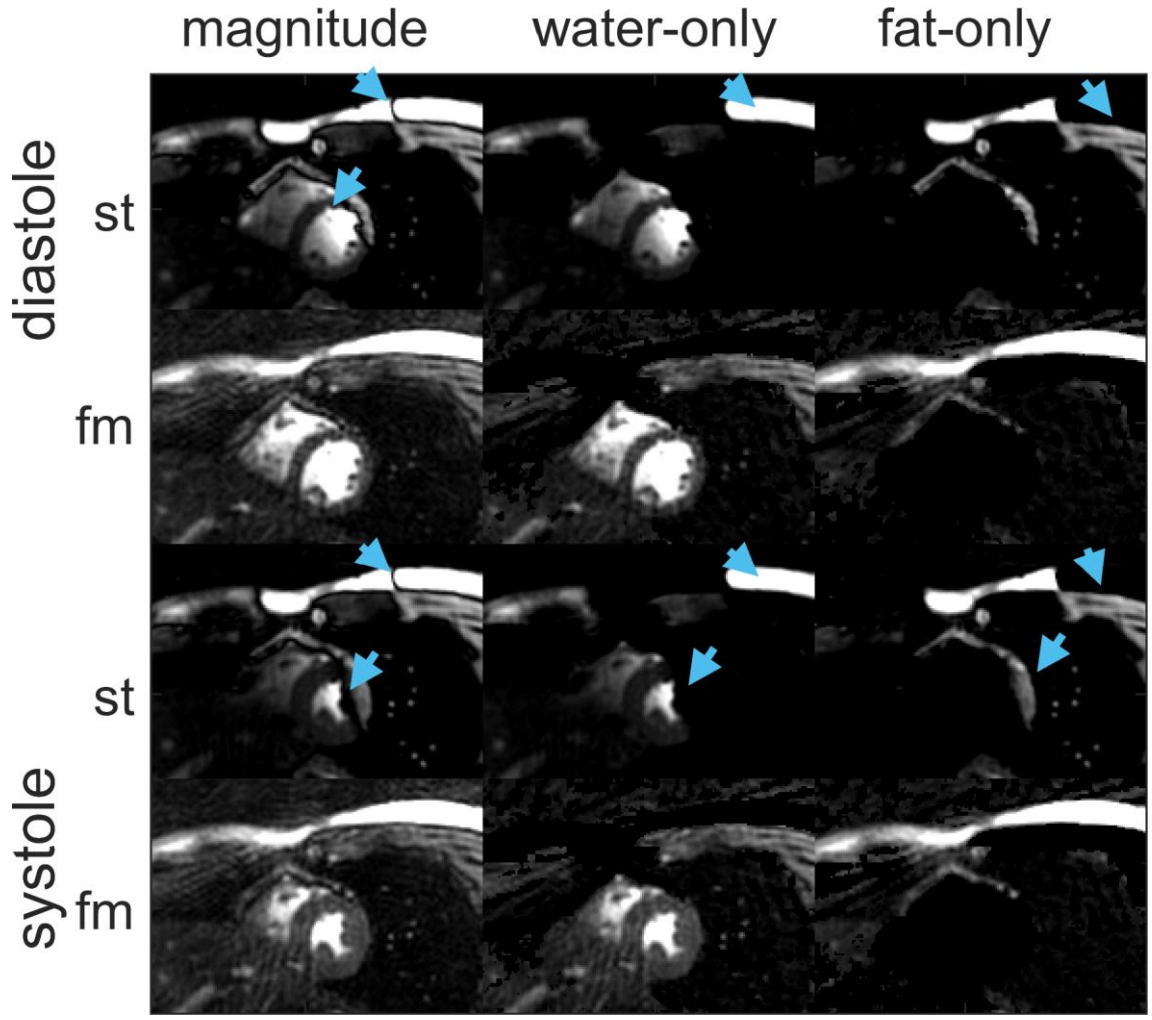

Figure 41: Water Fat Separation in a CINE sequence. Comparison of Magnitude, water-only and fat-only images in standard and fm-bSSFP. Shown are two exemplary heartphases in diastole (top) and systole (bottom). Wrongly assigned tissue areas in the standard bSSFP image are marked with blue arrows.

The human knee measurement shown in Figure 42 is of special interest as a discrepancy in the assignment of the pathology occurs (blue arrow). In standard bSSFP, after separation, the marked structure is assigned to the fat image, while in fm-bSSFP it is assigned to the water image. A banding artifact close to the structure of interest creates doubt on the reliability of the procedure.

As the pathology in question is located close to the femoropatellar joint it is likely a recess of the capsula filled with synovial fluid. Fatty tissue in this area is unlikely, especially as no trauma or fracture occurred. Fatty tumor tissue or lipoma are also highly improbable. Thus, the shape and

location as well as the doubt created by the visible banding, known to cause swaps in the separation algorithm, deem the assignment to water as correct.

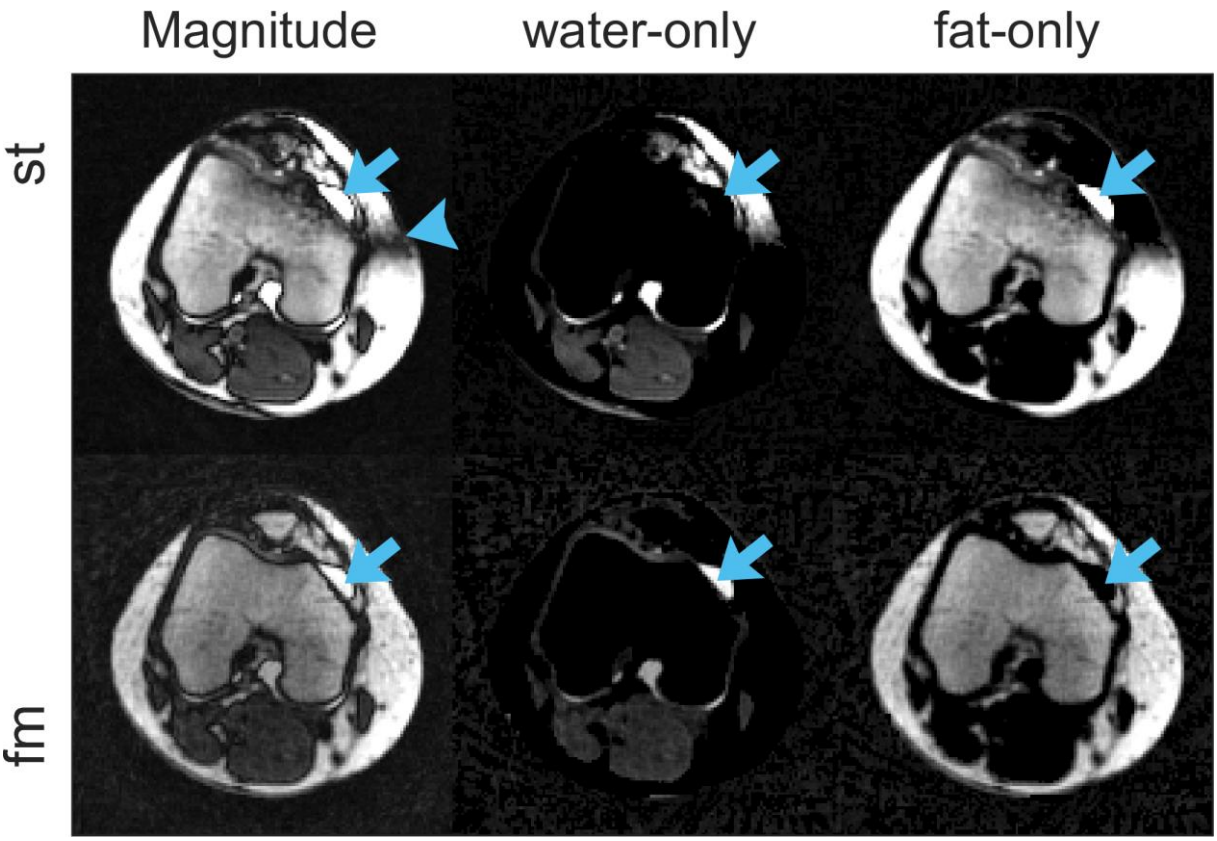

Figure 42 Water Fat Separation in the human knee. Note the different assignment of the very bright signal area in the upper right corner of the bone (blue arrows). Shape ad location suggest a recess in the capsula filled with synovial fluid, thus the assignment to water is more than likely the correct one.

6.4 Discussion

The phase sensitive separation of water and fat provides a voxel-wise classification of the tissue as water or fat. Unfortunately, in bSSFP sudden changes in phase can not only be caused by different tissue but also be due to offresonance effects. As the decision is solely based on the phase of the signal in the image wrong assignments occur at the position of banding artifacts.

Although it has been shown that a phase sensitive water fat separation is possible in a standard bSSFP acquisition (107,108), tissue swaps remain a problem and often extensive shimming, frequency scouts or manual correction are necessary. The example of synovial fluid in the human knee in Figure 42 shows the danger of misassignments of pathologies. While obvious in this case and without consequences, a misinterpretation and consequent wrong treatment based on a wrong assignment cannot be precluded.

To avoid tissue swaps, formerly a dual-acquisition was employed (109). The resulting signal features a linear and steady increase of phase with offresonance, while tissue boundaries still represent sudden changes. Nevertheless, depending on the tissue and imaging parameters, some oscillations remain in the magnitude as well as the phase of the signal. While these can be reduced by adding more phase-cycled acquisitions, there always remains a tradeoff between robustness to inhomogeneity and scan time.

As the frequency- modulated acquisition combines input from many different frequencies, the signal behavior was expected to behave like a combination of many phase-cycled acquisitions. In fact, simulated signals show a smooth magnitude and linear increasing phase independent of tissue or measurement parameters. A robust separation of water and fat was possible without visible banding artifacts or tissue swaps even in the presence of high field inhomogeneity, as shown in various measurements of a water-oil phantom or in human leg and cardiac measurements.

As the proposed method is based on the frequency-modulated acquisition and the phase-sensitive separation procedure, it suffers from the same drawbacks. Use of a frequency-modulated acquisition incurs some limitations regarding the choice of trajectory and maximum step size for the modulation (see chapter 5.4). The phase sensitive approach adds restrictions on the measurement parameters TR and TE. The ideal choice of TR as: $TR = n/(\,f_{water} - f_{fat})$, where n is an odd integer, and TE = TR/2, limits both parameters to set values. Especially for high field applications, the minimum values for n = 1 (TR~2.4ms at 3T) cannot always be reached for all measurement setups due to technical limitations. Changing to the next possible value for n = 3 can then increase the scan time in comparison to a measurement without TR restrictions.

Deviation from these ideal value shifts the relative position of the fat signal and therefore changes the difference in phase. In the current implementation of the block regional phase correction, a jump in phase of π is expected between tissues but deviation up to $\pi/2$ are acceptable. As the total phase accrual is combined from offresonance and chemical shift effects, a deviation in TR will limit the tolerable field inhomogeneity. In cases where perfect TR values cannot be reached, deviations are acceptable at the expense of robustness.

The phase sensitive separation is a binary approach, always assigning one label to each voxel. In comparison to DIXON like approaches it is not capable of defining fractions or partial volumes. The whole voxel is assigned to the more dominant tissue within that voxel. In general, a slight bias towards fat can be expected, as it sports higher intensity. Another consequence of the binary approach, reduces the complex fat spectrum to the main fat peak only. A multi-peak fat model cannot be introduced in the method without major changes.

In general, the TR of a measurement can be chosen according to the chemical shift of arbitrary materials to be separated in an MR image. This might make the approach interesting for other applications like detection of ruptures in silicone gel implants (110) or movement of silicone oil in ophthalmologic treatments (111) or in the field of material science.

All in all, the main advantages of the proposed procedure lie in the robustness against field inhomogeneity which prevents tissue swaps like seen in standard bSSFP or even dual-acquisition. In comparison to the latter, scan times are significantly shorter resulting in higher efficiency and patient comfort. This renders the phase-sensitive water-fat separation in a frequency-modulated acquisition an interesting option for fast, high SNR bSSFP applications.

7 Summary

This work considered the frequency-modulated balanced steady-state free precession (fm-bSSFP) sequence as a tool to provide banding free bSSFP MR images. The sequence was implemented and successfully applied to suppress bandings in various in vitro and in vivo examples. In combination with a radial trajectory it is a promising alternative for standard bSSFP applications. First, two specialized applications were shown to establish the benefits of the acquisition strategy in itself. In real time cardiac imaging, it was shown that the continuous shift in frequency causes a movement of the bandings across the FOV. Thus, no anatomical region is constantly impaired, and a suitable timeframe can be found to examine all important structures. Furthermore, a combination of images with different artifact positions, similar to phase-cycled acquisitions is possible. In this way, fast, banding-free imaging of the moving heart was realized. Second, acquisitions with long TR were shown. While standard bSSFP suffers from increasing incidence of bandings with higher TR values, the frequency-modulated approach provided banding free images, regardless of the TR.

A huge disadvantage of fm-bSSFP, in combination with the radial trajectory, is the decrease in signal intensity. In this work a specialized reconstruction method, the multifrequency reconstruction for frequency-modulated bSSFP (Muffm), was established, which successfully compensated that phenomena. The application of Muffm to several anatomical sites, such as inner ear, legs and cardiac acquisitions, proofed the advantageous SNR of the reconstruction.

Furthermore, fm-bSSFP was applied to the clinically highly relevant task of water-fat separation. Former approaches of a phase-sensitive separation procedure in combination with standard bSSFP showed promising results but failed in cases of high inhomogeneity or high field strengths where banding artifacts become a major issue. The novel approach of using the fm-bSSFP acquisition strategy with the separation approach provided robust, reliable images of high quality. Again, losses in signal intensity could be regained by Muffm, as both approaches are completely compatible.

Opposed to conventional banding suppression techniques, like frequency-scouts or phase-cycling, all reconstruction methods established in this work rely on a single radial acquisition, with scan times similar to standard bSSFP scans. No prolonged measurement times occur and patient time in the scanner is kept as short as possible, improving patient comfort, susceptibility to motion or physiological noise and cost of one scan.

All in all, the frequency-modulated acquisition in combination with specializes reconstruction methods, leads to a completely new quality of images with short acquisition times.

8 Zusammenfassung

In dieser Arbeit wird eine Modifikation der balanced steady-state free precession (bSSFP) Sequenz betrachtet. Die frequenzmodulierte bSSFP-Sequenz (fm-bSSFP) kann die sonst typischen Band-Artefakte in bSSFP-MR-Bildern verhindern. Die Sequenz wurde im Rahmen der Arbeit am MR-Scanner implementiert und erfolgreich in verschiedenen in-vitro- und in-vivo-Beispielen angewendet. In Kombination mit einer radialen Trajektorie erwies es sich als eine vielversprechende Alternative für alle Standard-bSSFP Anwendungen.

Zuerst wurden zwei spezialisierte Anwendungen gezeigt, um die Vorteile der Akquisitionsstrategie an sich darzustellen. Am Beispiel der Echtzeit-Herzbildgebung konnte mit Hilfe der kontinuierlichen Frequenzverschiebung eine Bewegung der Bänder über das FOV erzeugt werden. Somit wird keine anatomische Region ständig von Artefakten überlagert und für jeden Bereich kann ein geeigneter Zeitrahmen gefunden werden, um die wichtigen Strukturen darzustellen und zu untersuchen. Darüber hinaus ist eine Kombination von Bildern mit verschiedenen Artefaktpositionen möglich, ähnlich zu mehreren Aufnahmen mit verschiedenen Phasenzyklen. Auf diese Weise wurde eine schnelle Bildgebung des sich bewegenden Herzens ohne Bandartefakte realisiert.

Zusätzlich wurden Aufnahmen mit langen Repetitionszeiten (TR) untersucht. Während in der Standard-bSSFP die Häufigkeit von Bandartefakten mit steigendem TR-Wert zunimmt, lieferte der frequenzmodulierte Ansatz Banding-freie Bilder unabhängig vom TR.
Ein großer Nachteil von fm-bSSFP in Kombination mit der radialen Trajektorie ist der Verlust von Signalintensität bei der Rekonstruktion. In dieser Arbeit wurde eine spezielle Rekonstruktionsmethode namens Muffm (mulitfrequency reconstruction for frequency-modulated bSSFP) etabliert, die diesen Verlust erfolgreich kompensieren kann. Die Anwendung von Muffm an verschiedenen anatomischen Strukturen, wie Innenohr, Bein und Herzaufnahmen, bestätigte das vorteilhafte Signal-zu-Rausch-Verhältnis, dass durch die spezielle Rekonstruktion gewonnen werden kann.

Darüber hinaus wurde die fm-bSSFP auf die klinisch interessante Wasser-Fett-Trennung angewandt. Frühere Ansätze eines phasenempfindlichen Trennverfahrens in Kombination mit Standard-bSSFP zeigten vielversprechende Ergebnisse, scheiterten jedoch in Fällen hoher Inhomogenität oder hoher Feldstärken an den auftretenden Bandartefakten. Der neue Ansatz, diesen Separationsalgorithmus mit der fm-bSSFP-Akquisitionsstrategie zu verbinden, lieferte robuste, zuverlässige Bilder von hoher Qualität. Auch hier konnten entstehende Verluste in der Signalintensität durch Muffm zurückgewonnen werden, da beide Ansätze vollständig kompatibel

sind.

Im Gegensatz zu herkömmlichen Bandunterdrückungstechniken, wie Frequenz-Scouts oder die Aufnahme mehrerer Bilder mit verschiedenen Phasenzyklen, beruhen alle in dieser Arbeit etablierten Rekonstruktionsverfahren auf einer einzigen radialen Aufnahme. Die Messzeiten sind daher identisch zur Aufnahme einer Standard-bSSFP Messung. Das Verfahren ermöglicht eine deutliche Verkürzung der Aufenthaltsdauer im Scanner bei einer gleichzeitigen Garantie ein artefaktfreies Bild zu erhalten. Damit ist es insbesondere für Patienten von Vorteil, die unter Platzangst oder sonstigen Beschwerden leiden, die ein langes Stillliegen erschweren. Außerdem werden Bewegungsartefakte, physiologisches Rauschen und nicht zuletzt die Kosten eines Scans minimiert.

Insgesamt bietet die frequenzmodulierte bSSFP Aufnahme in Kombination mit spezialisierten Rekonstruktionsverfahren neue Möglichkeiten zur schnellen Aufnahme von Bildern ohne Bandartefakte.

III. Bibliography

1. The Organisation for Economic Co-operation and Development (OECD). Health equipment - Magnetic resonance imaging (MRI) units - OECD Data. theOECD [Internet] 2018. (Accessed on 04 January 2018)

2. The Organisation for Economic Co-operation and Development (OECD). Health equipment - Computed tomography (CT) scanners - OECD Data. theOECD [Internet] 2018. (Accessed on 04 January 2018)

3. Bieri O, Scheffler K. Fundamentals of balanced steady state free precession MRI. J. Magn. Reson. Imaging 2013;38:2–11. doi: 10.1002/jmri.24163.

4. Carr HY. Steady-State Free Precession in Nuclear Magnetic Resonance. Phys. Rev. 1958;112:1693–1701. doi: 10.1103/PhysRev.112.1693.

5. Freeman R, Hill HDW. Phase and intensity anomalies in fourier transform NMR. J. Magn. Reson. 1969 1971;4:366–383. doi: 10.1016/0022-2364(71)90047-3.

6. Oppelt A, Graumann R, Barfuss H, Fischer H, Hartl W, Schajor W. FISP, a novel, fast pulse sequence for nuclear magnetic resonance imaging. Electromedica 1986;54:15–18.

7. Ross JS. MR imaging of the cervical spine: techniques for two- and three-dimensional imaging. Am. J. Roentgenol. 1992;159:779–786. doi: 10.2214/ajr.159.4.1529843.

8. Chung H-W, Chen C-Y, Zimmerman RA, Lee K-W, Lee C-C, Chin S-C. T2-Weighted Fast MR Imaging with True FISP Versus HASTE. Am. J. Roentgenol. 2000;175:1375–1380. doi: 10.2214/ajr.175.5.1751375.

9. Vasanawala SS, Pauly JM, Nishimura DG. Linear combination steady-state free precession MRI. Magn. Reson. Med. 2000;43:82–90. doi: 10.1002/(SICI)1522-2594(200001)43:1<82::AID-MRM10>3.0.CO;2-9.

10. Plein S, Bloomer TN, Ridgway JP, Jones TR, Bainbridge GJ, Sivananthan MU. Steady-state free precession magnetic resonance imaging of the heart: Comparison with segmented k-space gradient-echo imaging. J. Magn. Reson. Imaging 2001;14:230–236. doi: 10.1002/jmri.1178.

11. Fuchs F, Laub G, Othomo K. TrueFISP—technical considerations and cardiovascular applications. Eur. J. Radiol. 2003;46:28–32. doi: 10.1016/S0720-048X(02)00330-3.

12. Schär M, Kozerke S, Fischer SE, Boesiger P. Cardiac SSFP imaging at 3 Tesla. Magn. Reson. Med. 2004;51:799–806. doi: 10.1002/mrm.20024.

13. Nayak KS, Hu BS. The future of real-time cardiac magnetic resonance imaging. Curr. Cardiol. Rep. 2005;7:45–51. doi: 10.1007/s11886-005-0010-x.

14. Scheffler K, Ehses P. High-resolution mapping of neuronal activation with balanced SSFP at 9.4 tesla. Magn. Reson. Med. 2016;76:163–171. doi: 10.1002/mrm.25890.

15. Zeineh M, Parekh M, Zaharchuk G, Su J, Rosenberg J, Fischbein N, Rutt B. Ultra-High Resolution Imaging of the Human Brain with Phase-Cycled Balanced Steady State Free Precession at 7.0T. Invest. Radiol. 2014;49:278–289. doi: 10.1097/RLI.0000000000000015.

16. Chavhan GB, Babyn PS, Jankharia BG, Cheng H-LM, Shroff MM. Steady-State MR Imaging Sequences: Physics, Classification, and Clinical Applications. RadioGraphics 2008;28:1147–1160. doi: 10.1148/rg.284075031.

17. Hargreaves B. Rapid Gradient-Echo Imaging. J. Magn. Reson. Imaging JMRI 2012;36:1300–1313. doi: 10.1002/jmri.23742.

18. Dharmakumar R, Wright GA. Understanding steady-state free precession: A geometric perspective. Concepts Magn. Reson. Part A 2005;26A:1–10. doi: 10.1002/cmr.a.20033.

19. Matt A. Bernstein, King KF, Zhou XJ. Handbook of MRI pulse sequences. Burlington, MA: Elsevier Academic Press; 2004.

20. Zur Y, Wood ML, Neuringer LJ. Spoiling of transverse magnetization in steady-state sequences. Magn. Reson. Med. 1991;21:251–263. doi: 10.1002/mrm.1910210210.

21. Elster AD. Gradient-echo MR imaging: techniques and acronyms. Radiology 1993;186:1–8. doi: 10.1148/radiology.186.1.8416546.

22. Ernst RR, Anderson WA. Application of Fourier Transform Spectroscopy to Magnetic Resonance. Rev. Sci. Instrum. 1966;37:93–102. doi: 10.1063/1.1719961.

23. Zur Y, Wood ML, Neuringer LJ. Motion-insensitive, steady-state free precession imaging. Magn. Reson. Med. 1990;16:444–459. doi: 10.1002/mrm.1910160311.

24. Zur Y, Stokar S, Bendel P. An analysis of fast imaging sequences with steady-state transverse magnetization refocusing. Magn. Reson. Med. 1988;6:175–193. doi: 10.1002/mrm.1910060206.

25. Scheffler K. A pictorial description of steady-states in rapid magnetic resonance imaging. Concepts Magn. Reson. 1999;11:291–304. doi: 10.1002/(SICI)1099-0534(1999)11:5<291::AID-CMR2>3.0.CO;2-J.

26. Oshinski JN, Delfino JG, Sharma P, Gharib AM, Pettigrew RI. Cardiovascular magnetic resonance at 3.0T: Current state of the art. J. Cardiovasc. Magn. Reson. 2010;12:55. doi: 10.1186/1532-429X-12-55.

27. Feng X, Salerno M, Kramer CM, Meyer CH. Non-Cartesian balanced steady-state free precession pulse sequences for real-time cardiac MRI. Magn. Reson. Med. 2016;75:1546–1555. doi: 10.1002/mrm.25738.

28. Boll DT, Lewin JS, Duerk JL, Aschoff AJ, Merkle EM. Comparison of MR imaging sequences for liver and head and neck interventions: Is there a single optimal sequence for all purposes?1. Acad. Radiol. 2004;11:506–515. doi: 10.1016/S1076-6332(03)00818-3.

29. Miyazaki M, Isoda H. Non-contrast-enhanced MR angiography of the abdomen. Eur. J. Radiol. 2011;80:9–23. doi: 10.1016/j.ejrad.2011.01.093.

30. Morita S, Masukawa A, Suzuki K, Hirata M, Kojima S, Ueno E. Unenhanced MR Angiography: Techniques and Clinical Applications in Patients with Chronic Kidney Disease. RadioGraphics 2011;31:E13–E33. doi: 10.1148/rg.312105075.

31. Guirado CR, Martν≠nez P, Roig R, Mirosa F, Salmerν≥n J, Florensa F, Roger M, Barragν°n Y. Three-dimensional MR of the inner ear with steady-state free precession. Am. J. Neuroradiol. 1995;16:1909–1913.

32. Sheth S, Branstetter BF, Escott EJ. Appearance of Normal Cranial Nerves on Steady-State Free Precession MR Images. RadioGraphics 2009;29:1045–1055. doi: 10.1148/rg.294085743.

33. Martin DR, Danrad R, Herrmann K, Semelka RC, Hussain SM. Magnetic Resonance Imaging of the Gastrointestinal Tract. Top. Magn. Reson. Imaging 2005;16:77. doi: 10.1097/01.rmr.0000179461.55234.7d.

34. Schieda N, Isupov I, Chung A, Coffey N, Avruch L. Practical applications of balanced steady-state free-precession (bSSFP) imaging in the abdomen and pelvis. J. Magn. Reson. Imaging 2017;45:11–20. doi: 10.1002/jmri.25336.

35. Anquez J, Angelini E, Bloch I, Merzoug V, Bellaiche-Millischer AE, Adamsbaum C. Interest of the steady state free precession (SSFP) sequence for 3D modeling of the whole fetus. Conf. Proc. Annu. Int. Conf. IEEE Eng. Med. Biol. Soc. IEEE Eng. Med. Biol. Soc. Annu. Conf. 2007;2007:771–774. doi: 10.1109/IEMBS.2007.4352404.

36. Bieri O, Mamisch TC, Trattnig S, Scheffler K. Steady state free precession magnetization transfer imaging. Magn. Reson. Med. 2008;60:1261–1266. doi: 10.1002/mrm.21781.

37. Bieri O, Scheffler K. Optimized balanced steady-state free precession magnetization transfer imaging. Magn. Reson. Med. 2007;58:511–518. doi: 10.1002/mrm.21326.

38. Gloor M, Scheffler K, Bieri O. Quantitative magnetization transfer imaging using balanced SSFP. Magn. Reson. Med. 2008;60:691–700. doi: 10.1002/mrm.21705.

39. Bär S, Weigel M, von Elverfeldt D, Hennig J, Leupold J. Intrinsic diffusion sensitivity of the balanced steady-state free precession (bSSFP) imaging sequence. NMR Biomed. 2015;28:1383–1392. doi: 10.1002/nbm.3380.

40. Cheung MM, Wu EX. Diffusion imaging with balanced steady state free precession. In: 2012 Annual International Conference of the IEEE Engineering in Medicine and Biology Society. ; 2012. pp. 90–93. doi: 10.1109/EMBC.2012.6345878.

41. Miller KL, Smith SM, Jezzard P, Pauly JM. High-resolution FMRI at 1.5T using balanced SSFP. Magn. Reson. Med. 2006;55:161–170. doi: 10.1002/mrm.20753.

42. Miller KL. FMRI using balanced steady-state free precession (SSFP). Neuroimage 2012;62:713–719. doi: 10.1016/j.neuroimage.2011.10.040.

43. Cheng JS, Gao PP, Zhou IY, Chan RW, Chan Q, Mak HK, Khong PL, Wu EX. Resting-State fMRI Using Passband Balanced Steady-State Free Precession. PLoS ONE [Internet] 2014;9. doi: 10.1371/journal.pone.0091075.

44. Kim TS, Lee J, Lee JH, Glover GH, Pauly JM. Analysis of the BOLD characteristics in pass-band bSSFP fMRI. Int. J. Imaging Syst. Technol. 2012;22:23–32. doi: 10.1002/ima.21296.

45. Scheffler K, Lehnhardt S. Principles and applications of balanced SSFP techniques. Eur. Radiol. 2003;13:2409–2418. doi: 10.1007/s00330-003-1957-x.

46. Benkert T, Ehses P, Blaimer M, Jakob PM, Breuer FA. Dynamically phase-cycled radial balanced SSFP imaging for efficient banding removal. Magn. Reson. Med. 2015;73:182–194. doi: 10.1002/mrm.25113.

47. Deshpande VS, Shea SM, Li D. Artifact reduction in true-FISP imaging of the coronary arteries by adjusting imaging frequency. Magn. Reson. Med. 2003;49:803–809. doi: 10.1002/mrm.10442.

48. Tang Y-W, Huang T-Y, Wu W-C. Fast and fully automatic calibration of frequency offset for balanced steady-state free precession cardiovascular magnetic resonance at 3.0 Tesla. J. Cardiovasc. Magn. Reson. 2013;15:32. doi: 10.1186/1532-429X-15-32.

49. Bangerter NK, Hargreaves BA, Vasanawala SS, Pauly JM, Gold GE, Nishimura DG. Analysis of multiple-acquisition SSFP. Magn. Reson. Med. 2004;51:1038–1047. doi: 10.1002/mrm.20052.

50. Bjork M, Ingle RR, Gudmundson E, Stoica P, Nishimura DG, Barral JK. Parameter Estimation Approach to Banding Artifact Reduction in Balanced Steady-State Free Precession. Magn. Reson. Med. 2014;72:880–892. doi: 10.1002/mrm.24986.

51. Lauzon ML, Frayne R. Analytical characterization of RF phase-cycled balanced steady-state free precession. Concepts Magn. Reson. Part A 2009;34A:133–143. doi: 10.1002/cmr.a.20138.

52. Elliott AM, Bernstein MA, Ward HA, Lane J, Witte RJ. Nonlinear averaging reconstruction method for phase-cycle SSFP. Magn. Reson. Imaging 2007;25:359–364. doi: 10.1016/j.mri.2006.09.013.

53. Casselman JW, Kuhweide R, Deimling M, Ampe W, Dehaene I, Meeus L. Constructive interference in steady state-3DFT MR imaging of the inner ear and cerebellopontine angle. Am. J. Neuroradiol. 1993;14:47–57.

54. Çukur T, Bangerter NK, Nishimura DG. Enhanced spectral shaping in steady-state free precession imaging. Magn. Reson. Med. 2007;58:1216–1223. doi: 10.1002/mrm.21413.

55. Çukur T, Lustig M, Nishimura DG. Multiple-profile homogeneous image combination: Application to phase-cycled SSFP and multicoil imaging. Magn. Reson. Med. 2008;60:732–738. doi: 10.1002/mrm.21720.

56. Foxall D l. Frequency-modulated steady-state free precession imaging. Magn. Reson. Med. 2002;48:502–508. doi: 10.1002/mrm.10225.

57. Benkert T, Ehses P, Blaimer M, Jakob PM, Breuer FA. Dynamically phase-cycled radial balanced SSFP imaging for efficient banding removal. Magn. Reson. Med. 2015;73:182–194. doi: 10.1002/mrm.25113.

58. Markl M, Leupold J. Gradient echo imaging. J. Magn. Reson. Imaging 2012;35:1274–1289. doi: 10.1002/jmri.23638.

59. Benkert T, Ehses P, Blaimer M, Jakob PM, Breuer FA. Fast isotropic banding-free bSSFP imaging using 3D dynamically phase-cycled radial bSSFP (3D DYPR-SSFP). Z. Für Med. Phys. 2016;26:63–74. doi: 10.1016/j.zemedi.2015.05.001.

60. Bloch F. Nuclear Induction. Phys. Rev. 1946;70:460–474. doi: 10.1103/PhysRev.70.460.

61. Hargreaves BA, Vasanawala SS, Pauly JM, Nishimura DG. Characterization and reduction of the transient response in steady-state MR imaging. Magn. Reson. Med. 2001;46:149–158. doi: 10.1002/mrm.1170.

62. Jaynes ET. Matrix Treatment of Nuclear Induction. Phys. Rev. 1955;98:1099–1105. doi: 10.1103/PhysRev.98.1099.

63. Hargreaves BA. Bloch Equation Simulation. http://mrsrl.stanford.edu/~brian/bloch/,(Accessed on 07 November 2017)

64. Noll DC. Multishot rosette trajectories for spectrally selective MR imaging. IEEE Trans. Med. Imaging 1997;16:372–377. doi: 10.1109/42.611345.

65. Feng H, Gu H, Silbersweig D, Stern E, Yang Y. Single-shot MR imaging using trapezoidal-gradient-based Lissajous trajectories. IEEE Trans. Med. Imaging 2003;22:925–932. doi: 10.1109/TMI.2003.815902.

66. Ahn CB, Kim JH, Cho ZH. High-Speed Spiral-Scan Echo Planar NMR Imaging-I. IEEE Trans. Med. Imaging 1986;5:2–7. doi: 10.1109/TMI.1986.4307732.

67. Waterton JC, Jenkins JPR, Zhu XP, Love HG, Isherwood I, Rowlands DJ. Magnetic resonance (MR) cine imaging of the human heart. Br. J. Radiol. 1985;58:711–716. doi: 10.1259/0007-1285-58-692-711.

68. Bley TA, Wieben O, François CJ, Brittain JH, Reeder SB. Fat and water magnetic resonance imaging. J. Magn. Reson. Imaging 2010;31:4–18. doi: 10.1002/jmri.21895.

69. Yu H, Shimakawa A, McKenzie CA, Brodsky E, Brittain JH, Reeder SB. Multiecho water-fat separation and simultaneous R 2* estimation with multifrequency fat spectrum modeling. Magn. Reson. Med. 2008;60:1122–1134. doi: 10.1002/mrm.21737.

70. Ma J. Dixon techniques for water and fat imaging. J. Magn. Reson. Imaging JMRI 2008;28:543–558. doi: 10.1002/jmri.21492.

71. Hu HH, Börnert P, Hernando D, Kellman P, Ma J, Reeder S, Sirlin C. ISMRM workshop on fat–water separation: Insights, applications and progress in MRI. Magn. Reson. Med. 2012;68:378–388. doi: 10.1002/mrm.24369.

72. Haase A, Frahm J, Hänicke W, Matthaei D. 1H NMR chemical shift selective (CHESS) imaging. Phys. Med. Biol. 1985;30:341–344.

73. Meyer CH, Pauly JM, Macovskiand A, Nishimura DG. Simultaneous spatial and spectral selective excitation. Magn. Reson. Med. 1990;15:287–304. doi: 10.1002/mrm.1910150211.

74. Bydder GM, Pennock JM, Steiner RE, Khenia S, Payne JA, Young IR. The short TI inversion recovery sequence--an approach to MR imaging of the abdomen. Magn. Reson. Imaging 1985;3:251–254.

75. Yuan J, Madore B, Panych LP. Fat-water selective excitation in balanced steady-state free precession using short spatial-spectral RF pulses. J. Magn. Reson. 2011;208:219–224. doi: 10.1016/j.jmr.2010.11.005.

76. Ribot EJ, Wecker D, Trotier AJ, Dallaudière B, Lefrançois W, Thiaudière E, Franconi J-M, Miraux S. Water Selective Imaging and bSSFP Banding Artifact Correction in Humans and Small Animals at 3T and 7T, Respectively. PLoS ONE 2015;10:e0139249. doi: 10.1371/journal.pone.0139249.

77. Deshpande VS, Shea SM, Laub G, Simonetti OP, Finn JP, Li D. 3D magnetization-prepared true-FISP: A new technique for imaging coronary arteries. Magn. Reson. Med. 2001;46:494–502. doi: 10.1002/mrm.1219.

78. Scheffler K, Heid O, Hennig J. Magnetization preparation during the steady state: fat-saturated 3D TrueFISP. Magn. Reson. Med. 2001;45:1075–1080.

79. Leupold J, Wieben O, Månsson S, Speck O, Scheffler K, Petersson JS, Hennig J. Fast chemical shift mapping with multiecho balanced SSFP. Magn. Reson. Mater. Phys. Biol. Med. 2006;19:267–273. doi: 10.1007/s10334-006-0056-9.

80. Quist B, Hargreaves BA, Daniel BL, Saranathan M. Balanced SSFP Dixon imaging with banding-artifact reduction at 3 Tesla. Magn. Reson. Med. 2015;74:706–715. doi: 10.1002/mrm.25449.

81. Kim H, Pinus AB, Wang J, Murphy PS, Constable RT. On the application of chemical shift-based multipoint water-fat separation methods in balanced SSFP imaging. Magn. Reson. Med. 2007;58:413–418. doi: 10.1002/mrm.21303.

82. Henze Bancroft LC, Strigel RM, Hernando D, Johnson KM, Kelcz F, Kijowski R, Block WF. Utilization of a balanced steady state free precession signal model for improved fat/water decomposition. Magn. Reson. Med. 2016;75:1269–1277. doi: 10.1002/mrm.25728.

83. Overall WR, Nishimura DG, Hu BS. Steady-state sequence synthesis and its application to efficient fat-suppressed imaging. Magn. Reson. Med. 2003;50:550–559. doi: 10.1002/mrm.10542.

84. Wansapura JP. Abdominal fat–water separation with SSFP at 3 Tesla. Pediatr. Radiol. 2006;37:69–73. doi: 10.1007/s00247-006-0334-8.

85. Hargreaves BA, Vasanawala SS, Nayak KS, Hu BS, Nishimura DG. Fat-suppressed steady-state free precession imaging using phase detection. Magn. Reson. Med. 2003;50:210–213. doi: 10.1002/mrm.10488.

86. Mazzoli V, Nederveen AJ, Oudeman J, Sprengers A, Nicolay K, Strijkers GJ, Verdonschot N. Water and fat separation in real-time MRI of joint movement with phase-sensitive bSSFP. Magn. Reson. Med. 2017;78:58–68. doi: 10.1002/mrm.26341.

87. Hargreaves BA, Bangerter NK, Shimakawa A, Vasanawala SS, Brittain JH, Nishimura DG. Dual-acquisition phase-sensitive fat–water separation using balanced steady-state free precession. Magn. Reson. Imaging 2006;24:113–122. doi: 10.1016/j.mri.2005.10.013.

88. Ma J. Breath-hold water and fat imaging using a dual-echo two-point dixon technique with an efficient and robust phase-correction algorithm. Magn. Reson. Med. 2004;52:415–419. doi: 10.1002/mrm.20146.

89. Winkelmann S, Schaeffter T, Koehler T, Eggers H, Doessel O. An optimal radial profile order based on the Golden Ratio for time-resolved MRI. IEEE Trans. Med. Imaging 2007;26:68–76. doi: 10.1109/TMI.2006.885337.

90. Zhou Z, Han F, Yan L, Wang DJJ, Hu P. Golden-ratio rotated stack-of-stars acquisition for improved volumetric MRI. Magn. Reson. Med. 2017;78:2290–2298. doi: 10.1002/mrm.26625.

91. Seiberlich N, Breuer F, Blaimer M, Jakob P, Griswold M. Self-calibrating GRAPPA operator gridding for radial and spiral trajectories. Magn. Reson. Med. 2008;59:930–935. doi: 10.1002/mrm.21565.

92. Dietrich O, Raya JG, Reeder SB, Reiser MF, Schoenberg SO. Measurement of signal-to-noise ratios in MR images: Influence of multichannel coils, parallel imaging, and reconstruction filters. J. Magn. Reson. Imaging 2007;26:375–385. doi: 10.1002/jmri.20969.

93. Robson PM, Grant AK, Madhuranthakam AJ, Lattanzi R, Sodickson DK, McKenzie CA. Comprehensive quantification of signal-to-noise ratio and g-factor for image-based and k-space-

based parallel imaging reconstructions. Magn. Reson. Med. 2008;60:895–907. doi: 10.1002/mrm.21728.

94. Slawig A, Wech T, Speier P, Petritsch B, Ringler R, Bley T, Köstler H. Banding free bSSFP at long TR values. In: Proceedings of the 34th Annual Meeting of ESMRMB. Barcelona; p. 35.

95. Riederer SJ, Tasciyan T, Farzaneh F, Lee JN, Wright RC, Herfkens RJ. MR fluoroscopy: Technical feasibility. Magn. Reson. Med. 1988;8:1–15. doi: 10.1002/mrm.1910080102.

96. Foxall D l. Frequency-modulated steady-state free precession imaging. Magn. Reson. Med. 2002;48:502–508. doi: 10.1002/mrm.10225.

97. Benkert T, Ehses P, Blaimer M, Jakob PM, Breuer FA. Fast isotropic banding-free bSSFP imaging using 3D dynamically phase-cycled radial bSSFP (3D DYPR-SSFP). Z. Für Med. Phys. 2016;26:63–74. doi: 10.1016/j.zemedi.2015.05.001.

98. Slawig A, Wech T, Ratz V, Tran-Gia J, Neubauer H, Bley T, Köstler H. Multifrequency reconstruction for frequency-modulated bSSFP. Magn. Reson. Med. 2017;78:2226–2235. doi: 10.1002/mrm.26630.

99. Slawig A, Wech T, Ratz V, Tran-Gia J, Neubauer H, Bley TA, Köstler H. Multi-frequency reconstruction for frequency-modulated bSSFP. In: Proceedings of the 24th Annual Meeting of ISMRM. Singapur; 2016. p. 517.

100. Slawig A, Tran-Gia J, Wech T, Neubauer H, Bley TA, Köstler H. Banding free bSSFP CINE imaging using a multi-frequency reconstruction. In: Proceedings of the 24th Annual Meeting of ISMRM. Singapur; 2016. p. 1794.

101. Slawig A, Tran-Gia J, Wech T, Neubauer H, Bley TA, Köstler H. Multi-frequency reconstruction for frequency-modulated bSSFP Imaging. In: Proceedings of the 32th Annual Meeting of ESMRMB. Edinburgh; 2015. p. 31.

102. Mazumdar A, Hargreaves B, Han E, Brau A, Yu H, Brittain J. Automated Fat-Water Identification in Phase Sensitive SSFP. In: Proc. Intl. Soc. Mag. Reson. Med. 13 (2005). Miami; 2005. p. 2307.

103. Yilmaz O, Saritas EU, Çukur T. Enhanced phase-sensitive SSFP reconstruction for fat-water separation in phased-array acquisitions. J. Magn. Reson. Imaging 2016;44:148–157. doi: 10.1002/jmri.25138.

104. Mazzoli V, Nederveen AJ, Oudeman J, Sprengers A, Nicolay K, Strijkers GJ, Verdonschot N. Water and fat separation in real-time MRI of joint movement with phase-sensitive bSSFP. Magn. Reson. Med. 2017;78:58–68. doi: 10.1002/mrm.26341.

105. Slawig A, Ratz V, Wech T, Neubauer H, Bley T, Köstler H. Phase-sensitive water-fat separation using frequency-modulated bSSFP. In: Proceedings of the 33th Annual Meeting of ESMRMB. Vienna; pp. 154–155.

106. Walsh DO, Gmitro AF, Marcellin MW. Adaptive reconstruction of phased array MR imagery. Magn. Reson. Med. 2000;43:682–690. doi: 10.1002/(SICI)1522-2594(200005)43:5<682::AID-MRM10>3.0.CO;2-G.

107. Wansapura JP. Abdominal fat–water separation with SSFP at 3 Tesla. Pediatr. Radiol. 2006;37:69–73. doi: 10.1007/s00247-006-0334-8.

108. Goldfarb JW, Arnold-Anteraper S. Water-Fat Separation Imaging of the Heart with Standard Magnetic Resonance bSSFP CINE Imaging. Magn. Reson. Med. 2014;71:2096–2104. doi: 10.1002/mrm.24879.

109. Hargreaves BA, Bangerter NK, Shimakawa A, Vasanawala SS, Brittain JH, Nishimura DG. Dual-acquisition phase-sensitive fat–water separation using balanced steady-state free precession. Magn. Reson. Imaging 2006;24:113–122. doi: 10.1016/j.mri.2005.10.013.

110. Cher DJ, Conwell JA, Mandel JS. MRI for Detecting Silicone Breast Implant Rupture: Meta-analysis and Implications. Ann. Plast. Surg. 2001;47:367.

111. Kiilgaard JF, Milea D, Løgager V, la Cour M. Cerebral migration of intraocular silicone oil: an MRI study. Acta Ophthalmol. (Copenh.) 2011;89:522–525. doi: 10.1111/j.1755-3768.2009.01793.x.

IV. Publications

Journal article

Slawig A, Wech T, Ratz V, Tran-Gia J, Neubauer H, Bley T, Köstler H.
Multifrequency reconstruction for frequency-modulated bSSFP.
Magn. Reson. Med. 2017; 78:2226–2235.
doi: 10.1002/mrm.26630

Patent

Inventors: **Anne Slawig**, Prof. Herbert Köstler
An algorithm to separate water and fat signal in a frequency-modulated balanced steady-state free precession MR imaging acquisition
Erfindungsmeldungsnummer: 2017E09320 DE / Patentanmeldung Nr. 15/711,511

Conference Abstracts

Slawig A, Tran-Gia J, Wech T, Neubauer H, Bley TA, Köstler H.
Multi-frequency reconstruction for frequency-modulated bSSFP Imaging.
32th Annual Meeting of ESMRMB. Edinburgh; 2015

Slawig A, Wech T, Ratz V, Tran-Gia J, Neubauer H, Bley TA, Köstler H.
Multi-frequency reconstruction for frequency-modulated bSSFP.
10th EUREKA! Symposium of the Graduate School of Life Sciences, Würzburg 2015

Slawig A, Wech T, Ratz V, Tran-Gia J, Neubauer H, Bley TA, Köstler H.
Multi-frequency reconstruction for frequency-modulated bSSFP.
24th Annual Meeting of ISMRM. Singapur; 2016

Slawig A, Tran-Gia J, Wech T, Neubauer H, Bley TA, Köstler H.
Banding free bSSFP CINE imaging using a multi-frequency reconstruction.
24th Annual Meeting of ISMRM. Singapur; 2016

Slawig A, Ratz V, Wech T, Neubauer H, Bley T, Köstler H.
Phase-sensitive water-fat separation using frequency-modulated bSSFP.
33th Annual Meeting of ESMRMB. Vienna; 2016

Slawig A, Wech T, Ratz V, Neubauer H, Bley T, Köstler H
Frequenzmodulierte bSSFP zur phasensensitiven Trennung von Fett und Wasser
Jahrestagung DGMP, Würzburg; 2016

Slawig A, Wech T, Speier P, Petritsch B, Ringler R, Bley T, Köstler H.
Banding free bSSFP at long TR values.
34th Annual Meeting of ESMRMB. Barcelona 2017

Slawig A, Wech T, Speier P, Petritsch B, Ringler R, Bley T, Köstler H.
Banding removal in long TR bSSFP measurements
12th EUREKA! Symposium of the Graduate School of Life Sciences, Würzburg 2017

Stich M, Blümlein L, F. Schmidl F, **Slawig A**, Lösch R, Hipp M, Ese Z, Kressmann M, Kreutner J, Schaefers G, Köstler H, Ringler R
A tissue-equivalent test environment for malfunctions of active V 6 medical implants and electronic devices due to radiation
Jahrestagung DGMP, Dresden; 2017

Stich M., Wech T, **Slawig A**, Ringler R, Dewdney A, Greiser A, Ruyters G, Thorsten Bley T, Köstler H
Implementation of a Gradient Pre-emphasis Based on the Gradient Impulse Response Function
25th Annual Meeting of ISMRM. Honolulu; 2017

VI. Eidesstattliche Erklärung / Affidavit

Hiermit erkläre ich an Eides statt, die Dissertation „Rekonstruktionsmethoden für die frequenz-modulierte balanced steady-state free precession MRT-Sequenz“ eigenständig, d.h. insbesondere selbständig und ohne Hilfe eines kommerziellen Promotionsberaters, angefertigt und keine anderen als die von mir angegebenen Quellen und Hilfsmittel verwendet zu haben.

Ich erkläre außerdem, dass die Dissertation weder in gleicher noch in ähnlicher Form bereits in einem anderen Prüfungsverfahren vorgelegen hat.

Ort, Datum Unterschrift

I hereby confirm that my thesis entitled “Reconstruction methods for frequency-modulated balanced steady-state free precession MRI-sequence “ is the result of my own work. I did not receive any help or support from commercial consultants. All sources and / or materials applied are listed and specified in the thesis.

Furthermore, I confirm that this thesis has not yet been submitted as part of another examination process neither in identical nor in similar form.

Place, Date Signature

VII. Acknowledgements

Mein Dank gilt allen Personen die es mir direkt und indirekt ermöglicht haben, diese Arbeit anzufertigen.

Für die erstklassige Betreuung, ständige Unterstützung und viele unbezahlbare Tipps und Ratschläge danke ich meinem Betreuer Herrn Prof. Dr. Herbert Köstler. Ihr unermüdlicher Einsatz und die gute Stimmung in Ihrer Arbeitsgruppen haben mir bei der Bearbeitung des Themas sehr geholfen und auch den Spaß an der Arbeit nicht zu kurz kommen lassen.

In diesem Zusammenhang geht mein Dank auch an die weiteren Mitglieder meines Promotionskomitees, für ihr Feedback und ihre Vorschläge. Herr Prof. Dr. Michael Laßmann, als Zweitbetreuer, und Herrn Prof. Dr. Thorsten Bley, der nicht nur das Komitee vervollständigte, sondern mir auch die Möglichkeit bot, die Ressourcen am Institut für Diagnostische und Interventionelle Radiologie zu nutzen, um meine Forschung durchzuführen.

Die Graduate School of Life Sciences stellte den Rahmen für ein strukturiertes Promotionsverfahren, bot viele lehrreiche Kurse und unterstützte meine Teilnahme an Konferenzen. Hierfür bin ich der GSLS und allen ihren Mitarbeitern sehr dankbar.

Meinen Kollegen Tobias Wech, Andreas Weng, Johannes Tran-Gia, Fabian Hilbert, Valentin Ratz, Lenon Mendez-Pereira, Manuel Stich, Tina Urbanek, Petra Thomas, Katharina Rath und Susanne Gaul danke ich für zahlreiche fachliche (und nichtfachliche aber nützliche) Diskussionen, das Korrekturlesen meiner Schriftstücke und diverse Code-Schnipsel. Außerdem dafür, dass sie immer bereit waren Dienstreisen zu einem Abenteuer zu machen und dafür, dass ich sie nicht nur als Kollegen, sondern auch als Freunde betrachten darf.

Ich danke ebenfalls allen Freunden und Mitstreitern die für eine tolle Zeit außerhalb des Büros gesorgt haben und somit den nötigen Ausgleich schafften.

Meiner Schwester Diana danke ich außerdem für ein immer offenes Ohr, eine große Bibliothek, viele Stunden Korrekturlesen und ihre Treue als Besucher.

Ein großes „Danke für Alles!“ geht an meinen Freund Hannes.

Zuletzt möchte ich an dieser Stelle meinen Eltern Heiko und Sylke danken, für die unendliche Unterstützung von klein auf und dass sie immer an mich geglaubt haben. Papa, mit Abgabe der Arbeit bin ich kein Student mehr und niemand musste unter der Brücke schlafen.

VIII. Appendix

	Subject	Dim	Traj	Scanner	FOV	Resolution	Slices/ Part.	lines	TR	TE	Flip-angle	Band-width	Scan time	Purpose	Figure
1)	Phantom	2D	RA, GA, CART	Prisma (3T)	300x300	1.2x1.2x5	1	402 402 256	4.2	2.1	69		1s	Simulated signals, artifacts	20
2)	Phantom/metal	2D	GA	Prisma (3T)	300x300	0.7x0.7x10	1	4000	5	2.5	60		20s	dephasing	21
3)	Human heart	2D	GA	Prisma (3T)	300x300	2.3x2.3x5	1	6000	3.48	1.72	36		23s	Real time cine	22
4)	Phantom	2D	GA	Skyra (3T)	200x200	0.4x0.4x8	1	1000	40 20 8		70		40s 20s 8s	Long TR	23
5)	Knee	3D	SToST	Aera (1.5T)	140x140x640	1.1x1.1x1.1	128	208 pp	5.2	2.6	50	305	4m6s	Muffm	28,
6)	Phantom	2D	GA	Skyra (3T)	300x300	0.6x0.6	1	800	5.4	2.7	70	574	7s	SNR Muffm	29, 32
7)	Phantom	3D	SToST	Skyra (3T)	300x300x32	2.3x2.3x2	16	214 pp	2.8	1.4	41	550	14s	SNR Muffm	29
8)	Lower leg	3D	SToST	Aera (1.5T)	140x140x640	1.1x1.1x1.1	128	208 pp	5.2	2.6	50	305	4m6s	Muffm	30
9)	Inner ear	3D	SToST	Skyra (3T)	242x242x38.4	0.6x0.6x0.6	64	680 pp	5.2	2.6	50	620	5m9s	Muffm	30
10)	Human heart	2D	GA CINE	Prisma (3T)	340x340	2.6x2.6x5	1	6300	2.8	1.4	39		19s	Muffm	31, 34, 41
11)	Lower leg	3D	SToST	Aera (1.5T)	320x320x128	1.0x1.0x1.0	128	526 pp	4.6	2.3	30	434	5m55s	WatFat	35, 36, 39
12)	Upper leg	3D	SToST	Skyra (3T)	380x380x202	1.8x1.8x1.8	112	360 pp	2.47	1.23	42	1502	1m43s	WatFat	37
13)	Lower leg	3D	SToST	Skyra (3T)	350x350x105	1.1x1.1x1.1	96	592 pp	7.2	3.6	30	220	8m36s	WatFat	38
14)	Lower leg	2D	GA	Aera (1.5T)	340x340	0.7x0.7	1	1000	4.6 13.8 23	2.3 6.9 11.5	70	674	7s 21s 35s	WatFat longTR	24, 33, 40
15)	Water-Fat Phantom	2D	GA	Aera (1.5T)	340x340	0.7x0.7	1	1000	4.6 13.8 23	2.3 6.9 11.5	70	674	7s 21s 35s	WatFat longTR	24, 40

Table 1: Measurement parameters, Dim-Dimension, Traj-Trajectory, RA- radial, GA- radial with golden angel spacing, CART- Cartesian, SToST- stack-of-stars, Part- Partitions, muffm-multifrequency reconstruction for frequency-modulated bSSFP, WatFat- Water Fat separation algorithm